STO TECHNICAL REPORT

TR-SET-219

Simulation of Active Imaging Systems

(Simulation de systèmes d'imagerie active)

Final Report of SET-219.

Simulation of Active Imaging Systems

(Simulation de systèmes d'imagerie active)

Final Report of SET-219.

The NATO Science and Technology Organization

Science & Technology (S&T) in the NATO context is defined as the selective and rigorous generation and application of state-of-the-art, validated knowledge for defence and security purposes. S&T activities embrace scientific research, technology development, transition, application and field-testing, experimentation and a range of related scientific activities that include systems engineering, operational research and analysis, synthesis, integration and validation of knowledge derived through the scientific method.

In NATO, S&T is addressed using different business models, namely a collaborative business model where NATO provides a forum where NATO Nations and partner Nations elect to use their national resources to define, conduct and promote cooperative research and information exchange, and secondly an in-house delivery business model where S&T activities are conducted in a NATO dedicated executive body, having its own personnel, capabilities and infrastructure.

The mission of the NATO Science & Technology Organization (STO) is to help position the Nations' and NATO's S&T investments as a strategic enabler of the knowledge and technology advantage for the defence and security posture of NATO Nations and partner Nations, by conducting and promoting S&T activities that augment and leverage the capabilities and programmes of the Alliance, of the NATO Nations and the partner Nations, in support of NATO's objectives, and contributing to NATO's ability to enable and influence security and defence related capability development and threat mitigation in NATO Nations and partner Nations, in accordance with NATO policies.

The total spectrum of this collaborative effort is addressed by six Technical Panels who manage a wide range of scientific research activities, a Group specialising in modelling and simulation, plus a Committee dedicated to supporting the information management needs of the organization.

- AVT   Applied Vehicle Technology Panel
- HFM   Human Factors and Medicine Panel
- IST   Information Systems Technology Panel
- NMSG   NATO Modelling and Simulation Group
- SAS   System Analysis and Studies Panel
- SCI   Systems Concepts and Integration Panel
- SET   Sensors and Electronics Technology Panel

These Panels and Group are the power-house of the collaborative model and are made up of national representatives as well as recognised world-class scientists, engineers and information specialists. In addition to providing critical technical oversight, they also provide a communication link to military users and other NATO bodies.

The scientific and technological work is carried out by Technical Teams, created under one or more of these eight bodies, for specific research activities which have a defined duration. These research activities can take a variety of forms, including Task Groups, Workshops, Symposia, Specialists' Meetings, Lecture Series and Technical Courses.

The content of this publication has been reproduced directly from material supplied by STO or the authors.

Table of Contents

List of Figures

List of Tables

SET-219 Membership List

CHAIR

Dr. Richard ESPINOLA
Naval Research Laboratory (NRL) – DC
UNITED STATES
Email: richard.espinola@nrl.navy.mil

MEMBERS

Dr. Weilin HOU
Naval Research Laboratory (NRL) – SSC
UNITED STATES
Email: weilin.hou@nrlssc.navy.mil

Dr. Kimberly Erin MANSER
US Army RDECOM
UNITED STATES
Email: kimberly.e.manser.civ@mail.mil

Mr. Peter LUTZMANN
Fraunhofer-IOSB Institute
GERMANY
Email: peter.lutzmann@iosb.fraunhofer.de

Mr. Olivier MEYER
DGA Maîtrise de l'Information / CGN2 /
 SDO Signature et Détection Optronique
FRANCE
Email: olivier.meyer@intradef.gouv.fr

Dr. Guy POTVIN
DRDC Valcartier
CANADA
Email: guy.potvin@drdc-rddc.gc.ca

Mr. Endre REPASI
Fraunhofer IOSB
GERMANY
Email: endre.repasi@iosb.fraunhofer.de

Dr. Kurt Ove Johannes STEINVALL
Swedish Defence Research Agency (FOI)
SWEDEN
Email: ove.steinvall@foi.se

Dr. Michael TULLDAHL
Swedish Defence Research Agency (FOI)
SWEDEN
Email: michael.tulldahl@foi.se

ADDITIONAL CONTRIBUTOR

Dr. Jose PEREZ
Fraunhofer Institute of Optronics,
System Technologies and Image Exploitation IOSB
GERMANY
Email: jose.perez@iosb.fraunhofer.de

PANEL/GROUP MENTOR

Dr. Donald A. REAGO
Night Vision Lab
UNITED STATES
Email: donald.a.reago.civ@mail.mil

Simulation of Active Imaging Systems
(STO-TR-SET-219)

Executive Summary

Active imaging systems are continually being developed and investigated for their ability to significantly improve tactical target acquisition, particularly under adverse environmental (land/sea/air) conditions. Accurate simulation tools can aid in the design and development, as well as the performance assessment, of active imaging systems. Currently available imaging models are limited in their ability to accurately represent active imaging systems in full spectral simulations, particularly in the atmosphere's effect on laser beam propagation and corresponding radiometric phenomenology on advanced sensor systems. NATO SET-219 addressed this limitation by advancing the modeling and simulation tools and techniques for state-of-the-art 1D/2D/3D active imaging systems. In this context, simulation is understood to mean the generation of synthetic image sequences that include laser illumination/environmental/sensor system parameters.

SET-219 set out with the following set of objectives and goals that would advance the working group's understanding, leveraging much of what was learned through previous groups SET-072 and SET-156, and provide situational awareness of the state-of-the-art in active imaging simulation tools and techniques:

- Perform a robust review of existing active imaging system simulations currently being used throughout NATO SET community.

- Evaluate high resolution physics-based simulations of active imaging system phenomenology, e.g., phase screen propagation and full spectral scene generation; evaluation concentrated on the block components of the simulations, viz.:

    - Laser interaction with atmospheric and underwater environments;

    - Target and background characterization;

    - Sensor system components and subcomponents, i.e., laser illuminator and detector; and

    - Performance limits and capability gaps.

- Demonstrate and exercise simulations on 1D/2D/3D active imaging system applications.

- Recommend improvements to active imaging system simulations.

The current state-of-the-art active sensor modeling tools from France, Canada and Germany are mostly focused on 2D sensing methodologies, namely active laser range gating in the VNIR-SWIR spectral range, and have shown good verification and validation through successful field test campaigns. Sweden and the US Army have introduced simulation tools for 3D Ladar imaging. Sweden has proposed to use the same tool for 1D profiling as well. The US Navy has continued to develop an underwater scene simulation. Each of these tools were utilized to assess utility and address capability gaps, such as measurement of optical properties of materials (targets and backgrounds) for BRDF, operation of tools beyond the weak turbulence regime and allowing for spatially varying C_n^2 for slant path geometries. Computational efficiency was also identified as a gap that can be obviated through the use of CPU/GPU resources as well as optimized code development.

Finally, the recommendation of the group is to perform an image quality assessment and validation by developing appropriate IQ metrics and using them to compare simulated data with existing field data, as well as data obtained from new national and/or joint NATO SET field trials. Further work is suggested by all nations to implement new modules that address and fill each of the identified capability gaps.

Simulation de systèmes d'imagerie active
(STO-TR-SET-219)

Synthèse

Les systèmes d'imagerie active font l'objet d'un développement et d'études continus, en raison de leur capacité à améliorer considérablement l'acquisition des objectifs, notamment en conditions environnementales hostiles (terre / mer / air). Des outils de simulation précis peuvent faciliter la conception et le développement – ainsi que l'évaluation du fonctionnement – de systèmes d'imagerie active. Les modèles d'imagerie actuellement disponibles ont une capacité limitée à représenter avec précision les systèmes d'imagerie active dans les simulations spectrales complètes, en particulier pour l'effet de l'atmosphère sur la propagation du faisceau laser et pour les effets des phénomènes radiométriques correspondants sur les systèmes de capteurs perfectionnés. Le SET-219 de l'OTAN a traité cette restriction en faisant progresser les outils et techniques de modélisation et simulation relatifs aux systèmes d'imagerie active de pointe en 1D / 2D / 3D. Dans ce contexte, la simulation désigne la production de séquences d'images de synthèse qui incluent les paramètres d'illumination laser / environnementaux / du système de capteurs.

Le SET-219 a été établi pour faire progresser la compréhension sur ce sujet, en utilisant nombre des enseignements des précédents groupes SET-072 et SET-156, et fournir une connaissance de la situation des outils et techniques de pointe en matière de simulation d'imagerie active. Ses objectifs étaient les suivants :

- Réaliser une revue exhaustive des simulations existantes des systèmes d'imagerie active, actuellement utilisées dans toute la communauté SET de l'OTAN.

- Evaluer les simulations basées sur la physique à haute résolution de la phénoménologie des systèmes d'imagerie active, par exemple, la propagation d'écran de phase, la production d'une scène spectrale complète et l'évaluation concentrée sur les composants modulaires des simulations, à savoir :
  - Interaction du laser avec les environnements atmosphériques et sous-marins ;
  - Caractérisation des objectifs et de l'arrière-plan ;
  - Composants et sous-composants des systèmes de capteurs, autrement dit, illuminateur et détecteur laser ; et
  - Limites de performance et lacunes en matière de capacités.

- Démontrer et réaliser des simulations portant sur des applications de système d'imagerie active en 1D / 2D / 3D.

- Recommander des améliorations à apporter aux simulations des systèmes d'imagerie active.

En France, au Canada et en Allemagne, les outils de modélisation à la pointe de la technologie des capteurs actifs se focalisent principalement sur les méthodologies de détection en 2D, à savoir le crénelage spatial laser actif dans le domaine spectral VNIR-SWIR, et ont obtenu de bons résultats de vérification et de validation lors des campagnes d'essai sur le terrain. La Suède et l'armée de terre des Etats-Unis ont introduit des outils de simulation pour l'imagerie Ladar en 3D. La Suède a proposé d'utiliser le même outil pour le profilage en 1D. La marine des Etats-Unis continue de développer une simulation des scènes sous-marines. Chacun de ces outils a été utilisé pour évaluer l'utilité et combler les lacunes de capacité, telles que la mesure des propriétés optiques des matériaux (objectifs et arrière-plan) pour la BRDF, le fonctionnement des outils au-delà du régime de faible turbulence et variation spatiale de C_n^2 pour les géométries de trajet oblique.

L'efficacité du calcul a également été identifiée comme une lacune qui peut être comblée par l'utilisation de ressources d'unité centrale / processeur graphique, ainsi que par l'élaboration d'un code optimisé.

Enfin, le groupe recommande de réaliser une évaluation et une validation de la qualité d'image en développant des indicateurs appropriés et en les utilisant pour comparer les données simulées avec les données de terrain existantes, ainsi qu'avec des données obtenues pendant de nouveaux essais de terrain au niveau de chaque pays et/ou du SET de l'OTAN. Il est suggéré que tous les pays entreprennent d'autres travaux pour mettre en œuvre de nouveaux modules comblant chacune des lacunes de capacité identifiées.

Chapter 1 – INTRODUCTION

Active imaging systems offer the promise of significantly improved tactical performance compared to passive military systems operating in adverse ground, air, and underwater/maritime environments [1], [2], [3]. These improvements would include, but are not limited to:

• Extending the ability to operate when passive sensors will not perform satisfactorily;

• Improving target detection, recognition, and identification performance; and

• Improving capability to determine the exact nature of the activity being pursued by individuals or vehicles at increased ranges.

The modern military battlefield could therefore greatly benefit from the use of active imaging systems.

Accurate modelling and simulation tools can aid in the design and development, as well as the performance assessment, of active imaging systems [4]. Currently available imaging models are limited in their ability to accurately represent active imaging systems in full spectral simulations, particularly in the atmosphere's effect on laser beam propagation and corresponding radiometric phenomenology on advanced sensor systems [5], [6]. NATO SET-219 working group proposes to mitigate these limitations by advancing the modelling and simulation tools and techniques for state-of-the-art 1D/2D/3D active imaging systems. In this context, simulation is understood to mean the generation of synthetic image sequences that include laser illumination/environmental/sensor system parameters.

SET-219 set out with the following set of objectives and goals that would advance the working group's understanding, leveraging much of what was learned through previous groups (SET-072 and SET-156) [7], [8], and provide situational awareness of the state-of-the-art in active imaging simulation tools and techniques:

• Perform a robust review of existing active imaging system simulations currently being used throughout NATO SET community.

• Evaluate high resolution physics-based simulations of active imaging system phenomenology, e.g., phase screen propagation and full spectral scene generation; evaluation concentrated on the block components of the simulations, viz.:

    • Laser interaction with atmospheric and underwater environments;

    • Target and background characterization;

    • Sensor system components and subcomponents, i.e., laser illuminator and detector; and

    • Performance limits and capability gaps.

• Demonstrate and exercise simulations on 1D/2D/3D active imaging system applications.

• Recommend improvements to active imaging system simulations.

The group was able to address and make progress in each of the main objectives listed above. The resulting enhancements to active imaging simulations will be a critical enabler for future sensor technology development and assessment.

This report describes the program of work accomplished and presents the results to date. This remainder of this report is organized as follows. Chapter 2 presents the active imaging technologies and applications studied. Chapter 3 described each NATO member's existing simulation tools. Chapter 4 provides results on selected simulation case studies. Chapter 5 provides the benefits of using numerical simulations for military

relevant applications. Finally, Chapter 6 concludes with the group's current status, listing of simulation capability gaps, and recommendations for addressing the gaps in potential future NATO SET collaborative research/working groups. Chapter 7 lists the technical references and Annex A is a technical description of the BRDF for turbulent active imaging.

Chapter 2 – ACTIVE IMAGING TECHNOLOGIES AND APPLICATIONS

2.1 ACTIVE IMAGING TECHNOLOGIES

Active imaging systems utilizing laser illuminators in conjunction with imaging sensor arrays offer the promise of significantly improved tactical performance compared to passive military systems operating on ground, in air, and underwater. These improvements would include, but not be limited to:

   i)   Extending the ability to operate when passive sensors will not perform satisfactorily;

   ii) Improving target recognition and identification performance; and

   iii) Improving capability to determine the exact nature of the activity being pursued by individuals or vehicles at increased ranges.

This chapter introduces the different active imaging technologies investigated by the NATO SET-219 working group in its Program of Work (PoW).

2.1.1 1D Profiling System

A modified Laser Range Finder (LRF) or dedicated range-resolving active laser sensor can be used for classification and recognition of targets using the active system's 1D range information. An illustration of the concept is shown in Figure 2-1. The transmitted and reflected laser pulse contains information of not only the range to the target, but also its characteristic range (or temporal) profile. If the laser system has a sufficiently rapid system response (short laser pulse and high detector bandwidth), the reflected pulse from the target can reveal information such as target size and relative position of characteristic parts of the target (e.g. nose cone, wings, and tail fin of an aircraft. The principle of 1D-profiling for target classification and recognition can be applied to air, sea, and ground targets [9], [10]. The method can also provide complementary information to classification based on 2D image data.

Figure 2-1: Long Range Target Characterization by Means of 1D Laser Imaging.

2.1.2 2D Imaging System

Gated imaging is a class of Time-Of-Flight (TOF) imaging technologies where a camera with tightly controlled opening and closing times of the shutter is used in conjunction with a high power pulsed light source. Image contrast is enhanced by gated imaging by limiting the exposure time of the camera to the return time of an emitted light pulse from an object at a defined distance, d. If the light source and camera are collocated, the exposure time should occur at a time after light pulse emission given by $\Delta t = 2\,d/c$, where c is the speed of light.

The principle of gated imaging is outlined in Figure 2-2 and can be used to enhance image contrast in scenes where the object of interest is obscured by clutter or strong light sources that are blurring or saturating the imager. The camera shutter may be controlled by CMOS switches in the imaging electronics.
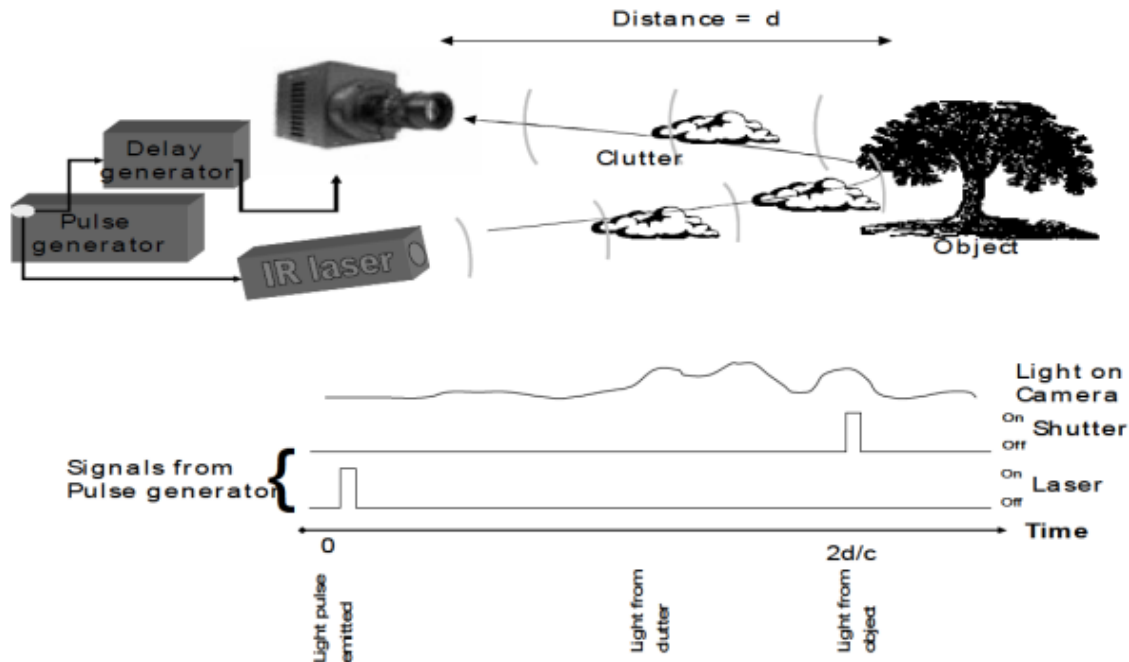
Figure 2-2: Example of Gated Imaging with Pulsed Laser: A tree is partially obscured by mist or other clutter that reflects light and reduces the contrast in the image of the tree. The electronic shutter of the camera is kept closed (i.e. the camera is not integrating light) during the time that the light from the clutter is incident. The shutter is opened only at the time of incidence of the light from the tree.

The gated imaging technologies may be divided into two distinct classes: single-shot or flash imaging sensor, and multishot or integrated imaging sensor. Single shot imagers capture the returned light from one single light pulse, while multishot imagers integrate light from several returned light pulses, within one frame time interval to form an image.

Moreover, controlling the time delay between the laser pulse and the shutter time of the sensor opens new capabilities, such as background suppression and increased target visibility. This "silhouette" capability improves target-to-background contrast and can help the observer in its target identification task.

2.1.3   3D Imaging System

Active 3D imaging can be obtained either from a single pixel scanning system or from a multi pixel system combined with scanning. The most common technique relies on the use of TOF measurements of laser pulses to obtain range information. Each sensor pixel provides range information as well as lateral position obtained and recalculated from the sensor direction. High-resolution systems with many pixels (voxels) on the target are beneficial for target classification and recognition as they can provide 3D information (e.g. size and shape) of a target. Similarly to 1D and 2D active imaging, another advantage with active 3D imaging arises from its ability to image shadowed or partially occluded objects. Imaging of targets in (ambient light) shadow or complete darkness does not limit the active sensor because it has its own illuminating (laser) source. Active imaging also opens possibilities for FOliage PENetration (FOPEN) imaging capabilities, where the 3D range information can effectively enable the penetration of dense foliage backgrounds to reveal hidden targets.

2.2   ACTIVE IMAGING APPLICATIONS

2.2.1   Target Detection/Recognition/Identification

All members of SET-219 are heavily involved in active research investigating 2D active imaging systems for long range target identification, especially in nighttime operation when visible EO systems are not efficient (see Figure 2-3). The task of target identification is better for an active sensor compared to a thermal sensor because of:

•   The shorter wavelength which provides higher optical resolution; and

•   The spectral bands used (0.8 and 1.5 μm): the active image allows the ability to see reflective contribution of the materials, providing images which look more similar to a black and white visible image. The capability to see more visually recognizable patterns allows easier target identification.
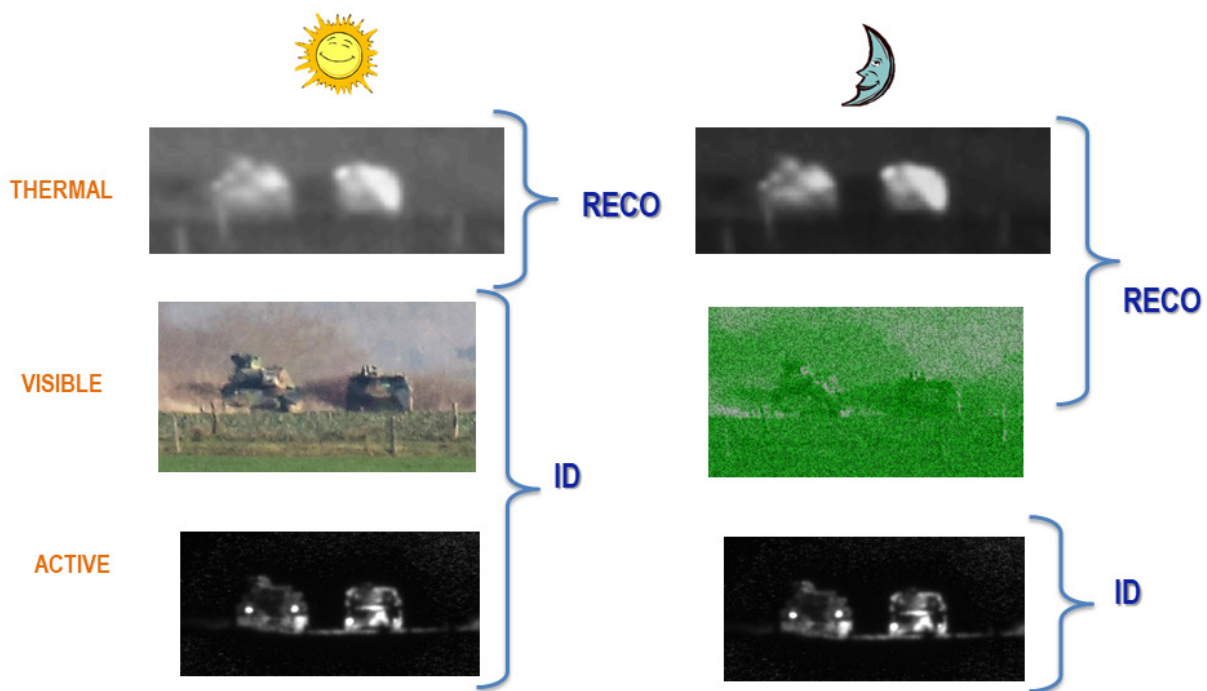
Figure 2-3: Benefit of Active Imaging Sensor for Target ID, Especially in Night Operation.

Moreover, the "silhouette" mode, offered by the range gating capability, can help the operator to better identify the target. This particular capability will be described in the next section.

2.2.2   Underwater Imaging

Underwater imaging is useful for naval applications such as remote UAV for mine detection, obstacle avoidance, and remote sensing. System components are designed very similar to land-based active imaging systems. The main difference is in the imaging phenomenology, particularly in the effect of laser propagation and scatter in a water medium. As in the atmosphere, active gated underwater imaging can mitigate the strong scattering problem to improve detection, recognition, and identification range (see Figure 2-4).

While previous efforts have focused on static treatments of scattering issues, dynamic consideration is necessary where turbulence contribution can be addressed.
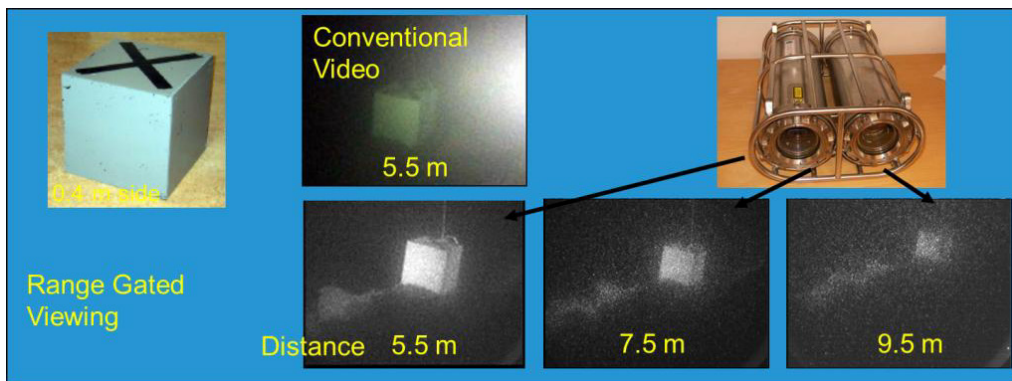
Figure 2-4: Comparison Between Conventional and Range-Gated Image (FOI).

2.2.3   Classification by Target Profiling

A 1D profiling LIDAR has the potential capability to classify and recognize a number of different aircraft, UAVs, ground vehicles and ships. To distinguish between different targets, a classifier can be trained with corresponding (1D LIDAR) data. In Figure 2-5, an example from a 1D profiling experiment and a measured profile is shown. The experiments were made by FOI for studies of profiling for small target recognition [9]. The target range from the sensor is 1.3 km and the target consists of a (physical) mock-up model of a UAV. The length and wingspan of the model are respectively 3.45 m and 3 m. In the 1D profile it is possible to distinguish three separate echo peaks from the UAV nose, wings, and tail fin.
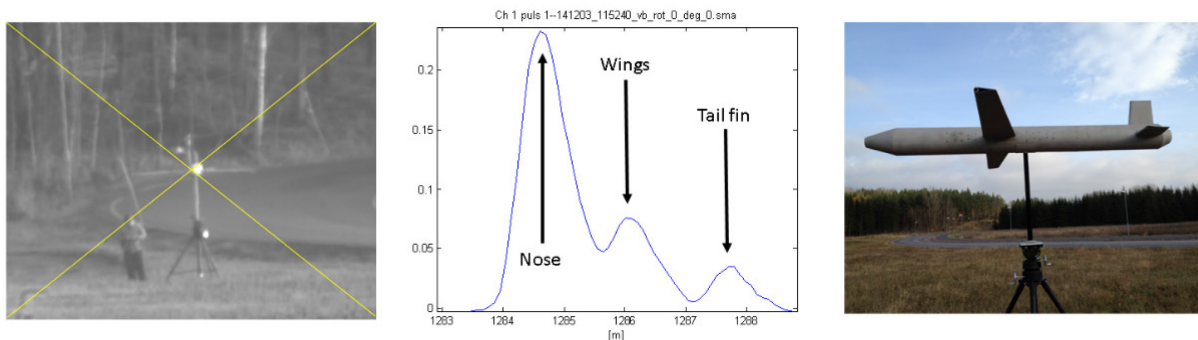
Figure 2-5: Profiling Experiment on a UAV Mock-up Model (Left), Measured LIDAR Range Profile of the UAV (Middle), and a Side View Photo of the Mock-Up Model (Right).

2.2.4   FOliage PENetration (FOPEN)

The FOPEN application requires the use of a full-wave signal. Compared to a regular rangefinder, where usually only one or few detections are done, the full-wave opens the capability of multiple detections because the temporal evolution of the optical signal is acquired. An example of a FOPEN application is shown in Figure 2-6.
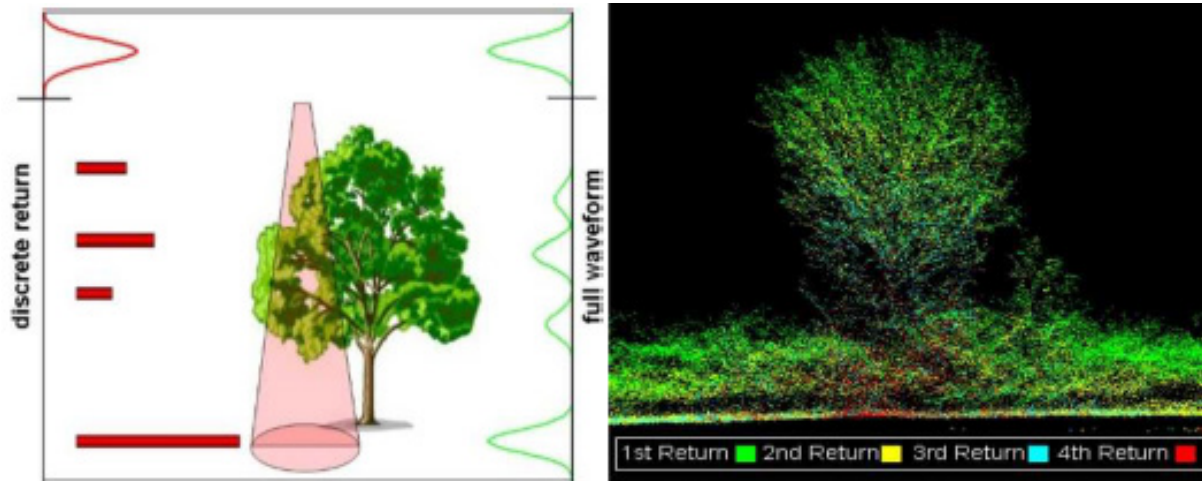
Figure 2-6: FOPEN Application for Undercover Target.

This imaging technique can be used to discover a camouflaged target. Figure 2-7 shows (top left side) that one target is clearly visible, but using FOPEN capability reveals that two other targets are under the canopy (top right side).
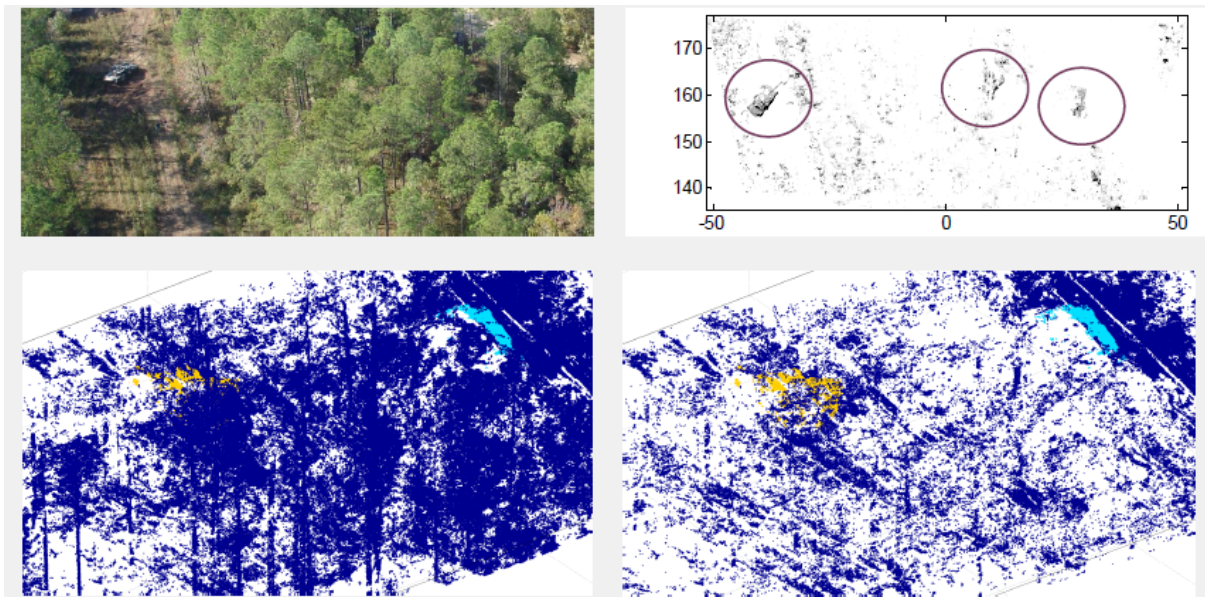
Figure 2-7: FOPEN Application for Undercover Target (FOI).

Chapter 3 – MODELING AND SIMULATION TECHNOLOGIES

3.1 MODELING AND SIMULATION TOOLS

The following section is a catalogue of different modelling and simulation tools that have been developed and utilized by each SET-219 member representative and nation for the purpose of accomplishing the Program of Work.

3.1.1 Canada DRDC Valcartier Research Centre

DRDC has developed a passive imaging simulator model for weak optical turbulence and Lambertian targets designated as the *Optical Turbulence Imaging System Simulator* (OTISS). This model is based on the turbulent imaging data acquired at the *Validation Measurements on Propagation in the Infrared and Radar* (VAMPIRA) trial in 2004. The VAMPIRA trial was part of the NATO SET-056 Task Group and included, among other things, acquiring high-speed image data of a series of lights as seen from across Eckernforde bay of the Baltic Sea in northern Germany [11]. This led to the study of the space-time correlations of the moments of the turbulent Point-Spread Function (PSF) [12], [13], [14] which, in turn, led to the current DRDC model OTISS [15], [16]. OTISS functions by generating a three dimensional bloc of the random refractive index field between the target and the imager. The turbulence is 'frozen' but moves with a constant speed in a direction perpendicular to the imager's line-of-sight. From this OTISS generates a random scalar field that contains all of the necessary information for generating the Gaussian turbulent Point-Spread Function (PSF). This model is the subject of ongoing research and development and the details of its latest version can be found in the NATO SET-156 final report [8].

As a result of the work with the NATO SET-219 group, DRDC has extended OTISS to deal with the active imaging case. The extended model is designated provisionally as OTISS-A. The model must simulate:

a) The propagation of the illuminating pulse from the source to the target surface through turbulence;

b) The reflection/scattering of the rays off the targets surface; and

c) The propagation from the surface to the imager through the same turbulence.

These steps are illustrated in Figure 3-1.
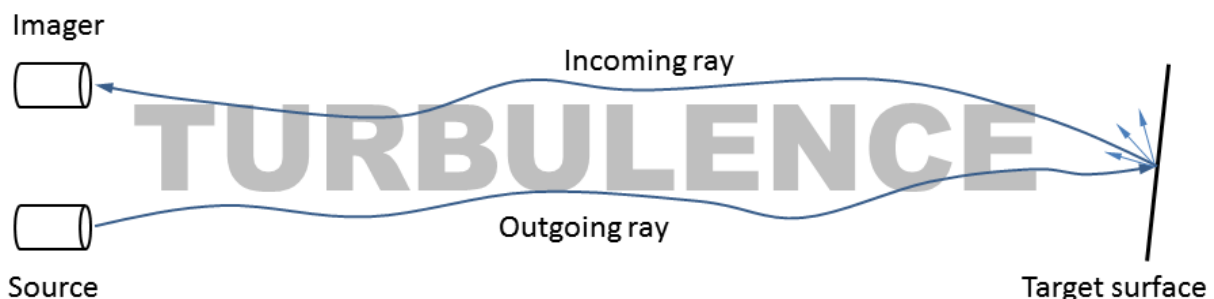
Figure 3-1: Illustration of the Simulation Steps of the DRDC Active Imaging Model. Namely, these three steps are: a) The emission of an outgoing ray from the source to the target through turbulence, b) The reflection/scattering of this ray of the target surface; and c) The propagation of these rays from the target to the imager through turbulence.

As we can see in Figure 3-1, the target surface may not be perfectly perpendicular with respect to the system's line-of-sight. If the target surface is specular to some extent, this can have an effect on the amount of radiance that returns to the imager.

Figure 3-2 shows the reflection/scattering process of a ray off the target surface in detail. In particular, we see on the right hand side of the surface's normal vector the reflected ray in red and the scattered rays in blue. A specular surface therefore only has the reflected ray whereas a Lambertian surface has a spread of scattered rays evenly distributed over the entire hemisphere above the surface. The OTISS-A model characterizes a surface with two coherence lengths. These lengths are inversely proportional to the angular spreads of the scattered ray angles. Also, one length corresponds to an axis tangent to the surface and the other length correspond the axis perpendicular to the first but also tangent to the surface. In this way, OTISS-A can model surfaces with an anisotropic degree of coherence.
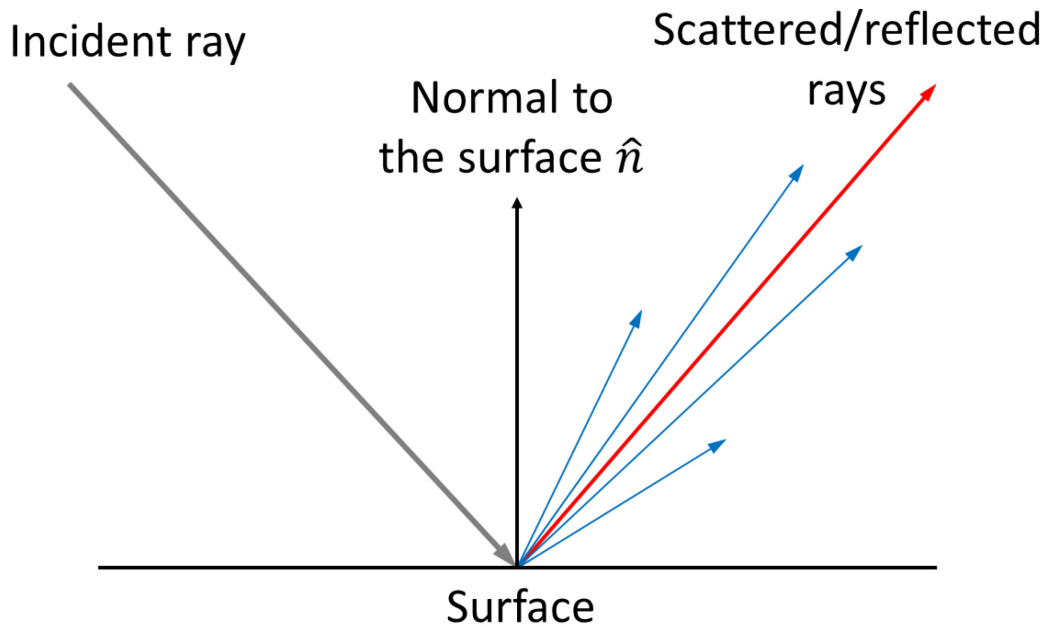
**Figure 3-2: Detailed Illustration of the Reflection/Scattering
Process of a Ray Off the Target Surface.**

Figure 3-3 shows sample outputs from OTISS-A. The original grey panel image (upper left) is given an isotropic coherence length of 8 mm and is seen through 2.3 km of turbulence with a C_n^2 of 5e-14, an outer scale of 10 m and an inner scale of 6 mm (displayed in the upper right). The lower left shows the same panel with a coherence length of 800 μm and the lower right shows the Lambertian (coherence length zero) version of the panel. The upper right panel is very specular, which is why we see a fairly good reflected image of the illuminating source located at the centre of the panel. The lower left panel has a coherence length that is a tenth of the coherence length of the upper right panel. Because there is more scattering over a wider range of angles, the imager receives radiance from a wider area of the panel. The Lambertian surface in the lower right panel has scattering over all angles and so the imager receives radiance from every point of the panel. Readers may consult Annex A for details of this simulation.
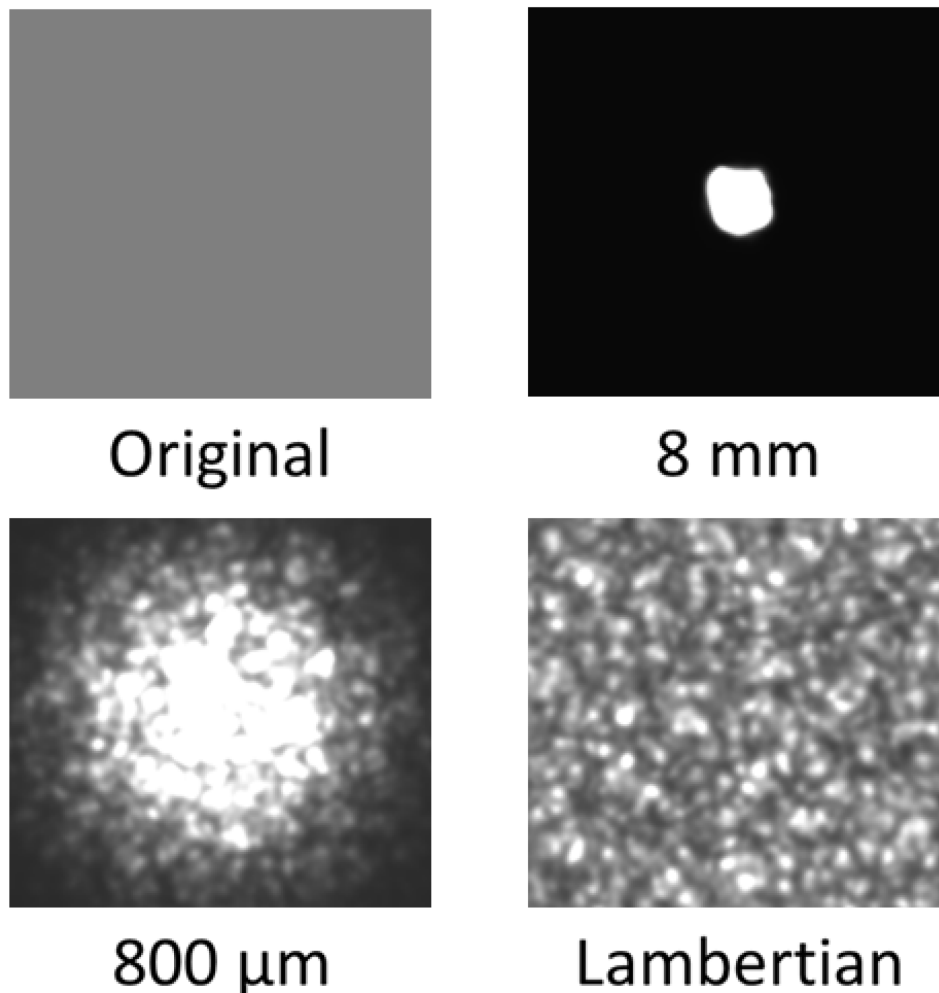
Figure 3-3: Sample Outputs from the OTISS-A Model. The upper left shows the original image of a grey panel. The upper right shows the output for a grey surface with an isotropic coherence length of 8 mm, the lower left with a length of 800 μm and the lower right shows a Lambertian surface. The simulation range is 2.3 km, outer scale 10 m, inner scale 6 mm, C_n^2 5 e-14, wavelength 4.2 μm, IFOV 3.83 μrad, imager aperture diameter 18.36 cm and the source is 1 cm.

3.1.2   France DGA Rennes

The generation of a synthetic image involves several tools, one for each main physical contributor, as detailed in the sub-sections below.

3.1.2.1   The Scene

SE Workbench is a raytracing model used to generate reflective or thermal images of the scene. Generic or specific optical properties of materials can be used, in order to render real diffusion of the scene (Lambertian and/or specular diffusion in the case of the use of BRDF models). Dynamic scenarios can be handled (sensor and/or target moving).

Figure 3-4 illustrates the process of a construction and validation of a synthetic image: using real field image that includes background, target and calibrated reflectance panels, a similar scene is modeled in SE-Workbench.
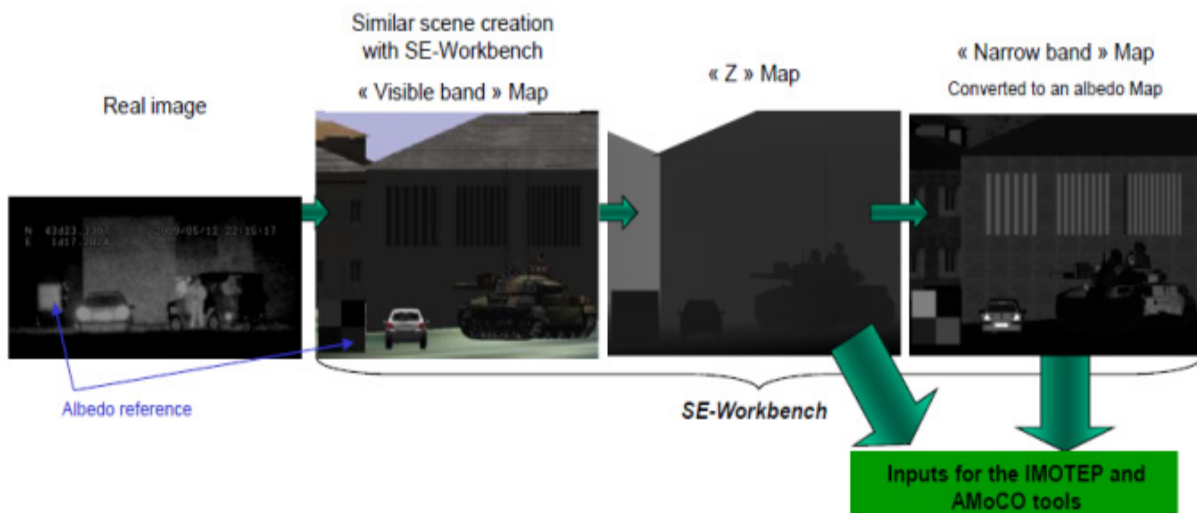
Figure 3-4: Scene Construction and Validation.

3.1.2.2   Atmospheric Effects

Two effects have to be considered:

- Transmission: this effect is estimated either by Modtran or Matisse tool. Both allow accurate estimation of the atmospheric transmission for the small waveband of the laser illuminator.

- Turbulence: Turbulence affects twice the active imaging sensor:
    - Way forth (*laser to target*): because of laser coherence, the turbulence will provide scintillation effect, i.e., non-homogeneous laser illumination in the target plan (see Figure 3-5, middle). This effect is important to be modeled because it is usually the first parameter who will limit the target identification range, especially in ground to ground scenario.
    - Way back (*target to laser*): as other passive imaging sensors, especially with narrow field of view, the image is degraded by the turbulence blur (anisotropic deformation) as shown in Figure 3-5, right.
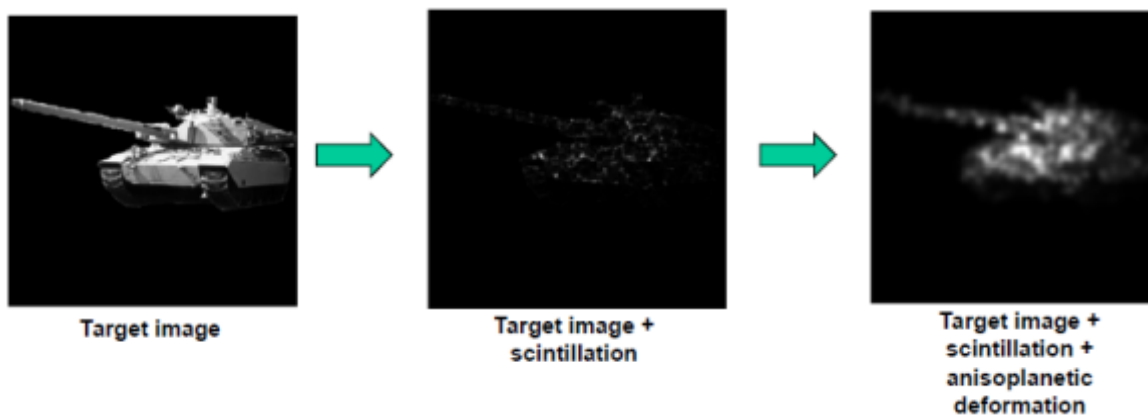
Figure 3-5: Turbulence Effects on 2D Active Imaging Sensor.

In the last years, DGA investigated a lot in the development of a specific tool, IMOTEP (**I**nstrument de **MO**délisation de la **T**urbulence par **E**crans de **P**hase), for turbulence modeling. It allows the computation of

scintillation and anisotropic deformation for active imaging sensor. It is based on the phase screen propagation, running on GPU card for fast calculation and rendering time. IMOTEP drives:

- Gaussian and spherical/Top Hat beam propagation (see Figure 3-6);

- Horizontal or slant path propagation by using vertical profile of C_n^2;

- Time correlation; and

- Compliant with flash and cumulative sensor (short or long time integration).

Image 512² pix
10 screens (1024² pix)
1600 Fourier Comp.
Fov= 5 mrad
Div = 3 mrad
Freq. = 200 Hz

Cn² = 1.10⁻¹⁴ m⁻²ᐟ³
Z = 5 km
Lambda = 1.5 μm
βo² = 1.5
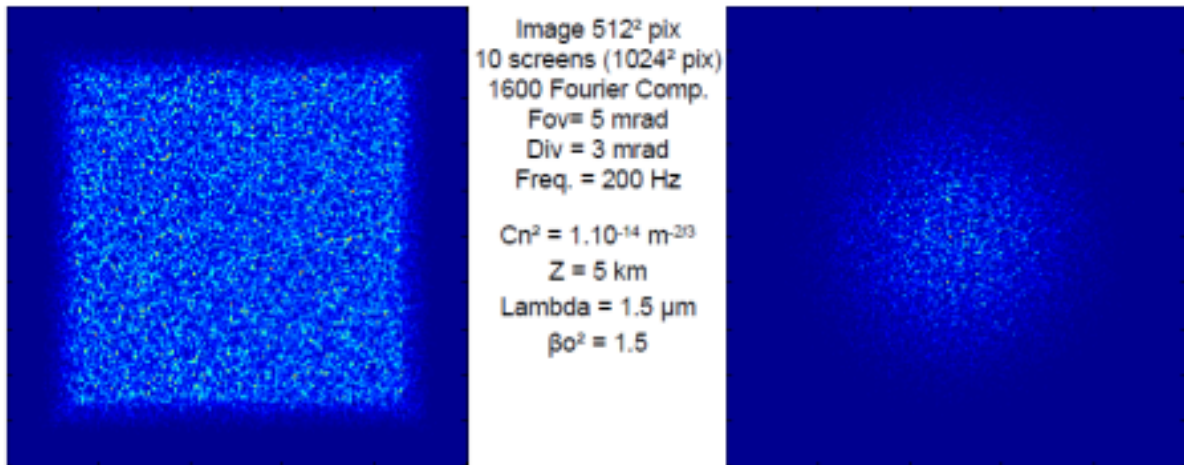
Figure 3-6: Beam Profile – Top Hat (Left) and Gaussian (Right).

The scintillation maps are computed by a phase screen generator algorithm coupled with a phase « spatio-temporal » correlation algorithm from Ref. [17]. Usual computing time is around 0.1 to 5 seconds per scintillation map, depending on the strength of the turbulence.

For the anisotropic deformation of the turbulence, two methods have been investigated:

1) A first method, based on Ref. [18] which uses a Gaussian turbulence PSF, described with 3 parameters (centroid shifts along x and y, width). In Ref. [18], empirical models have been proposed through the analysis of real data (RTG-40) for the estimation of the DSP of the 3 parameters. In IMOTEP method, the PSD are calculated by using the phase screen « spatio-temporal » correlation algorithm and the propagation of many point sources over a finite 1D line. The estimation of the statistics of spatial variations of the turbulence PSF lead to the 1D covariance function of each parameter. Assuming isotropic 3D turbulence because of the small FOV of the sensor, 3D PSD is deduced and used to generated stochastic maps for each of the three parameters (see Figure 3-7).

2) Because the turbulence PSF is described with only a few parameters, the validity range was limited to weak turbulence regime. So a second method based on Ref. [19] has been developed in order to describe a turbulence PSF in a better way, i.e., with higher spatial frequencies. In the new algorithm, a first computational step – the estimation of the principal components – precedes the steps listed mentioned in the first method. During this additional step, a collection of independent realizations of the PSF is generated. Once a set of principal components is obtained, they are used to characterize the spatial (anisoplanatic) variations of the PSF, following the previously steps.
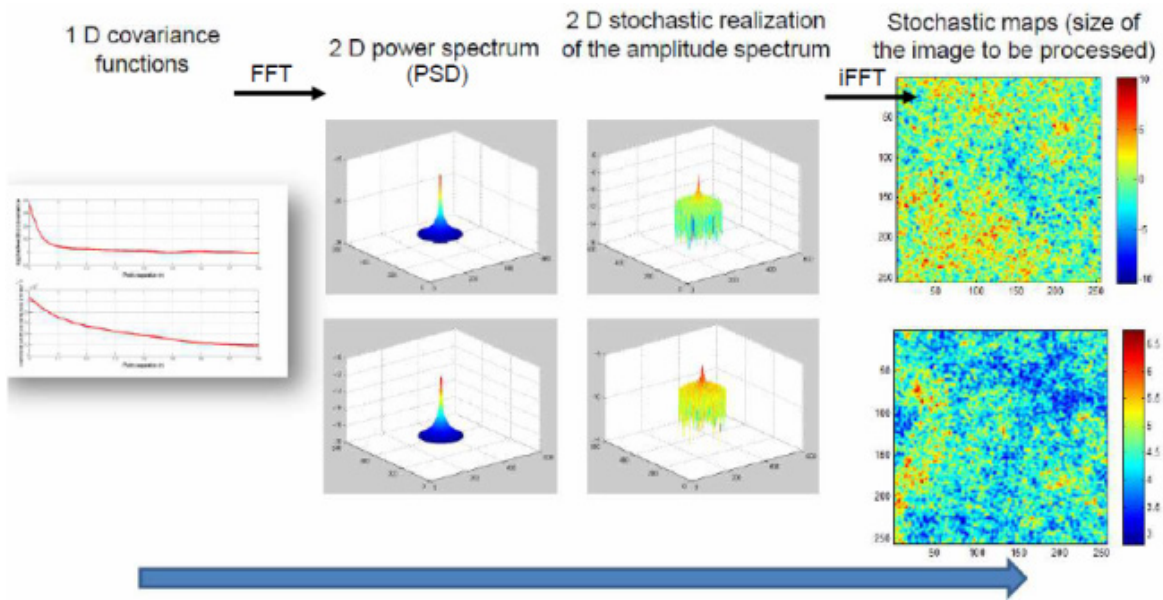
Figure 3-7: Process from 1D Covariance Function to Stochastic Map Generation for Method N°1.

Figure 3-8 clearly illustrates the difference in the turbulence PSF computation between the two methods.
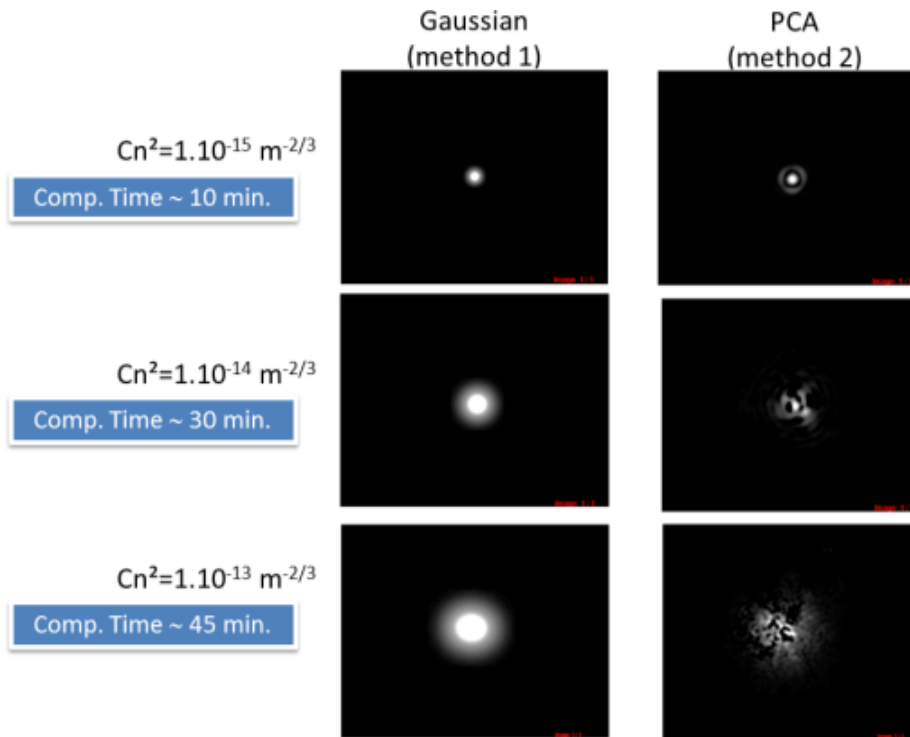
Figure 3-8: Turbulent Point Source at 2 km – Image FOV = 0.5 x 0.4 m.

The effect on image quality and resolution is shown on Figure 3-9; the high frequencies are more visible in the image resulting from the Principles Components Analysis (PCA) PSF rather than the one from the Gaussian PSF.
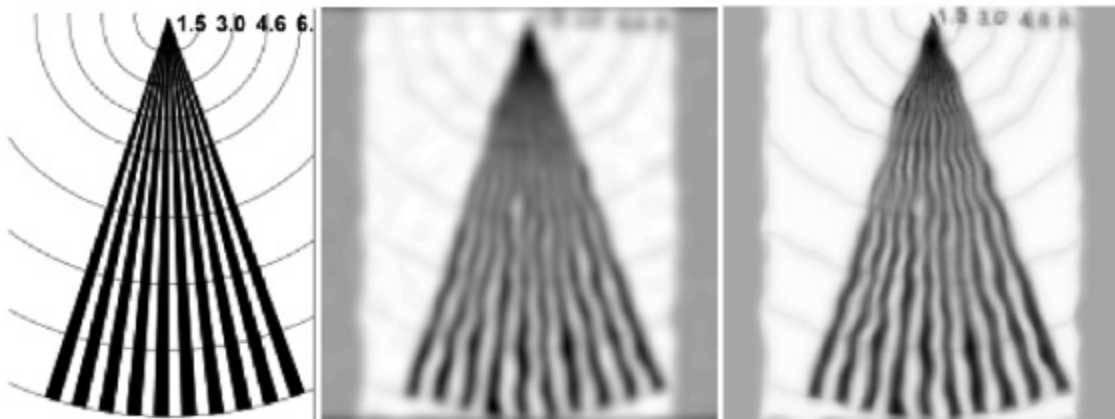
Figure 3-9: Example of Image Processing. Left: input image; Center: Gaussian PSF; Right: PCA-based PSF. (range = 300 m, $C_n^2 = 10^{-13}$ m$^{-2/3}$, 18 cm in diameter aperture, 25 cm x 25 cm target pattern) from Ref. [20].

3.1.2.3   Sensor Effects

The AMoCO tool is a MATLAB environment software, working on modular concept and sequential image processing (image workflow). The model is realized by choosing and applying all the noises and MTF effects or degradations coming from the receiver on an input image (the observed scene). At the output of the model, the scene seen by the sensor receiver is provided. Some additional effects can also be taking into account, like the passive scene contribution in case of daylight use, and optical retro-reflection.

Figure 3-10 illustrates the AMoCO model of the ATV2000i active imaging system.
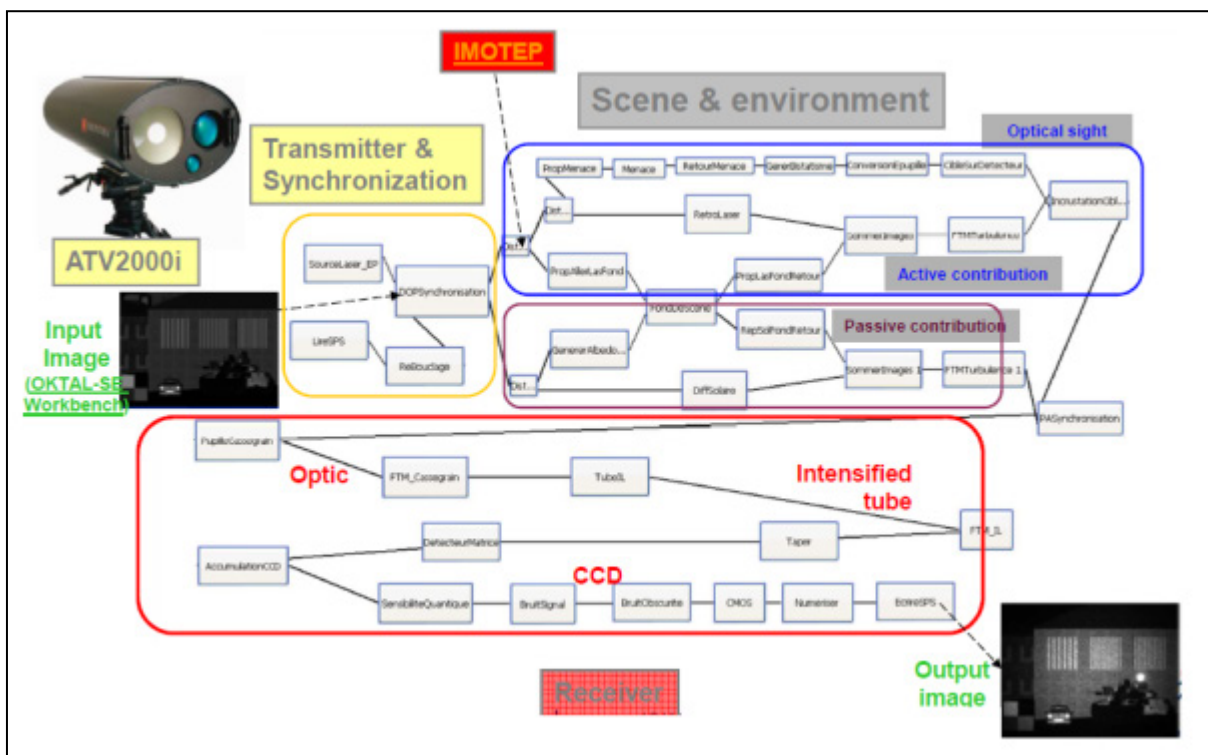
Figure 3-10: Example of ATV2000i Model Detailed Scheme in AMoCO.

3.1.3 Germany Fraunhofer IOSB

The model developed at IOSB to perform imaging simulation of active electro-optical system rests upon the propagation of a laser beam through atmospheric turbulence using the Fast Fourier Transform (FFT) split step method. Intensity distribution at the detector is obtained through backward propagation of the reflected intensity at the target using an empirical model. In the following a more detailed explanation of the model is given.

The FFT split step method is a well-established model to simulate coherent electromagnetic wave propagation through atmospheric turbulence [21]. It leverages the simplified expression of the wave propagation equation in the Fourier domain. In this framework, the Fourier transform of the complex wave amplitude after a finite propagation distance in vacuum is a simple multiplication of the Fourier transform of the input complex wave amplitude with a so-called Fourier propagator. This Fourier propagator scales the Fourier transform of the complex amplitude depending on the distance to propagate, the wavelength and the angular (spatial frequency) spectrum of the propagating wave.

Phase disturbance on the laser beam is a three dimensional distribution. In the FFT split step method this 3D phase disturbance is integrated into a finite number of two dimensional, infinitely thin phase screens, through which the laser beam propagates. Each phase screen is therefore the integrated phase disturbance over a finite distance. The underlying statistics of the phase variation over each phase screen is not only a function of the distance over which the phase disturbance is integrated but also a function of the refractive index structure constant C_n^2. Additionally the type of laser beam wavefront and the type of atmospheric spectrum assumed for the phase power density also influence the actual phase distribution over the phase screens. Last but not least the propagation model takes into account phase screen shifting due to transversal wind.

The FFT split step method earns its name from the step-wise application of the Fourier propagator on the complex wave amplitude in Fourier space and the phase disturbance on the complex wave amplitude in real space.

The target illuminated by the laser beam is assumed to have a Lambertian reflectance. Furthermore in the model adopted by IOSB presented here, the reflection at the target is assumed to shorten the coherence time of the incoming wave in such a way that the reflected light can be assumed to be incoherent.

Imaging of the reflected intensity is performed using an empirical turbulence model developed previously [22]. In short, this empirical model is based upon the analysis of imaging distortions in real image sequences recorded under different atmospheric conditions. The parameters upon which the distortions were characterized are mainly refractive index structure constant and wind but also detector dependent parameters such as detector integration time and camera frame rate. Each pixel from the detector is illuminated from a signal stemming from different areas of the scene. These areas are given an effective range. This pixel-wise range information or range map also enters the parameter list of the empirical turbulence simulator.

To simulate imaging of a scene emitting incoherent light, this empirical model gives, for a given atmospheric scenario, detector parameters and range map, the first and second order statistical moments of imaging distortions. A random noise generator is then used to apply a set of distortion samples from these statistical moments on a set of pristine images, that is, on the set of images that would be recorded if there were no turbulence.

The back propagated intensity distribution recorded this way at the detector is the temporally fluctuating reflected intensity distribution distorted according to the distortion statistics given by the empirical turbulence model

Figure 3-11 illustrates the workflow of the simulation tool developed at IOSB to perform imaging simulation of active electro-optical systems.
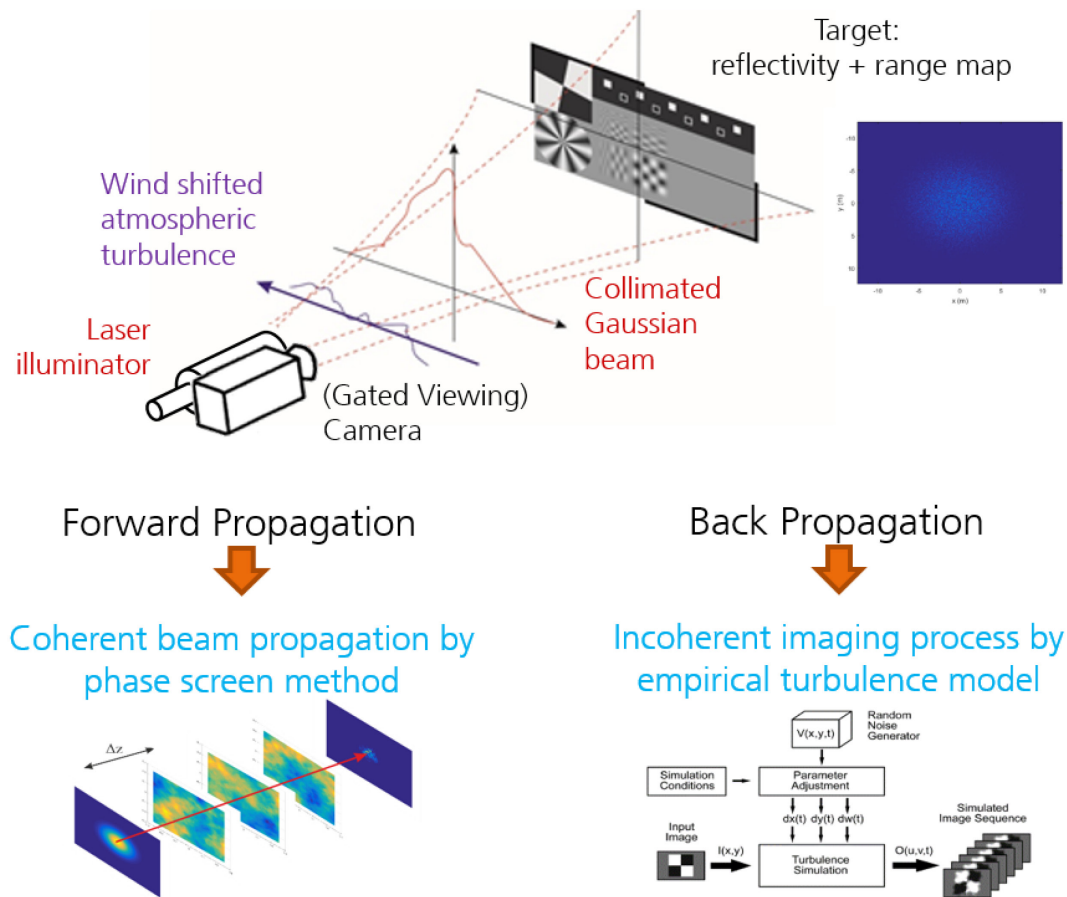
Figure 3-11: IOSB Simulation Tool Workflow.

3.1.4   Swedish Defence Research Agency (FOI)

At FOI, a simulation tool called FOI-LadarSim has been developed during several years [23]. FOI-LadarSim has been adapted for different types of active imaging systems including 1D, 2D, and 3D systems. A recent development addresses the modelling of photon counting LIDAR [9]. During 2017 improvements were done to speed up parts of the simulation for generation of the detector response. LadarSim has been used for different applications for both linear and photon counting LIDAR in air, sea, and land scenarios [9], [10]. LadarSim consists of a collection of modules for:

- Description of the sensor including the laser transmitter and receiver. The module describes values for parameters as the laser pulse energy, pulse length, divergence, beam profile, detector response, cross-talk between detector pixels, detector gain, noise characteristics, and field-of-view.

- Description of atmospheric parameters and background light.

- Description of the position and orientation of targets and other objects in a scene. Objects can be added, moved, or removed during a simulation.

- Description of the sensor position, aiming direction (or scanning) and its movement during a simulation.

- Execution of the simulation, which includes e.g. raytracing and convolution of signals with the sensor system response (in time and spatial dimensions).

- Analysis of simulated data.

The majority of the modules in LadarSim are implemented in MATLAB except for modules for import of 3D-models, assemblage of the 3D-scene (from 3D-models) and raytracing between the sensor and the objects in the scene. These parts (modules) are performed by another tool developed at FOI called SceneServer [24].

A schematic illustration of the communication between MATLAB and SceneServer is shown in Figure 3-12. MATLAB communicates with the SceneServer application through a Java-library which is connected to an interface in SceneServer. The 3D graphics (for operator control) is visualized with Open Scene Graph (OSG), which in its turn uses OpenGL. OSG is a platform independent library used for real-time visualisation. OpenGL is a software interface for creation of computer graphics in 2D and 3D. Rendering of the 3D scene for operator control (screen visualization) is done on the GPU (Graphics Processing Unit) while the raytracing for the sensor simulation is performed by the CPU (Central Processing Unit). The LadarSim concept offers flexibility in that the loading of 3D models and building of the 3D scene is done by SceneServer while placement commands/manipulation of the scene is performed with commands from MATLAB (movement of sensor or targets, change of reflectance for individual scene objects, etc.). SceneServer/OSG can handle many 3D model file formats. Because the raytracing part of the simulation if performed on CPU, the LadarSim execution can be quite time consuming for large scenes with many detailed objects, in combination with high sensor resolution.
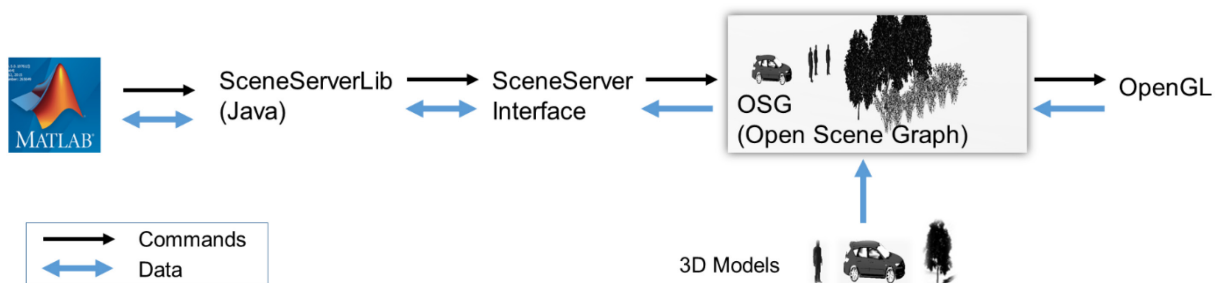
Figure 3-12: Schematic Illustration of the FOI-LadarSim Communication Architecture.

3.1.5   US Army Night Vision and Electronic Sensors Directorate (NVESD)

This section outlines the tools used by NVESD in their active system simulations, as well as an overview of the 1D, 2D, 3D (static and "on the move") simulation results. Note that none of the NVESD simulations include turbulence, since the simulation tools used assume a time-averaged turbulence blur instead of a random realization based on phase. Turbulence efforts were left to other members, who could then apply their phase screen solutions to the simulated imagery presented here.

The Digital Imaging and Remote Sensing Image Generation (DIRSIG) model is a first-principles-based, synthetic image generation model developed by the Digital Imaging and Remote Sensing Laboratory at Rochester Institute of Technology. DIRSIG has been developed over the course of over two decades through a combination of internal, commercial and government funding, and is only available for use for US citizens. DIRSIG simulation capabilities include passive single-band, multi-spectral or hyper-spectral imagery from visible through the thermal infrared wavelengths, a mature active laser (LIDAR) simulator, and an evolving active RF (RADAR) simulator. Since DIRSIG is a ray-tracing model at its core, it relies on very basic physics and builds complicated simulations on that foundation. This makes it versatile and very powerful, with high-fidelity and realistic outputs, given high-fidelity inputs. DIRSIG uses Modtran for its atmospheric calculations for full simulations, though simpler models may be used for lower fidelity when full atmospheric simulation is unnecessary. Materials are defined and applied to 3D objects within the scene, with full-spectrum BRDF definition if desired. Figure 3-13 shows an example of the different material reflectance available in DIRSIG.
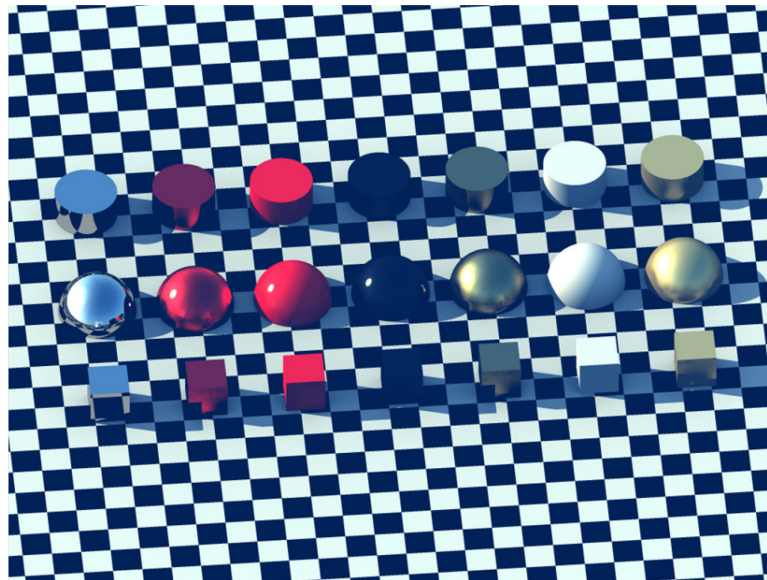
**Figure 3-13: Examples of Different Reflectivity Settings Available in
DIRSIG, Including Specular, Diffuse, and Custom BRDF Modelling.**

In order to simulate active illumination systems, DIRSIG simply builds on its ray-tracing and photon propagation models to add a co-located source at the sensor. Laser propagation is simulated to and from the target, taking into account back-scattering due to atmospheric conditions, and photons may bounce more than once before being collected by the camera. To incorporate multiple bounce (scattering) contributions, DIRSIG employs a modified "photon mapping" approach that tracks total travel time. This process is depicted in Figure 3-14.
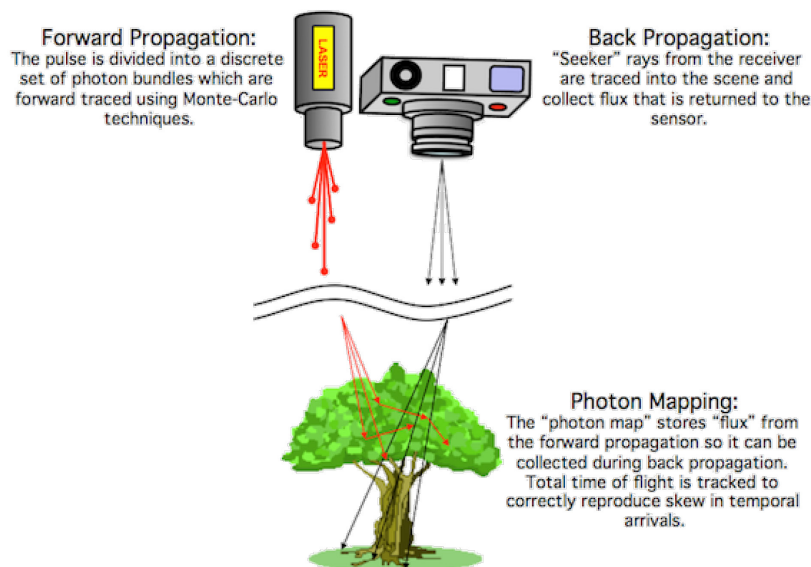
Figure 3-14: Depiction of Active Imaging Simulation in DIRSIG.

Photon arrival time and number of photons per time bin are tracked in the simulation, and can be evaluated in a number of ways to simulate various active imaging modes and systems, including linear- and Geiger-mode detectors with various sources of noise.

3.1.6   US Naval Research Laboratory (NRL)

As in the atmosphere, small-scale variation in density likely caused by temperature and/or salinity in the ocean can lead to localized changes in the index of refraction and can distort Electro-Optical (EO) signal transmission underwater. This phenomenon is well-studied in the atmosphere, where it is generally referred to as "optical turbulence". Less is known about how turbulent fluctuations in the ocean distort EO signal transmissions, an effect that can impact various underwater applications. To circumvent the cost associated with going to sea and finding ideal locations to study such processes, and to shorten system development time, it makes sense to establish a lab environment where controlled settings allows repeatability and intensity at will. This is what prompted the study and implementation of Simulated Turbulence and Turbidity Environment (SiTTE). Once it has been validated both in house and independently, we carried out experiments to investigate beam propagation, and CLS active imaging, leveraging collaborations with NATO SET-219.

3.2   SIMULATION CASE STUDIES

This section presents common scenarios shared by the partners for comparing and evaluating modelling tools.

3.2.1   1D Profiling System

The common scenario is a target placed 2000 meters from the 1D sensor. The characteristics of the sensor are described below. These simulations neglect the turbulence effects.

3.2.1.1   1D Profile Simulation Using FOI-LadarSim

As a complement to measuring a large number of targets, it is possible to obtain additional profiling data from simulations. Dimensions and shapes of targets can be obtained from published sources and CAD-models of objects. To be able to use CAD-model data in a profiling LIDAR classifier, simulations of 1D signatures can be performed to generate typical sensor responses for different conditions (target aspect, sensor instrumental parameters etc.). The simulations will, in this case, drastically reduce the demand for measured signatures. In the following case study, simulations are used to illustrate the profiling result depending on sensor aiming position relative to the target, and the influence from the pulse length of the LIDAR system. For this study, the considered target is given by Figure 2-5.

3.2.1.2   1D Profile Simulation Using DIRSIG

To simulate the 1D time-of-flight profiles for targets of interest, a single-pixel detector was used with 300 GHz timing resolution (exaggerated resolution for the small scale of the targets). The targets used were a 0.05x scaled 737 airplane (to approximate a UAS) and a 0.01x scaled cargo ship as proof of concept. The scaled targets were placed 200 m from the detector, though there is no limitation on size and range of targets for future simulations. Table 3-1 shows the specifications for the active imaging system in the 1D simulation.

Table 3-1: System Specifications for 1D Simulations.

Sensor (Single Pixel)	
Pixel Size	1000 μm
FOV	0.67º or 40.2 arcmin
Receiver Bandpass	1 nm centered at 1064 nm
Gate Resolution	300 GHz
Laser Source (1064 nm)	
Line Width	0.3 nm
Energy Per Pulse	10 mJ
Pulse Width	0.1 ns
Divergence	0.0232 rad (half angle)
Beam Profile	Super Gaussian (radial, 10th order)

3.2.2   Foliage Penetration Imaging

Active imaging has the potential to penetrate through vegetation or camouflage. Imaging of an obscured target is possible if some of the emitted photons from the laser reach the target, are reflected off the target, and propagate back to the receiver. In the case study we have simulated vegetation penetration capability of a photon counting LIDAR sensor.

A scenario was created with the sensor and scene objects placed on ground. The scene objects are three trees and 14 bushes placed in front of the trees (see Figure 3-15). The targets are placed behind the trees, and the targets consist of one car and four persons. Behind the targets a hillside is placed, which serves as an object for counting all detections that are obtained behind the vegetation (not only detections on the targets). The sensor is located 2 km from the scene objects and directed towards the scene objects. A transverse movement of 10 m of the sensor relative to the target area is simulated as schematically illustrated in Figure 3-15.

The main parts of the simulated sensor correspond to similar components in used recent experimental studies at FOI [25]. The experiments were performed for short range imaging with relatively weak laser power and are a development of the previous photon count LIDAR studies at FOI [26]. The main parts of the simulated sensor are a laser and a photon counting 3D camera. The camera utilizes a Geiger-Mode Avalanche Photodiode Detector (GM-APD) [25]. The detector in the camera is a 32-row by 128-column matrix and the time resolution in the camera corresponds to a range resolution of 7.5 cm. The laser wavelength is 1542 nm with 0.57 ns pulse length. In the simulations, a field-of-view of the sensor is selected that matches the target transverse extension at the range of 2 km. The instantaneous Field-Of-View (IFOV) per pixel in the matrix detector is 7.5 cm at the range of 2 km. The trees, bushes and the car, are 3D models obtained from the internet, from https://free3d.com/ and https://archive3d.net/. The scene objects, including targets, hillside, stems, branches, and leaves are given a diffuse reflectance of 10%. The number of leaves on each tree or bush is about 9000, and 3000, respectively. Each leaf is modelled with 5 − 16 triangular faces. In total with all objects, the scene consists of approximately 700 000 3D model faces. The major parts of these faces are required for modelling the trees and bushes. The 14 bushes are arranged in two rows in an overlapping pattern so that the sensor path to the targets are completely unobscured or partly obscured by a combination of one or two bushes, a tree stem, or tree branches and leaves. The smallest parts of the vegetation are the bush branches, with a diameter of about 2 cm and bush leaves with a size of and 4 cm.

The model of the bushes has relatively sparse foliage, allowing partial penetration of photons between branches or leaves. The combination of the trees and the upper part of the bush has very dense foliage and rarely allows photon penetration. Close to the ground photon penetration between the tree stems and bush branches is possible.

The FOI scenario is shown below in Figure 3-15.
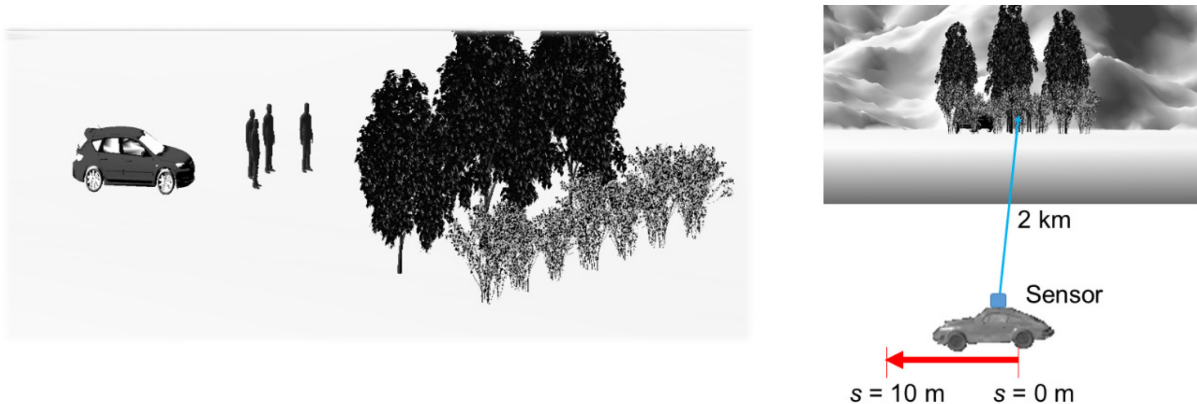
Figure 3-15: A Scene with 3D Models of a Car and Four Persons Behind Three Trees and 14 Bushes (Left); Schematic Illustration of a Scenario with the Same Scene Seen by a Sensor from 2 km Range (Right).

The NVESD scenario is shown below in Figure 3-16.
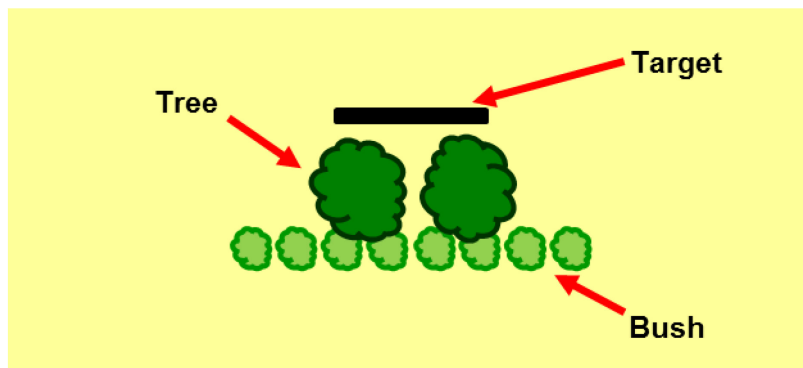
Figure 3-16: Top-Down View of the On-The-Move Scene; "Target" is the DRDC Target with Relief Area (see Figure 3-17).

3.2.3   2D Imaging System and 3D Data Collection System: Test Pattern Panel

DRDC was tasked with designing a 2D target in accordance with requirements from the NATO SET-219 group members. The end result was a panel that contained a combination of Lambertian and weakly specular zones, where the specular zone contains 'bumps' on its surface.

Figure 3-17 shows the 2D target. The upper panel shows the brightness of the target surface. The black and white border is completely black or white, whereas inside the border the black areas are 10% less black and the white areas are 90% white. This is done so that the border may be used to calibrate absolute black and white in the simulations while allowing variations of intensity inside the border.
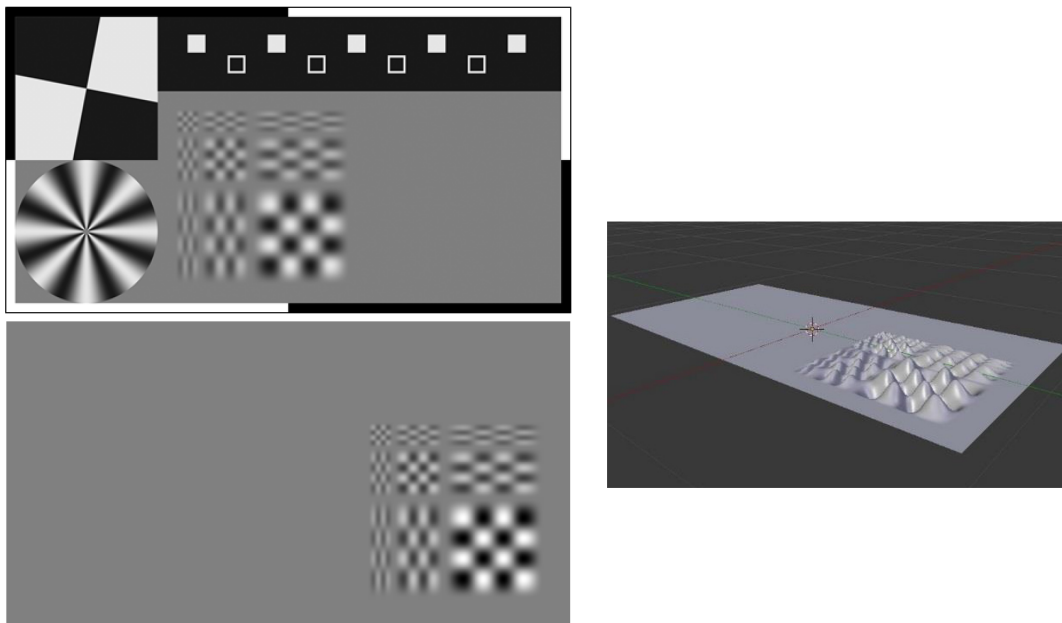
**Figure 3-17: The Target Used in the 2D Simulations. The upper left panel represents
the brightness of the target surface, whereas the lower left and middle
right panel represents a relief map of the bumps on the surface.**

In the upper left corner there is a checkerboard pattern rotated by 11 degrees. This is to enable an evaluation of the MTF of the average image. The lower left corner has a pinwheel pattern to enable an estimate of image resolution. The upper black horizontal band has a sequence of full and open squares to allow for the study of displacement and deformation effects caused by the turbulence. The lower middle portion of the image has a pattern of smooth black and white patches that is repeated with a different scaling in the horizontal, vertical, or both. This pattern is to allow for a wavelet analysis of turbulent effects.

The uniformly grey area in the lower right portion of the upper panel is the weakly specular zone. Its colour is grey but it has bumps that are represented in the relief map in the lower panel of Figure 3-17. Therefore, this area has surfaces that are inclined with respect to the imaging system's line-of-sight, but its specular nature will create variations in the reflected radiance that would not be visible for a Lambertian surface. Consequently, the bump pattern should be visible for the right combination of surface inclination (determined by the difference in height between the crests and the troughs) and the coherence length (which we take to be isotropic). The pattern of bumps is identical to the pattern of brightness patches in the lower middle of the upper panel so as to allow a direct comparison of the two types of turbulence effects (i.e. scintillation of a Lambertian surface with a variation in brightness versus the reflection/scattering off a weakly specular surface with uniform brightness but a variation in inclination). Note that the exact values of the coherence length and inclinations are left to the discretion of each participant.

3.2.4   2D Imaging System: Full Synthetic Scene Simulation

A synthetic 3D scene has been provided by DGA. It has been computed with SE-Workbench, and shared between IOSB and DRDC. Several goals lead to the construction of this scene:

- Realization of a representative field scene, i.e., including target and background;
- Illustration of the simulation of the gating effect, to discriminate the target from the background, and to see the target "silhouette"; and
- Generation of video sequences with time correlation: 5 seconds at 30 Hz (150 images).

The scene is composed by an armored vehicle, trees as background, and a flat grass ground. The target is a full 3D model, with Lambertian optical properties. Each tree is only composed by two textured plans, positioned at 90°. A distance of 20 meters is between the target and the trees.

The level of the background and the target is adjusted to get averaged reflectance of:

- 40% for the ground and background; and
- 20% for the target.

The scene is computed for two distances: 4 and 6 km. Figure 3-18 gives the reflectance maps.
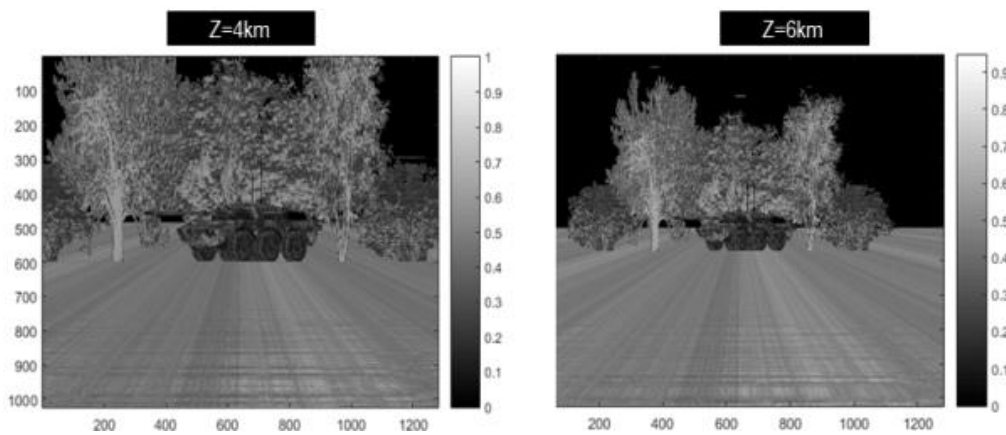
Figure 3-18: Reflectance Maps for 4 and 6 km.

In order to model the gating effect, the distance map is used (see Figure 3-19) for each of the two reflectance maps. The pixel IFOV is 3.1 µrad. All maps have a size of 1280 x 1024 pixels, which is twice the size of the active sensor (640 x 512 pixels).
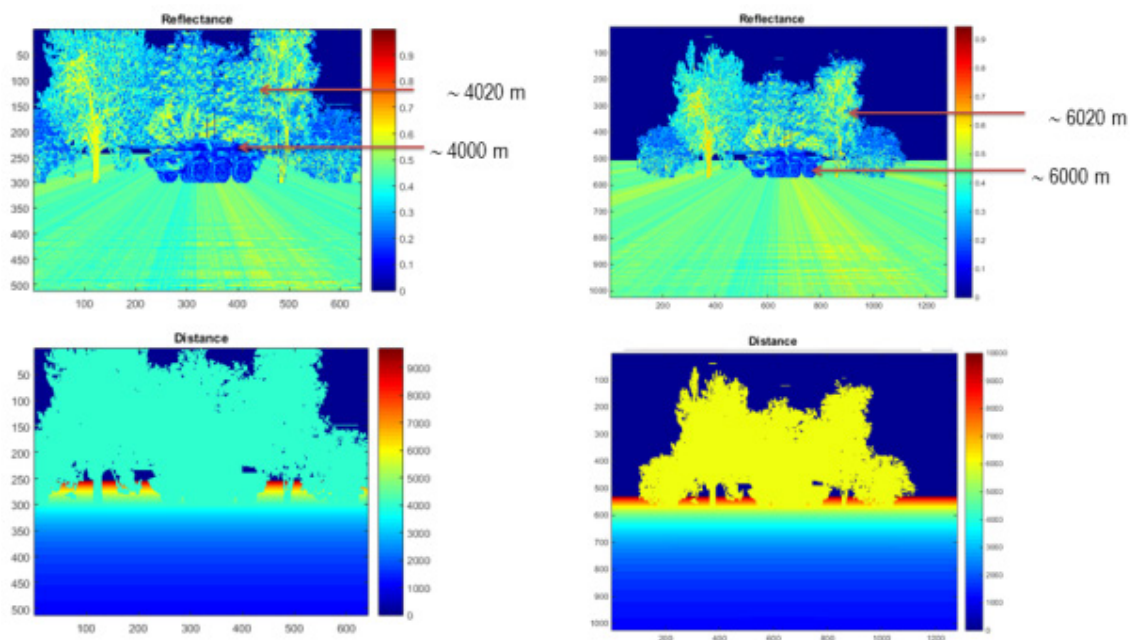
Figure 3-19: Associated Distance Map.

3.2.5 Underwater Imaging Simulation (SiTTE)

SiTTE has been implemented at US Naval Research Laboratory over the last few years and results have been reported [27], [28], [29], [30]. A brief review will be provided here for convenience. The laboratory tank is a standard acrylic water tank with a 5 m length and a height and cross-section of approximately 0.5 m. This tank is unique in that it is outfitted with stainless steel plates at the bottom and top that can be temperature controlled (Figure 3-20, left). This allows for the generation of classical convective Rayleigh–Bénard type turbulence, which is generated by heating and cooling the bottom and top, respectively. The strength of the convective turbulence in the tank is a function of the temperature difference between the top and bottom plates and can be characterized in terms of the Rayleigh number, defined as:

$$Ra = \frac{g\alpha\Delta\mathrm{T}d^3}{\nu D_T}$$
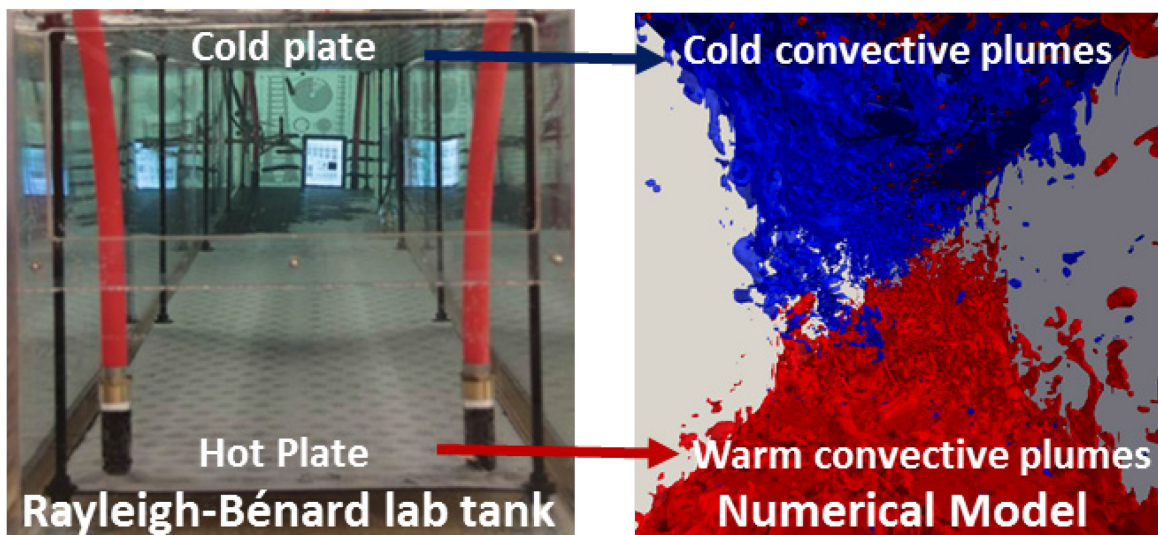
Figure 3-20: View into SiTTE Laboratory Tank at NRLSSC (Left) and Corresponding View from Numerical Model Simulating this Setup (Right).

Here, g is the acceleration due to gravity, α is the thermal expansion coefficient, ΔT is the temperature difference between the plates, d is the distance between the plates, ν is the kinematic viscosity, and D_T is the thermal diffusivity.

The Rayleigh number of the flow can be changed by changing the plate temperatures, and thus the turbulence intensity can be varied. In our experiments, Ra ranges from $1.5\cdot10^{10}$ to around $4\cdot10^{10}$, corresponding to a temperature difference ΔT between the plates of 6 K and 16 K, respectively.

The turbulence in the tank is quantified by high-resolution Nortek Vectrino Profiler Acoustic Doppler Velocimeters (ADV) and fast thermistor probes (PME high-resolution Conductivity-Temperature (CT) probe) (Figure 3-21, left). These instruments provide high-resolution velocity and temperature measurements, at 100 and 64 Hz, respectively. Three Vectrino Profilers and two CT probes were mounted in the tank and collected time series of high-resolution velocity and temperature/conductivity for the subsequent estimation of turbulent kinetic energy dissipation rate ε and temperature variance dissipation rate χ. Data were collected at a sampling frequency of 100 Hz with the Vectrino Profiler and at 64 Hz with the PME temperature probes. To quantify the impact of turbulent fluctuations on optical signal transmission, turbulent kinetic energy dissipation rate ε and temperature variance dissipation rate χ were calculated from the velocity and temperature measurements via spectral fitting to Kolmogorov spectra (for velocity) and Batchelor spectra

(for temperature) following techniques described in references [31], [6], [32], [33], [34], [35]. Turbulent kinetic energy dissipation rate ε and temperature variance dissipation rate χ were then compared to values obtained from the numerical simulations of convective turbulence in the tank and can subsequently be used to assess the impact on the optics and for the estimation of the optical turbulence coefficient C_n^2 [31], [6].
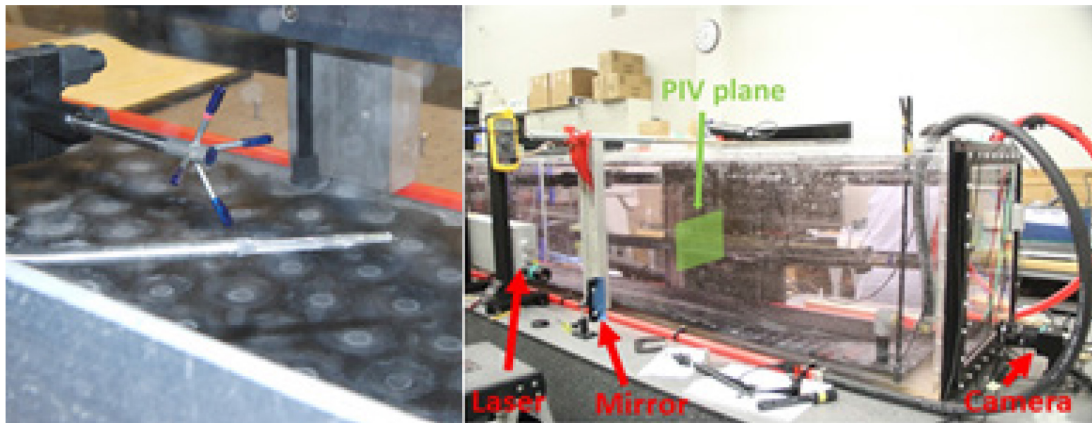
Figure 3-21: Measurement Setup at SiTTE. Left: Vectrino profiler ADV and CT temperature probe. The photo on the right shows the setup of the Particle Image Velocimetry (PIV) system. Here, the mirror is set up to direct the light sheet into the tank at a 90 degree angle to illuminate a cross-section as indicated. Details can be found in Ref. [27].

To complement the sparse laboratory measurements and better understand the large-scale flow field and temperature structure inside the laboratory tank, three-dimensional, very high-resolution, non-hydrostatic numerical simulations using CFD we performed. These simulations can provide full fields of temperature and velocity for the estimation of turbulence parameters and their impact on the optics. The combination of laboratory environment and numerical model provides a well-quantified framework for controlled repeatable experiments.

The numerical tank was implemented in the open-source CFD code OpenFOAM using a Large-Eddy Simulation (LES) approach. In LES, the larger-scale eddies in the flow are explicitly resolved, while the scales smaller than the grid-size are modeled. The traditional Smagorinsky model was chosen as the sub-grid scale model [29]. In LES, a larger portion of the turbulence spectrum is explicitly resolved than in the often used Reynolds-averaged Navier-Stokes (RANS) models (k-ε and others), which, while useful to predict turbulence parameters, do not resolve the smaller flow features and associated eddies. Direct Numerical Simulations (DNS) on the other hand, in order not to be computationally prohibitive for a domain as large as presented here, would be severely underresolved and thus suffer from excessive numerical diffusion. Since it is necessary to resolve the details of the flow and eddying characteristics in the temperature field, in addition to turbulence parameters, to be able to assess the effect on the optics, the LES approach is the preferred way to simulate the setup described in this paper.

Here, we present results from a very high-resolution, millimeter-scale simulation with Δx = Δy = 5 mm, Δz = 2.5 mm, which corresponds to 20 million grid points in the 5 m by 0.5 m by 0.5 m domain. Exploratory simulations at lower resolution (Δx = Δy = Δz = 1 cm) were run on a modern, high-performance, dual six-core Linux desktop, whereas the production runs at the millimeter-scale resolution required High-Performance Computing resources at the DoD Supercomputing Resource Center, due to the high computational cost. A view into the laboratory tank and a corresponding model view are shown in Figure 3-22. The model provides full velocity and temperature fields which can be verified using the laboratory measurements (Figure 3-24).

Figure 3-22: "Numerical Tank" Used to Simulate Rayleigh–Bénard Convection and Emulating the Laboratory Tank Setup. The temperature field is shown as a fly-over around and into the tank visualizing the convective plumes as isovolumes colored by temperature range 293.6 K to 294.4 K (top and middle rows). The bottom row shows the same isovolumes colored by vertical velocity range -0.034 m/s to 0.0266 m/s. Frames are at model times t = 80 s, 200 s, 310 s, top row left to right, and 70 s, 330 s, 880 s both bottom rows, left to right. The tank dimensions as shown are 5 m (x, horizontal along tank axis) by 0.5 m (y, horizontal across tank axis) by 0.5 m (z, vertical tank axis).

The laboratory tank allows the variation of plate temperature for a wide range of temperature differences ($\Delta T = 2°C$ to $\Delta T = 16°C$). We focus here on presenting results for two cases of turbulence strength. The lower strength turbulence, corresponding to Rayleigh number $Ra = 1.5 \cdot 10^{10}$ and a temperature difference between the plates of $\Delta T = 6$ K and the extreme turbulence case with $Ra = 4 \cdot 10^{10}$ with the highest temperature difference we can achieve in the tank $\Delta T = 16$ K (Figure 3-23).

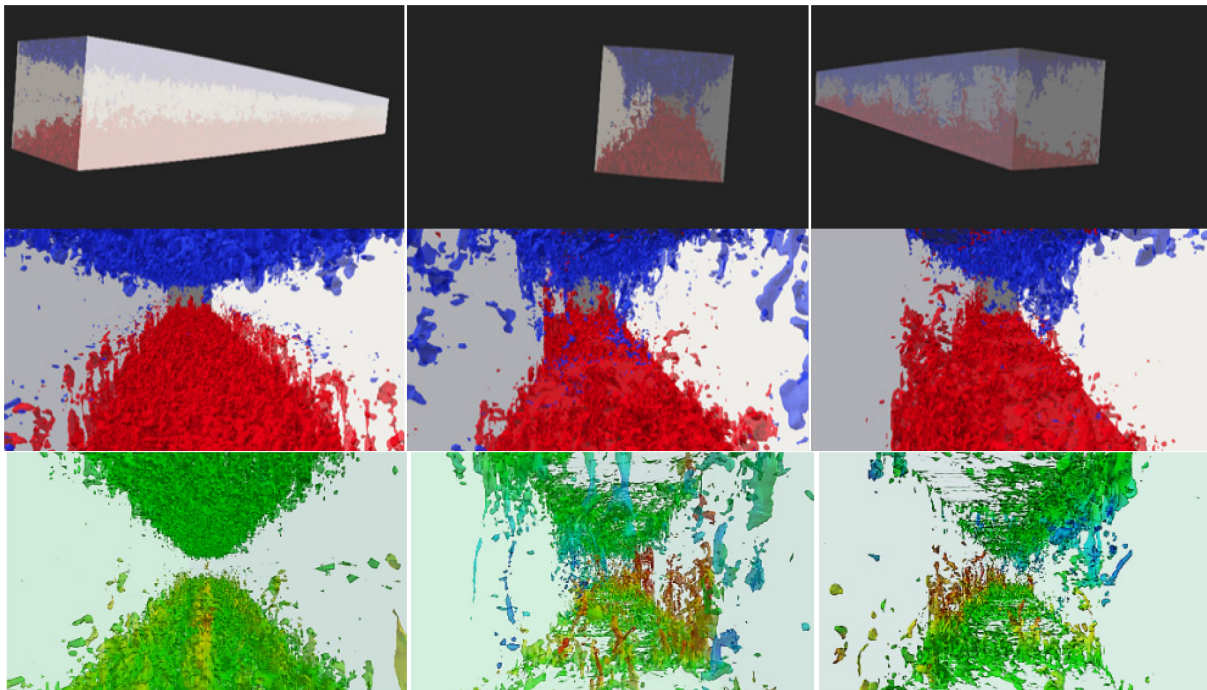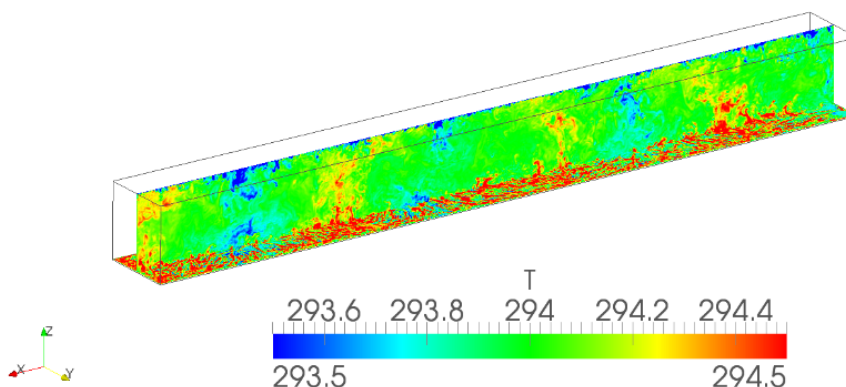**Figure 3-23: "Numerical Tank" Used to Simulate Rayleigh–Bénard Convection and Emulating the Laboratory Tank Setup. The temperature field (in K) is shown and several convective plumes are visible. Top is for a "lower" level of optical turbulence ($\Delta T = 6°C$) and bottom is the "extreme" ($\Delta T = 16°C$) level of turbulence.**

3.2.6 Beam Propagation Model

The propagation of light in oceans and lakes is limited due to absorption, diffuse scattering, and optical distortions as a result of the presence of inhomogeneities in the index of refraction. Despite these difficulties, the need for high bandwidth communication and high-resolution imaging has maintained a continued interest in underwater optics and photonics [32], [33].

Here we present a comprehensive study of beam propagation simulations and lab experiments of a focused Gaussian beam propagating through varying degrees of optical turbulence intensities. For the computational part of the investigation, a true end-to-end simulation was performed, starting with a CFD simulation of Rayleigh–Bénard convection. The simulated temperature fields were converted to index of refraction phase screens, which then were used to simulate the propagation of a focused Gaussian laser beam via the split-step Fourier method. Lab experiments where conducted using the same parameters as in the simulation using a good quality Gaussian beam and a CCD camera to record data. As shown in Figure 3-24, the physical RB turbulence tank with the water cooled/heated plates on the top/bottom. Also shown are the optical quality and anti-reflection coated windows which allow for an undisturbed entry/exit of light into the tank. Light can be passed either through the long (5 m) dimension of the tank or across the tank for a propagation path of 0.5 m. The turbulence strength is controlled by setting the temperature of the hot bottom plate and the cold top plate while the turbidity can be set by the introduction of scattering particles.
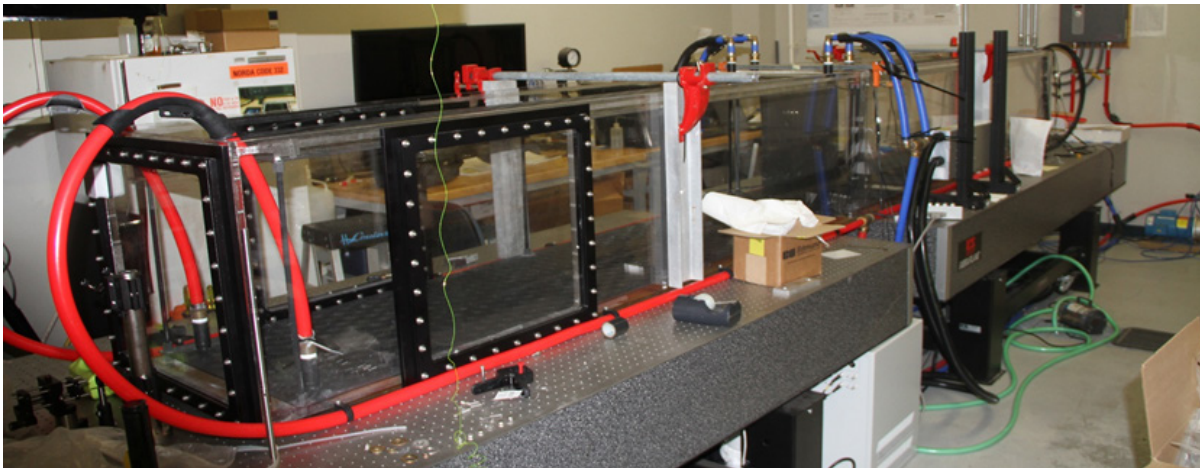
**Figure 3-24: Rayleigh–Bénard Tank with Water Cooled and Heated Top and Bottom Plate.
Also shown are the optical quality windows and the PIV setup on the far side.**

The same geometry as the physical tank shown in Figure 3-24 is simulated via numerical methods on a high performance computer, involving 20-million grid points at mm resolution. A snapshot of the simulated temperature profile as well as the time averaged temperature profile is shown in Figure 3-25. Also shown in Figure 3-25 is the time average velocity profile in the vertical plain along the long dimension of the tank. Lastly, the logarithm of the index of refraction structure constant (C_n^2) in the same plain is plotted.
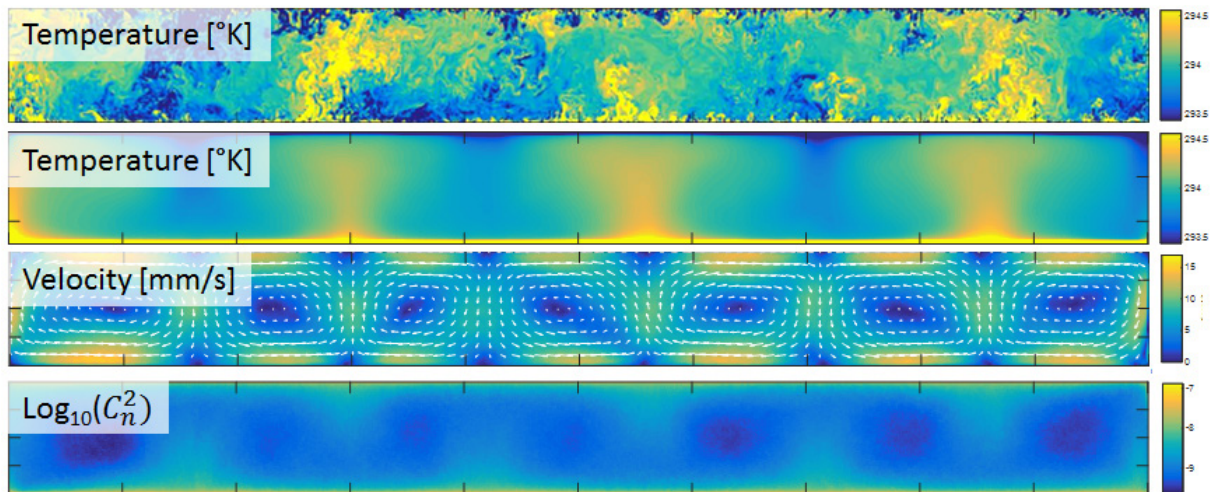
Figure 3-25: (Top to Bottom) Along-SiTTE View of Simulated Instantaneous Temperature, the Time Averaged Temperature, the Time Averaged Flow Velocity, and the Time Averaged Index of Refraction Structure Constant.

Chapter 4 – SIMULATION CASE STUDY RESULTS

4.1   1D PROFILING SYSTEM

4.1.1   1D Profiling Results Using FOI-LadarSim

Examples of simulated 1D range profiles from a UAV CAD-model are shown in Figure 4-1. The length and wingspan of the CAD model is same as for the mock-up model (Figure 2-5), but the wings are placed slightly further back on the CAD model than on the mock-up model. The simulations in Figure 4-1 are performed for a sensor to target range of 2 km. The square boxes in the figure indicate the aiming position and footprint of the LIDAR receiver (FOV) relative to the target. Similarly, the white circle shows the aiming position and the beam width of the laser transmitter. The beam cross-section is Gaussian and the circle shows the Full Width at Half of Maximum (FWHM) of the beam cross-section. The figure illustrates how a vertical or horizontal aiming offset affects the 1D profile. It is seen that the relative intensity of the first peak (nose) to the second peak (wings) changes with changing aiming offset. For the horizontal offset of 0.6 m, the peak intensity from the wings is almost unchanged while the intensity from the nose peak is significantly reduced, compared to the aiming position at the centre of the target. It can be noted that the nose peak is significantly stronger than the wings peak in the experimental data (Figure 2-5), while the nose and wings peaks have more close intensity values in the simulated data (Figure 4-1). The difference between the experimental and simulated data is explained by a slightly different target aspect towards the sensor. In the experiment, the UAV body did not point exactly towards the sensor. It is also noted that the tail fin peak is difficult to distinguish in the simulated data, which is partly caused by a slightly smaller separation between the wings and the tail fin for the CAD model compared to the mock-up model. The target aspect (physical model not perfectly aligned towards the sensor) is also in part an explanation for this difference.

To more clearly separate the peaks from different parts of a small target, it is beneficial to use a profiling LIDAR with a shorter laser pulse [9]. In Figure 4-2 we show simulation examples with a laser pulse length of 6 ns (similar to Figure 4-1) compared to the results with a 3 ns pulse (FWHM). The simulation setup with profiles for different aiming offset positions on the target is similar to Figure 4-1. Figure 4-2 shows that the tail fin echo peak is clearly distinguishable from the first two peaks when using a 3 ns pulse. The tail fin peak is preserved for all aiming offsets up to 0.6 m, but significantly reduced in intensity for the horizontal offset of 0.6 m. A vertical offset aiming position 0.6 m above the centre of the UAV body will not significantly reduce the tail fin echo peak intensity.
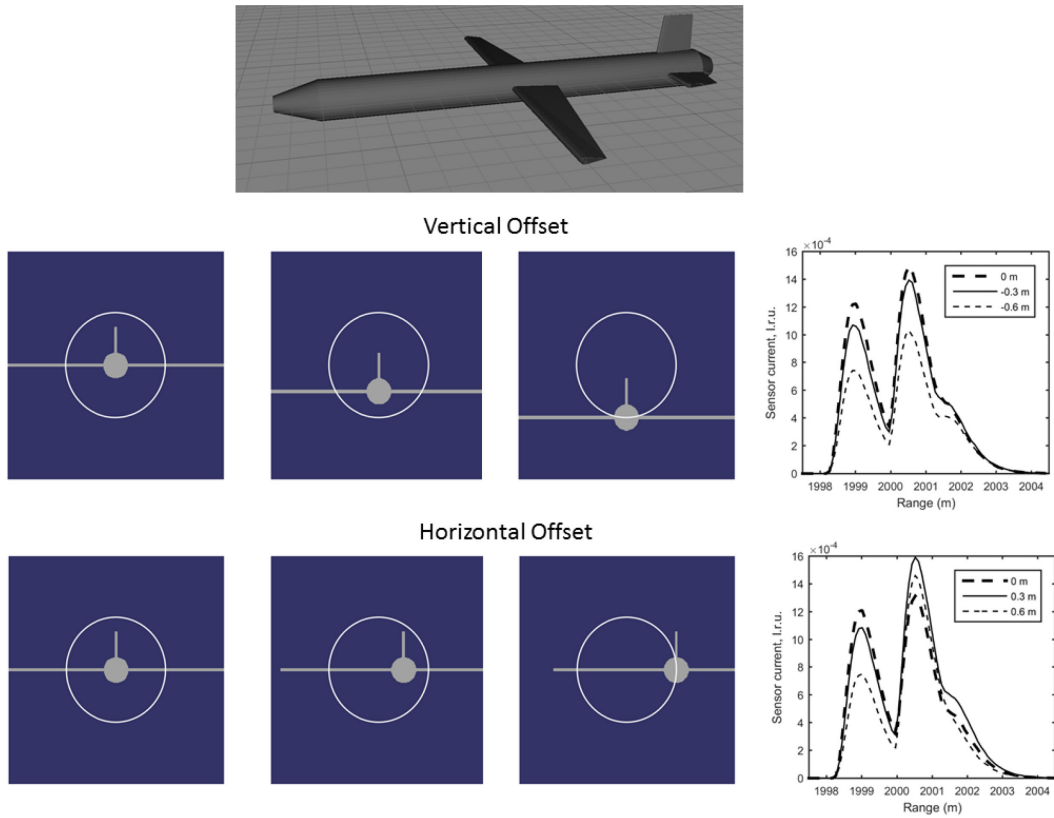
Figure 4-1: Simulation Examples of 1D Profiling of a UAV Target – (Upper Figure) 3D Model of the Simulated Target; (Middle and Lower Panels) Aiming Positions and Profiles (Right) Depending on the Target Position Relative to the Sensor Aiming Position. White rings indicate the width (FWHM) of the laser beam cross section. A pulse length of 6 ns FWHM was used in the simulations.
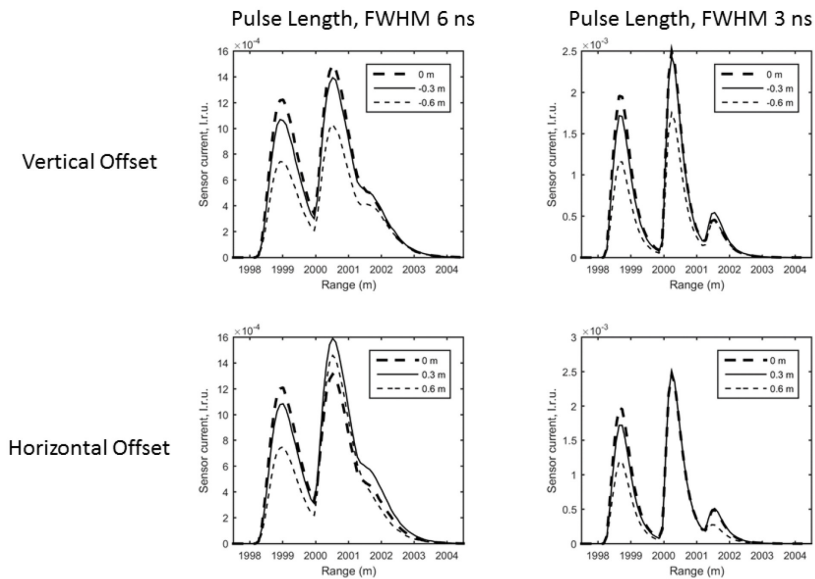
Figure 4-2: Simulation Examples of 1D Profiling of a UAV Target – Range Profiles Depending on the Target Position (Vertical or Horizontal Offset) Relative to the Sensor Aiming Position (c.f. Figure 4-1). Figures on the left show results using a pulse length of 6 ns FWHM and figures on the right show the corresponding results for a 3 ns pulse.

4.1.2   1D Profile Results Using DIRSIG

Figure 4-3 shows the 1D time-of-flight profiles for returns from the scaled 737 and the scaled cargo ship, along with narrow-band equivalent images, simulated with a passive camera, to show the relative orientation of each object in the field of view.
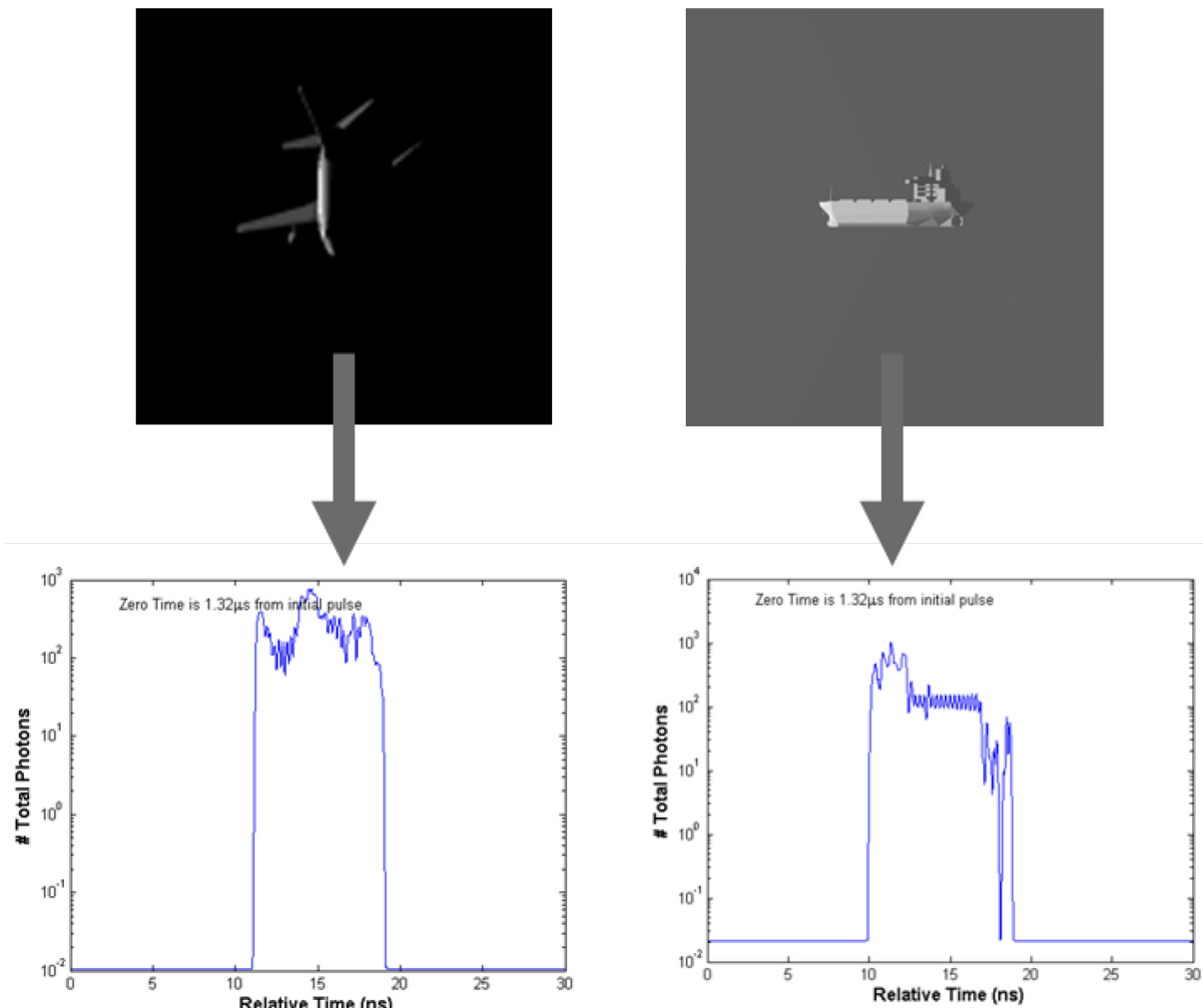
Figure 4-3: 1D Profiles Results for a 0.05x Scaled 737 Airplane (UAS Stand-In) and a 0.01x Scaled Cargo Ship. *x* Axes show time of flight and *y* axes show number of photons collected per time bin (300 GHz).

4.2   FOPEN

Examples of simulation results for the FOPEN scenario (Figure 3-16) are shown in Figure 4-4 – Figure 4-9. Several simulation runs were performed with different laser pulse energies; 0.125 µJ, 0.25 µJ, 1 µJ, and 4 µJ. For each pulse energy level, sensor data collection was performed for 50 laser pulses each 0.5 m from $s = 0$ m to $s = 10$ m along the red arrow in Figure 3-16, i.e. from 21 sensor positions. Figure 4-4 shows the result from one sensor position ($s = 0$ m) and two different pulse energies. In this figure the time histogram for detections (photon counts) are shown as the sum of counts for all pixels in the matrix detector. Thus the total and maximum number of counts over all time bins is 204 800 (32 x 128 (pixels) x 50 (pulses)). For both energy levels, 0.125 µJ and 4 µJ, groups of peaks in the histogram can be identified as originating from the

vegetation, the targets, or the background as indicated in Figure 4-4. It can be noted that the ratio between the maximum target peak intensity and the maximum vegetation peak intensity is higher for the low pulse energy case (0.125 µJ) compared to the higher pulse energy case (4 µJ). The explanation to this is that a strong return from the foliage (vegetation) will saturate the detector and thus limit the possibility to detect the partly obscured target even if photons from the target reach the detector [25]. In Figure 4-5 the simulation results for four pulse energy levels are shown, presented as local Time-of-Flight (ToF) for each pixel in the detector. The results are from simulated data from only one sensor position ($s = 0$ m). The local ToF is defined as the time bin for the peak with the maximum intensity in the time histogram for each pixel. A limit of at least 3 detector counts in the same time bin is used for detection of a peak. The result in Figure 4-5 is based on 50 simulated laser pulses for each pulse energy level. In Figure 4-5, reflections from the vegetation, targets, and background are respectively coloured light blue, light green, and yellow (c.f. the time scale in Figure 4-4). The dark blue pixels in Figure 4-5 denotes "no detected" peak. The figure shows that too small of a pulse energy will result in very few pixels with a peak intensity large enough to detect the surface of an object. With increased pulse energy, the number of pixels with a detectable histogram peak increases.
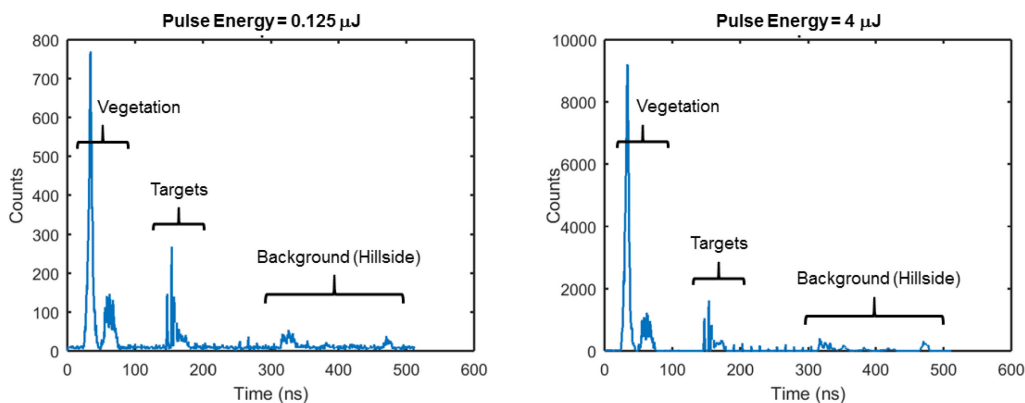
Figure 4-4: Time Histogram for Detections from the Matrix Detector. The time on the *x*-axis is shown as local Time-of-Flight (ToF) within a range gate placed over the vegetation, targets, and background. The number of counts on the *y*-axis is the total detector counts for all pixels in the 32 x 128 matrix detector. The result is based on 50 simulated laser pulses. Simulation results are shown for two different pulse energy levels.
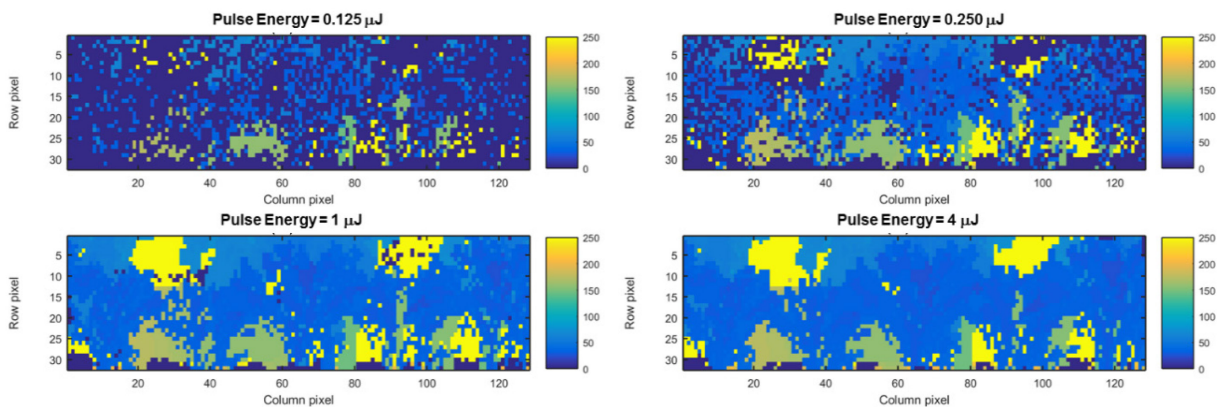
Figure 4-5: Simulation Results in the Matrix Detector for Four Different Pulse Energy Levels. The colour code represents local Time-of-Flight (ToF) in nanoseconds. The local ToF is defined by the maximum peak in the time histogram (detector counts) for each pixel. A limit of at least 3 detector counts in a time bin is used for detection of a peak. The result is based on 50 simulated laser pulses.

For foliage penetration, saturation effects in the detector may occur from the vegetation, which suggests that an optimum pulse energy is used that maximizes the probability of detection of targets behind the vegetation [36]. For analysis of the pulse energy influence we have calculated the foliage fill factor for each pixel in the detector matrix. The foliage fill factor is defined as the fraction of the FOV occupied by the foliage [36]. For detailed analysis in simulation studies, the foliage fill factor can be calculated for each individual pixel in the sensor [25]. An example of calculated values is shown in Figure 4-6. The calculation is realized based on the simulation method where we use several subpixels for each simulated physical (sensor) pixel. In our study we have used 4 x 4 subpixels for each sensor pixel. In the simulation, raytracing is performed for each subpixel. The data in the left part of Figure 4-6 is directly obtained by calculation of the ratio of subpixels $(0 - 16)$ to all subpixels (16) that are obscured by part of a stem, branch, or leaf in the vegetation. With a subpixel resolution of 4×4 subpixels we can thus calculate 17 fill factor levels $f = [0, 1/16, ... , 15/16, 1]$. In the right part of Figure 4-6 is shown the distribution of foliage fill factor values over all pixels. Many pixels are either completely unobscured ($f = 0$) or completely blocked ($f = 1$) by the vegetation. Relatively low f values ($0.06 < f < 0.4$) occur for pixels partly obscured by the thin branches of the bushes. We note that the 2 cm size of these branches subtend a relatively small part of the approximate 7.5 cm sensor pixel size. Moderate to high f values (larger than about 0.5) occur for pixels on the upper part of the bushes and on the trees. By combining the simulated detector counts and the calculated foliage fill factor, we can analyse the influence from pulse energy on the foliage penetration capability.
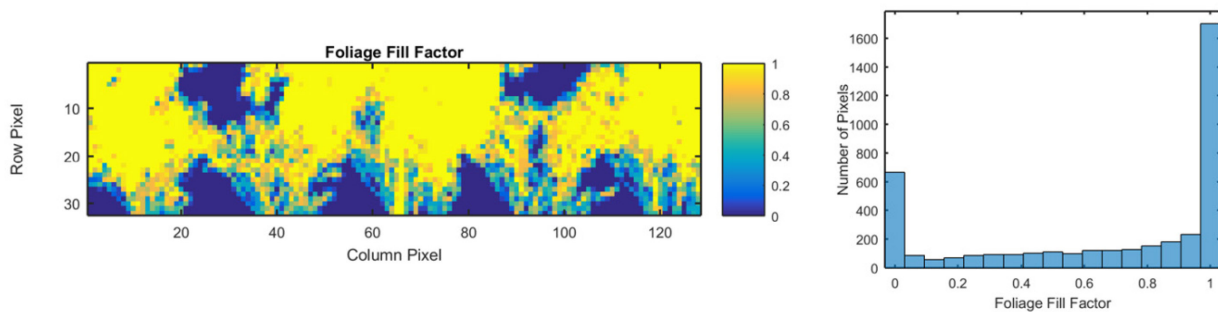
Figure 4-6: (Left) Example of Calculated Foliage Fill Factor Seen by the Matrix Detector; (Right) Distribution of Foliage Fill Factor Across All Pixels in the Matrix Detector. In each pixel the calculated value is the ratio between the number of subpixels subtended by vegetation (within the "vegetation" range according to Figure 4-4) and the total number of subpixels. In this simulation 4 x 4 subpixels were used.

An example of such combined data is shown in Figure 4-7 which is based on a simulation with 50 laser pulses in one sensor position. The target and background (hillside) detection probability is plotted as a function of pulse energy and foliage fill factor. The figure shows that pixels with low foliage fill factor f or unobscured pixels ($f = 0$) results in a high optimum pulse energy (e.g. 4 μJ). Lower pulse energy (e.g. 1 μJ) is required to maximize the penetration for pixels with high foliage fill factor. The right part of Figure 4-7 shows the result zoomed in for high values of the foliage fill factor, and shown as a function of the total detection probability in the matrix. The total detection probability is the number of detector counts for the whole matrix divided by the number of pixels in the matrix. To the right in of Figure 4-7 the black vertical thick lines indicate the optimum detection probability according to theoretical results by Johnson [36]. Our simulated results of optimum pulse energy correspond well to these theoretical results.
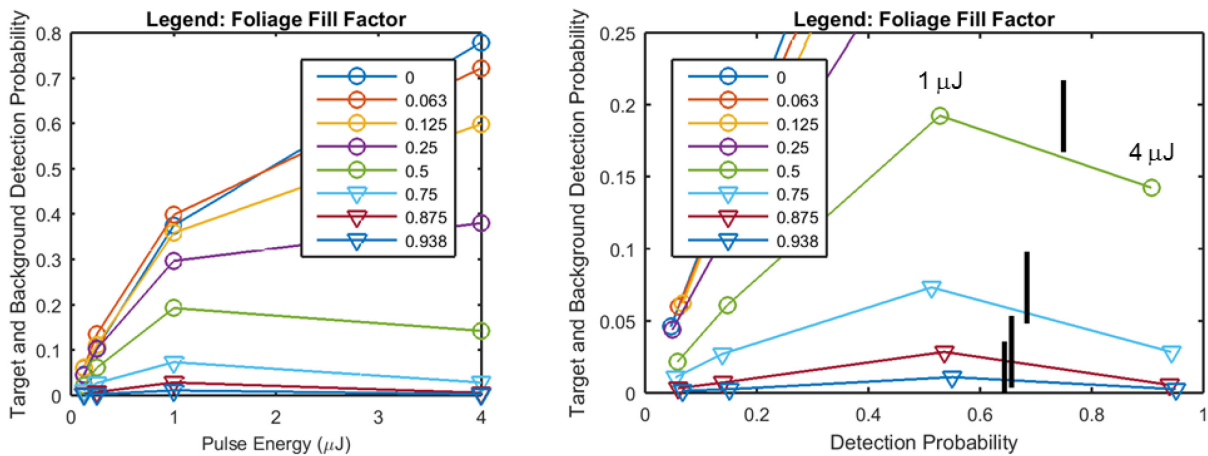
**Figure 4-7: Simulation Results of Penetration Detection Through Vegetation
for Different Foliage Fill Factor and Pulse Energy Values.**

On the y-axis is shown the ratio between detections that occur either from the target or the background (hillside) (c.f. Figure 4-4), and the product of the number of laser pulses (50 pulses) and the number of pixels. The data is grouped pixel-wise according to its respective fill factor based on the data shown in Figure 4-6. The left figure shows the result as a function of pulse energy. In the right figure the result is zoomed in for high values of the foliage fill factor and shown as a function of the total detection probability in the matrix detector. In the right figure the vertical thick lines indicate the optimum detection probability according to Johnson [36]. The simulated data is generated with zero background noise and zero dark counts in the detector, and only for one sensor position $s = 9$ m (c.f. Figure 3-15).

For visualization of the penetration capability and the influence from sensor movement, we have transformed the range results from each sensor position ($s = 0$ to $s = 10$) to 3D points in an "earth-fixed" coordinate system. Example results for two different pulse energy levels are shown in Figure 4-8. The colour scale of each 3D point denotes the intensity of the peak in the time histogram for a pixel (c.f. Figure 4-4, showing a histogram example for all pixels in the detector). In Figure 4-8(a) using 1 μJ pulse energy it is seen that more 3D points are obtained from the targets than using 4 μJ in Figure 4-8(c). The additional points in (a) compared to (c), originate from pixels which are partly obscured by vegetation. Figure 4-8(b) and (d) show the corresponding data accumulated along the 10 m sensor movement (direction along the red arrow in Figure 3-15). The results are based on simulations with 50 laser pulses each 0.5 m from $s = 0$ to $s = 10$ (21 positions).

By placing the 3D points (Figure 4-8) in a voxel grid with 5 cm grid side, the number of new "unique" points for each sensor position can be analysed. We define a new unique point, and add this point, only if the voxel does not contain a previously collected 3D point. The result from this analysis is shown in Figure 4-9, where the left part shows the number of new unique points for each movement step and the right part shows the accumulated number of unique points. The number of 3D points at the sensor start position ($s = 0$ m) was 765 and 665, respectively for 1 μJ and 4 μJ pulse energy. After movement of the sensor to $s = 10$ m, the number of accumulated unique points increases to 2700 and 2160, respectively for 1 μJ and 4 μJ pulse energy. The simulation indicates thus that by decreasing the pulse energy from 4 μJ and 1 μJ, it is possible to increase the number of points on the targets (given a 5 cm voxel grid) with 15% at the start position and with 25% for the total number of accumulated unique points along the 10 m sensor path.
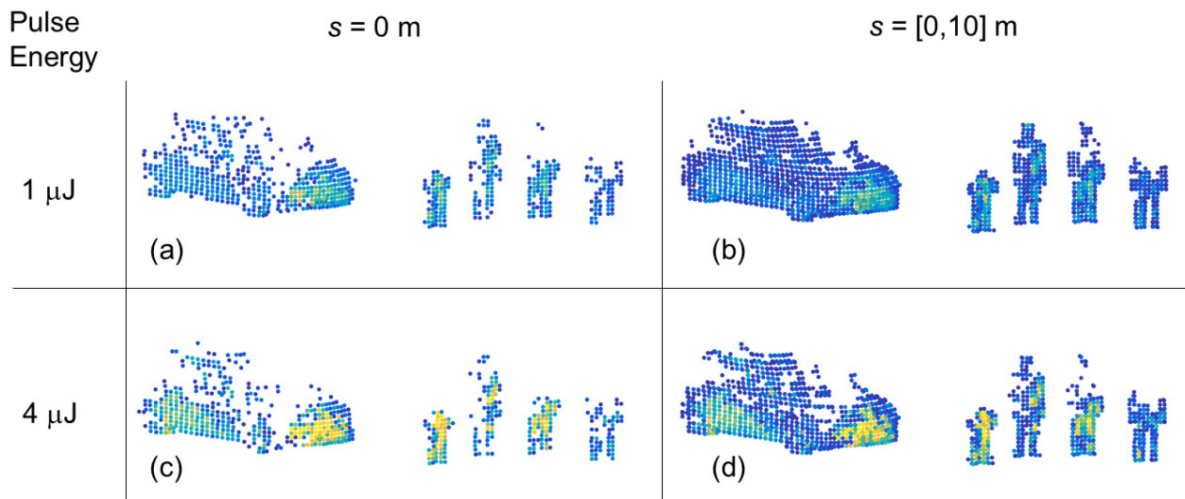
Figure 4-8: Results from Simulations of the Scenario Illustrated in Figure 3-15. Figures (a)-(b) and (c)-(d) show results respectively for laser pulse energy 1 μJ and 4 μJ. Figures (a) and (c) show the 3D points based on peak detections in a range gate over the targets (50 pulses, at start position of the sensor). Figures (c) and (d) show cumulated 3D points from sensor data collection with 50 laser pulses each 0.5 m from s = 0 m to s = 10 m along the red arrow in Figure 3-15.
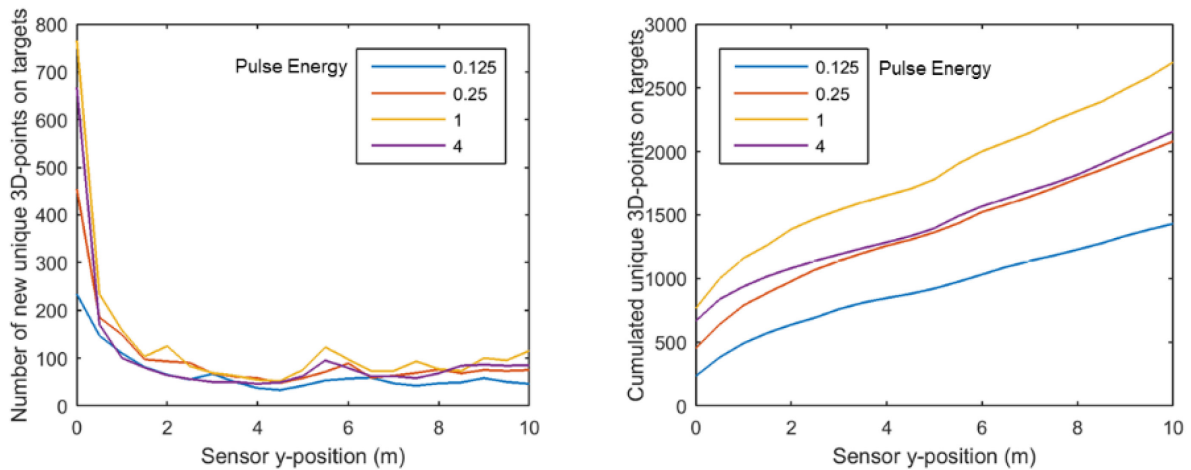
Figure 4-9: Detection Results on Targets (3D Points on Car or Persons) from Simulation of the Scenario Illustrated in Figure 3-15. The left figure shows the number of new unique points for each new position along the red arrow in Figure 3-15. The right figure shows the cumulated number of unique points for the same simulation. Data collection is performed from 50 laser pulses each 0.5 m from s = 0 m to s = 10 m along the red arrow in Figure 3-15.

In addition to the static 3D imagery, a dynamic "on the move" scene was simulated for an occluded target in a very simple setup (a top-down view of the scene is shown in Figure 3-16). In the scene, the bushes and trees had individual leaf and branch components and were rotated with respect to each other. This ensured varied angles of reflection and complex bounce patterns for the returning photons. The sensor system was moved parallel to the plane of the target (DRDC target), which was positioned 1 m above the ground plane. All objects in the scene were assigned realistic reflectivity profiles. Figure 4-10 shows the range and intensity data results from the simulation, taken at the point when the camera line of sight was centered on the target.
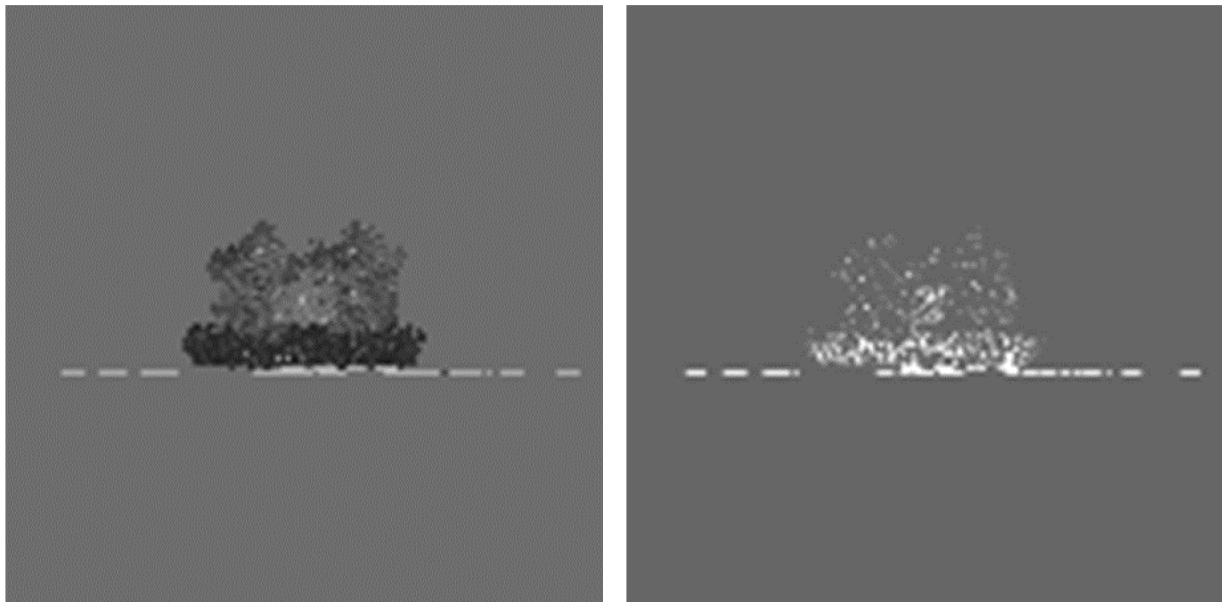
Figure 4-10: Single-Frame Stills from Multi-Frame Collection Showing Range (Left – Darker Objects are Closer to the Sensor) and Intensity (Right) Data for a LIDAR System. The DRDC target can be made out behind the trees in both images.

4.3   TEST PATTERN PANEL

DGA illustrates the benefit of the use of the radial target for the global system MTF evaluation and compare it to the theoretical global system MTF. For that, we assume the following hypothesis in Table 4-1 for the active sensor design. The sensor is based on the characteristic of the Intevac LIVAR M506 sensor, assuming no sun contribution. So the images are computed in digit level from this camera.

Table 4-1: Laser and Receiver Configuration.

Pulse width	1,50E-08	s
Energy	2,00E-02	J
Peak Power	1,33E+06	W
Divergence (1/2 Fov_X)	2,00E-03	rad
lambda	1,57E-06	m

Toptical	65	%
Optical quality	2,3	
pixel size	1,50E-05	m
Num. pixel_X	640	pixels
Num. pixel_Y	512	pixels
Size_sensor_X	9,60E-03	m
Size_sensor_Y	7,68E-03	m
Focale length	2,4	m
F Number	10	
Pupil diameter	0,24	m
Fov_X	4,00E-03	rad
Fov_Y	3,20E-03	rad
Quantum efficiency	25	%
Gain	150	
Tube MTF	Gaussian, 15	lp/mm@50%
Read out noise	200	electron
Frame time integration	100	ns
Digits	10	bits
Filter bandwitdh	20	nm
Sun contribution	0	W
Sun contribution on time integrat	0	J

The MTF of the amplification stage of the sensor is also considered as given by Figure 4-11.
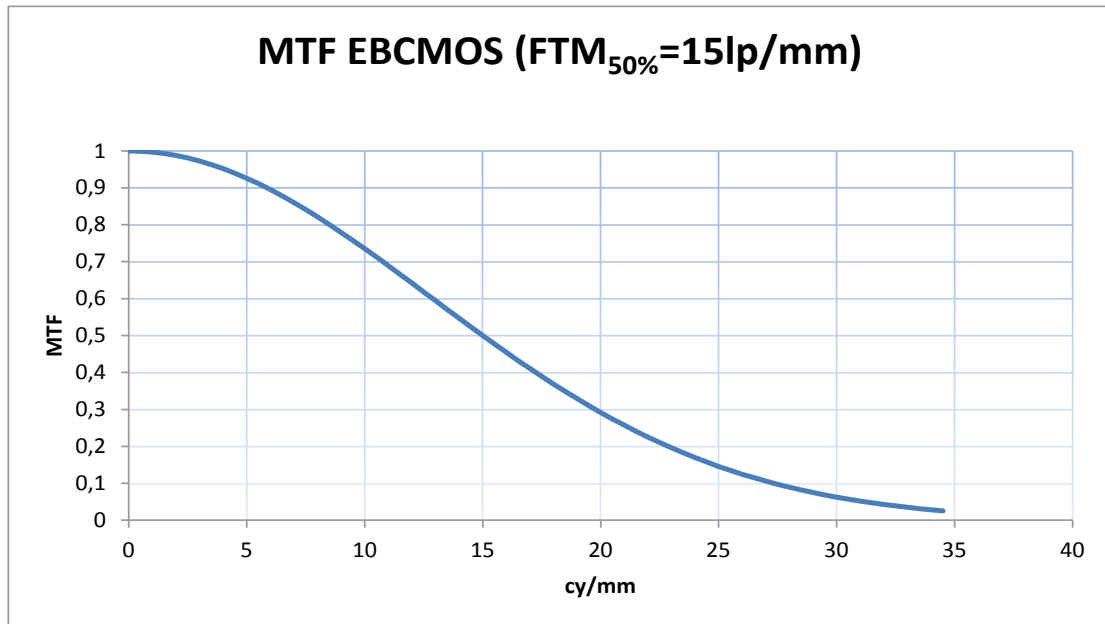
Figure 4-11: MTF of the Amplification Stage of the Sensor.

Note that the modeling chain of DGA does not consider:

- Target speckle effect (supposed negligible); and
- The effect of the 3D bump of DRDC target panel (this area is supposed flat). Moreover, the global target is supposed to be fully Lambertian.

For an easier estimation of the global MTF, the laser illumination is assumed to have a "top hat" spatial profile over the DRDC target. The target size is 1.5 x 0.75 mrad. Also, the analysis of the MTF is made over an averaged image coming from 30 single images, uncorrelated in time. The following plots (Figure 4-12 – Figure 4-14) give the DRDC target averaged image and the sensor MTF profile, measured on the averaged image (blue curve) and the theoretical MTF (red dash curve) of the global system (include long exposure turbulent MTF, sensor and optic MTF). They are given for one level of turbulence ($C_n^2 = 1 \cdot 10^{-14}$ m$^{-2/3}$), and three distances (2, 4, and 6 km).
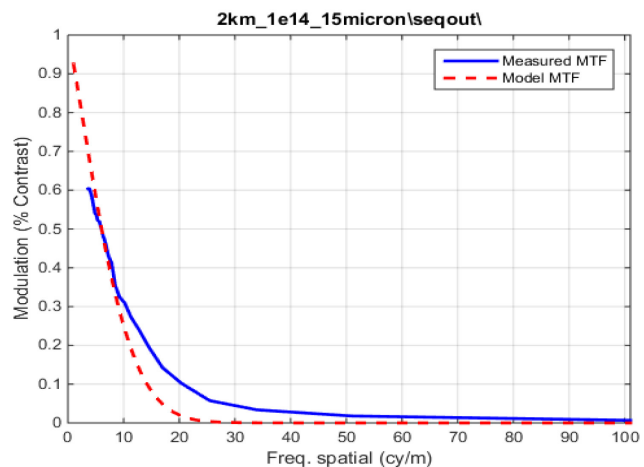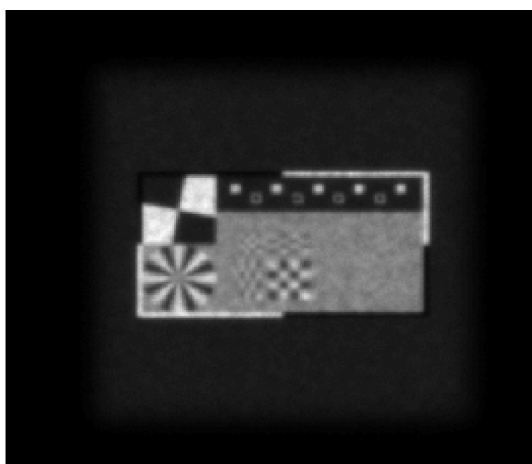
Figure 4-12: Result for 2 km.
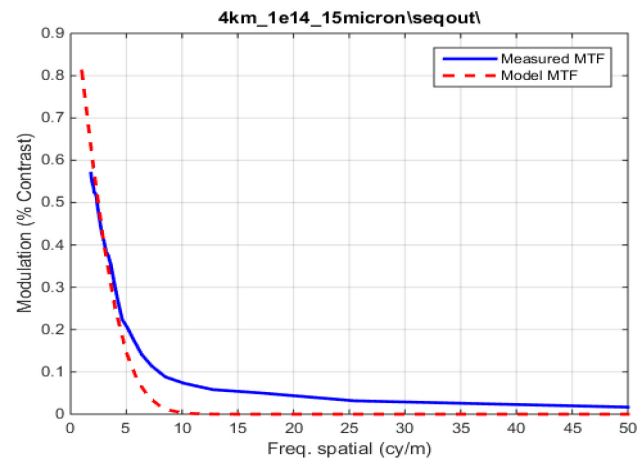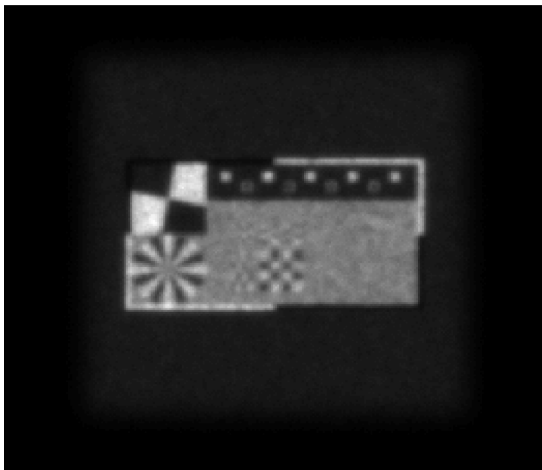
Figure 4-13: Result for 4 km.
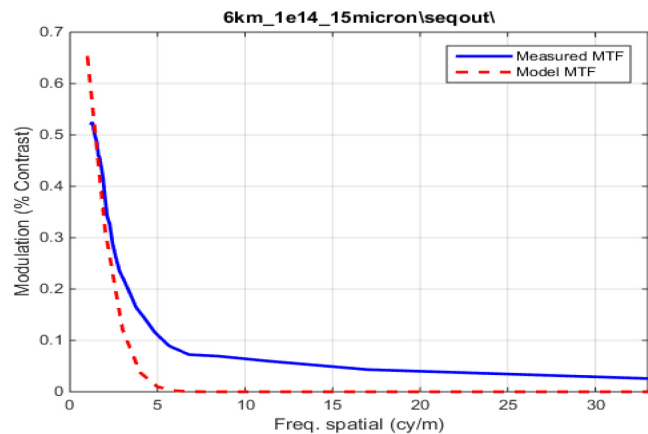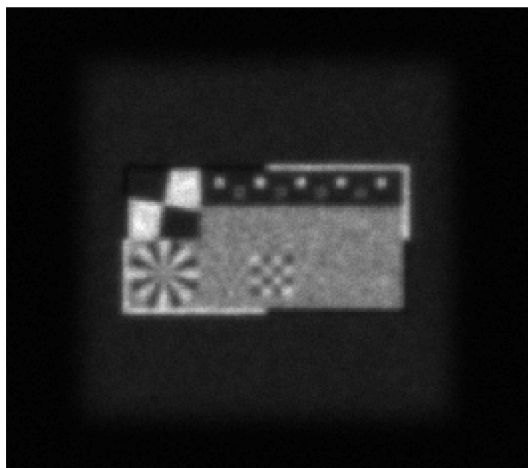
Figure 4-14: Result for 6 km.

We can observe that for the low frequencies, theoretical and measured system's MTF are in good accordance. For high frequencies, the accordance decreases: this is mainly caused by the residual noise in the averaged image.

Such analysis can be used for a first estimation of image processing gain over range performance:

- First, compare the global system MTF without and with the image processing; and

- Then, use the global system MTF curve obtained with the image processing in an analytic model for range performance prediction.

DGA also illustrates the rendering effect of the elevation of the sensor on the image quality. Indeed, the IMOTEP tool takes into account different C_n^2 profiles (Hufnagel Valley, Tatarskii, and custom). As the propagation tends to be a slant path, the effect of the turbulence is decreasing.

The following plots (Figure 4-15 – Figure 4-18) illustrate the image quality of the DRDC target seen by the active sensor defined previously, for a distance of 2 km, a C_n^2 at 2 meters of $1 \cdot 10^{-13}$ m$^{-2/3}$ assuming a day Tatarskii vertical profile, a target altitude of 2 meters and 4 different altitudes for the sensor: 2, 10, 100,

and 1000 meters. Each figure shows a single frame without any averaging process. Also on the top right corner, an illustration of the instantaneous turbulent PSF is given (red circle is the diameter containing 63% of the PSF total energy).
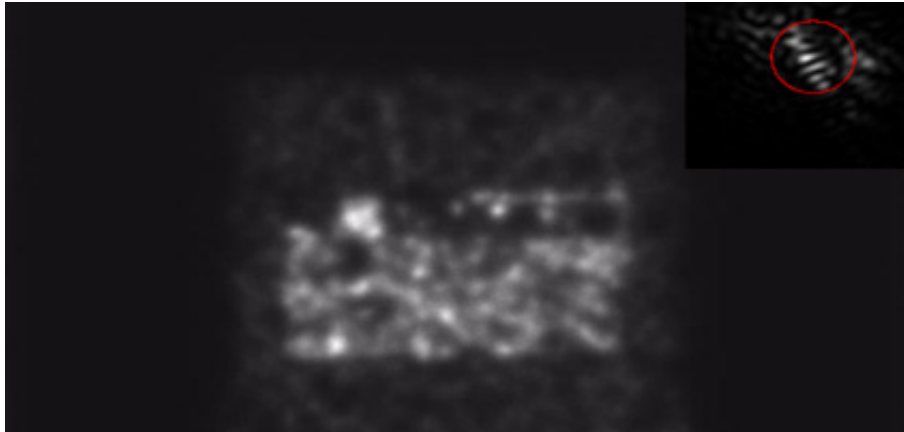
Figure 4-15: DRDC Target for a Horizontal Path (Sensor Altitude = 2 m).
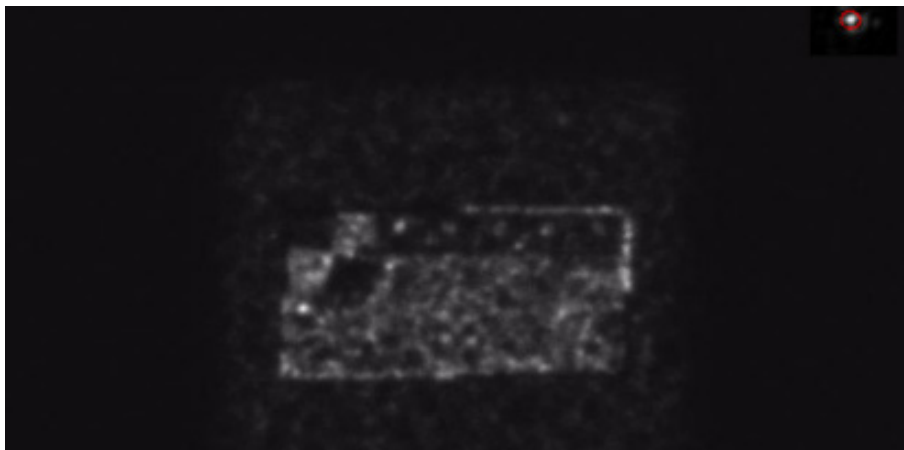
Figure 4-16: DRDC Target for a Slant Path (Sensor Altitude = 10 m).
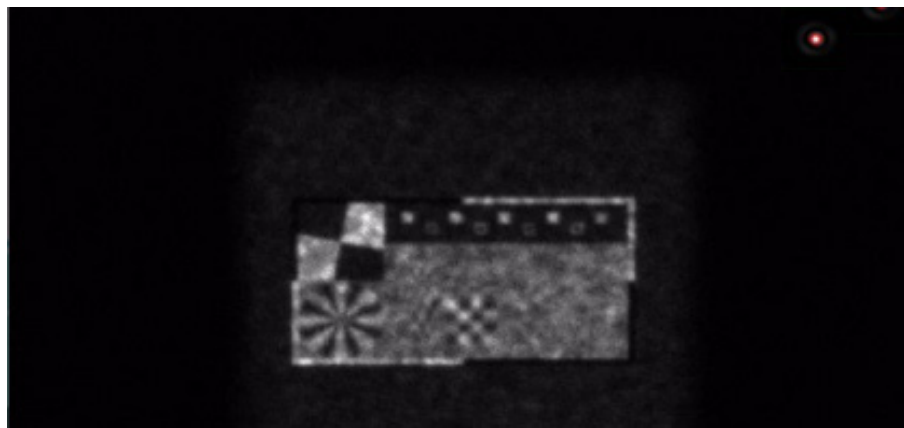
Figure 4-17: DRDC Target for a Slant Path (Sensor Altitude = 100 m).
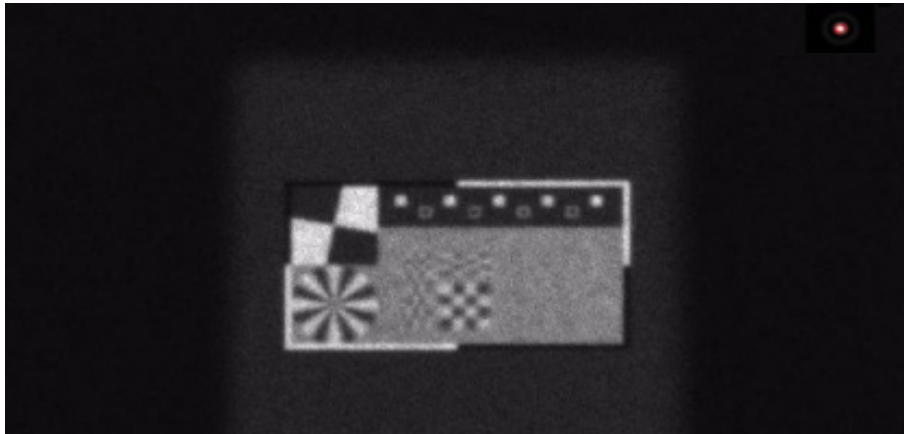
Figure 4-18: DRDC Target for a Slant Path (Sensor Altitude = 1 km).

Note that in the following section, for the CANADA and GERMANY results, the images are calculated without consideration of the sensor sensitivity and tube MTF.

Active imaging simulations on the DRDC target were performed using the DRDC OTISS-A model. The imaging and atmospheric parameters used in the model were determined by the SET-219 group. The parameters that were kept constant between simulations are listed in Table 4-2.

Table 4-2: Fixed Parameters for the DRDC Active Imaging Simulations.

IFOV	6.25 μrad
Imaging aperture diameter	24 cm
Frame rate	30 Hz
Wavelength	1.55 μm
Specular zone coherence length	39.5 μm
Source diameter	1 cm
Wind	1 m/s
Outer scale	2 m
Inner scale	1 cm

Note also that the source was aligned with the target's centre and that the width of the illuminating beam was assumed to be much larger than the width of the target. Note also that the weakly specular zone was set to be isotropic with a coherence length of 39.5 μm. Only the range (2, 4 and 6 km) and the C_n^2 (1e-15, 1e-14 and 1e-13) varied from one simulation to another.

Figure 4-19 shows a sample active image from the DRDC OTISS-A model of the DRDC target with no turbulence at a range of 2 km. The bumps in the specular zone in the lower right corner are visible due to the variable surface inclination and the weakly specular nature of the surface. Had that surface been Lambertian, they would not be visible at all.
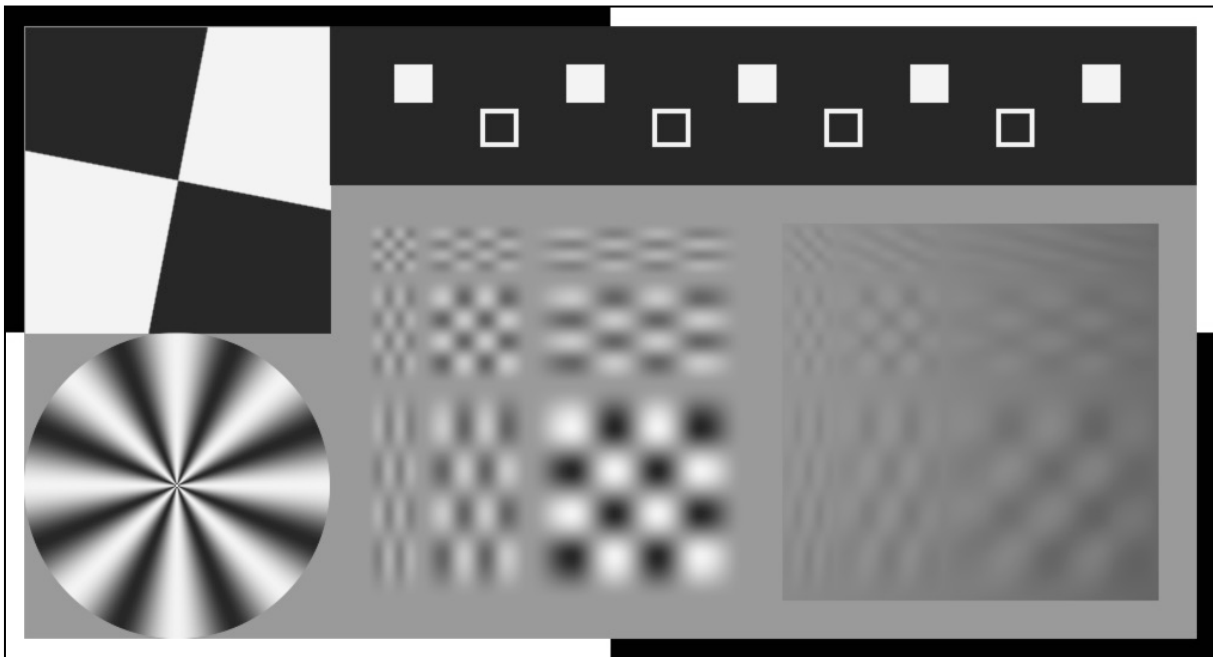
**Figure 4-19: Sample Active Image from the OTISS-A
Model Without Turbulence at a Range of 2 km.**

We see in Figure 4-20 sample active images with a C_n^2 = 1e-15, at a range of 2 km (with a corresponding Rytov parameter of 0.007), a range of 4 km (Rytov parameter of 0.025) and a range of 6 km (Rytov parameter of 0.054). Each case is well within the weak optical turbulence regime (Rytov parameter ≤ 0.3), which is where the OTISS-A is designed to perform. The 2 km image resembles Figure 4-19 but with a scintillating 'noise' superimposed on it. The specular zone becomes harder to perceive, partly because of the scintillation but also because incoming rays are now arriving from a range of angles due to the turbulence. The 4 and 6 km images show larger and stronger scintillation patches (caused by the cumulative effect of the longer propagation), as well as the disappearance of the specular zone. This most likely is due to the stronger scintillation and the more variable angle of arrival of the rays, but also because at those ranges the angles between the incoming and reflected rays are narrower, thus making weakly specular scattering look more Lambertian.
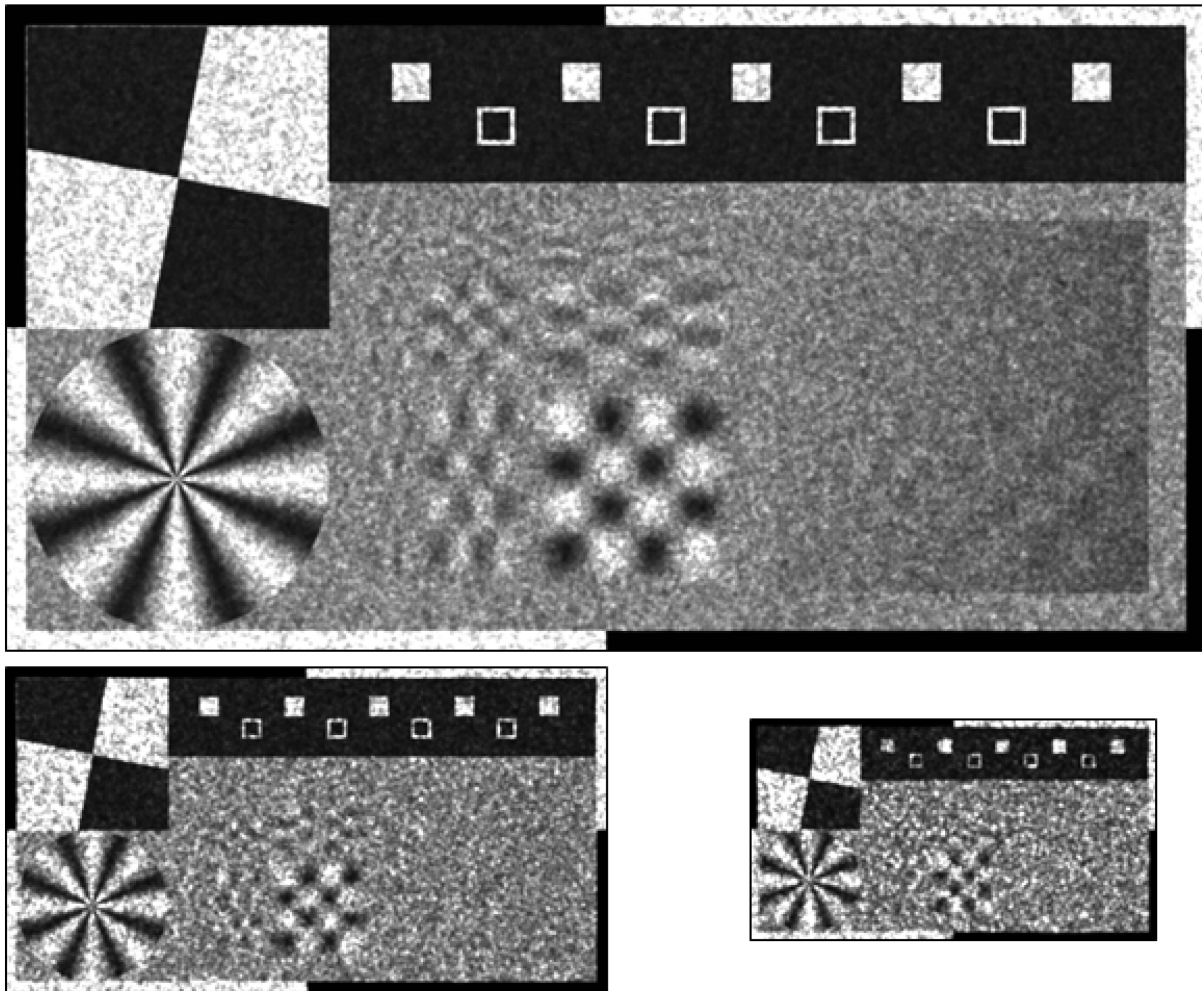
Figure 4-20: Sample Active Images from the OTISS-A Model with C_n^2 = 1e-15. The upper panel is at 2 km range, the lower left panel at 4 km range and the lower right panel at 6 km range.

We see the same tendency in Figure 4-21, where we have sample active images with C_n^2 = 1e-14 and at ranges of 2 km (Rytov parameter of 0.072), 4 km (Rytov parameter of 0.255) and 6 km (Rytov parameter of 0.536). Apart from the stronger scintillation and images displacement, the stronger turbulence makes the specular zone harder to perceive. This is even more apparent in Figure 4-22, where the specular zone disappears completely at a range of 2 km and C_n^2 of 1e-13 (Rytov parameter 0.715).
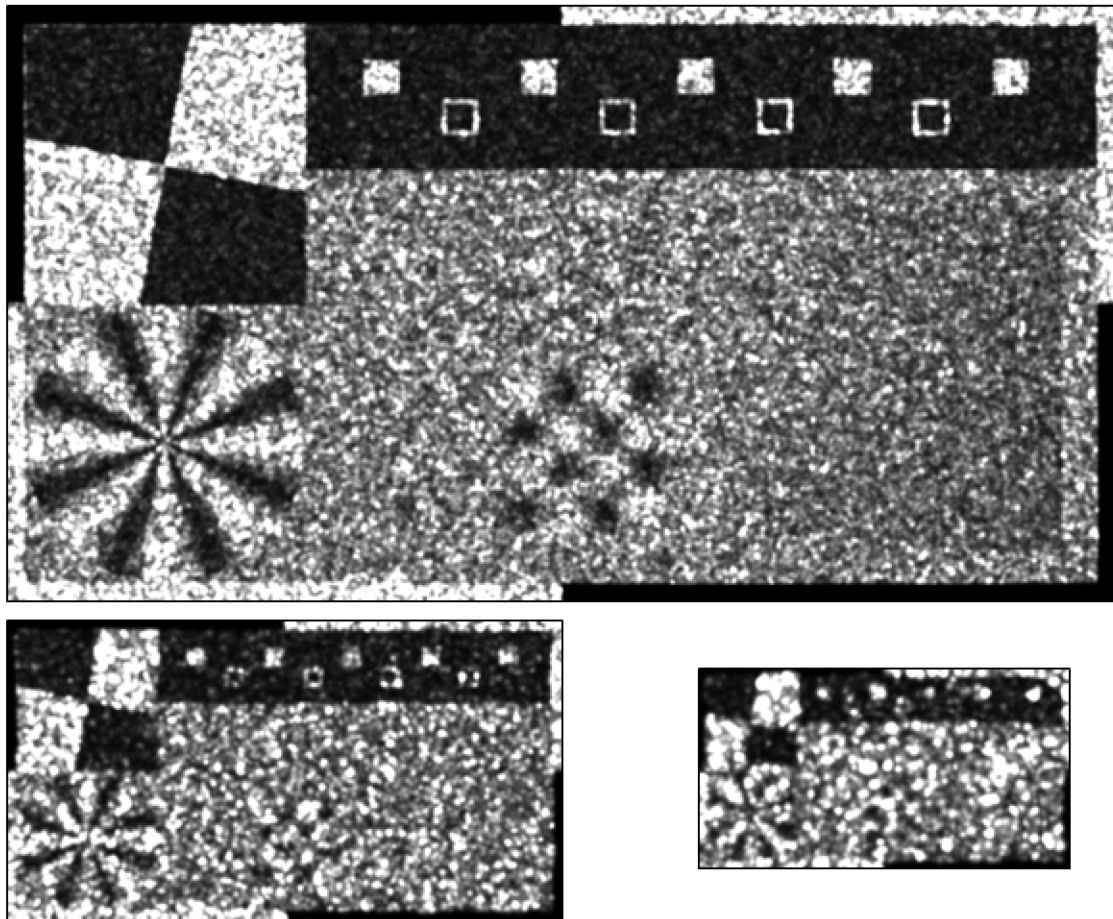
Figure 4-21: Sample Active Images from the OTISS-A Model with C_n^2 = 1e-14. The upper panel is at 2 km range, the lower left panel at 4 km range and the lower right panel at 6 km range.
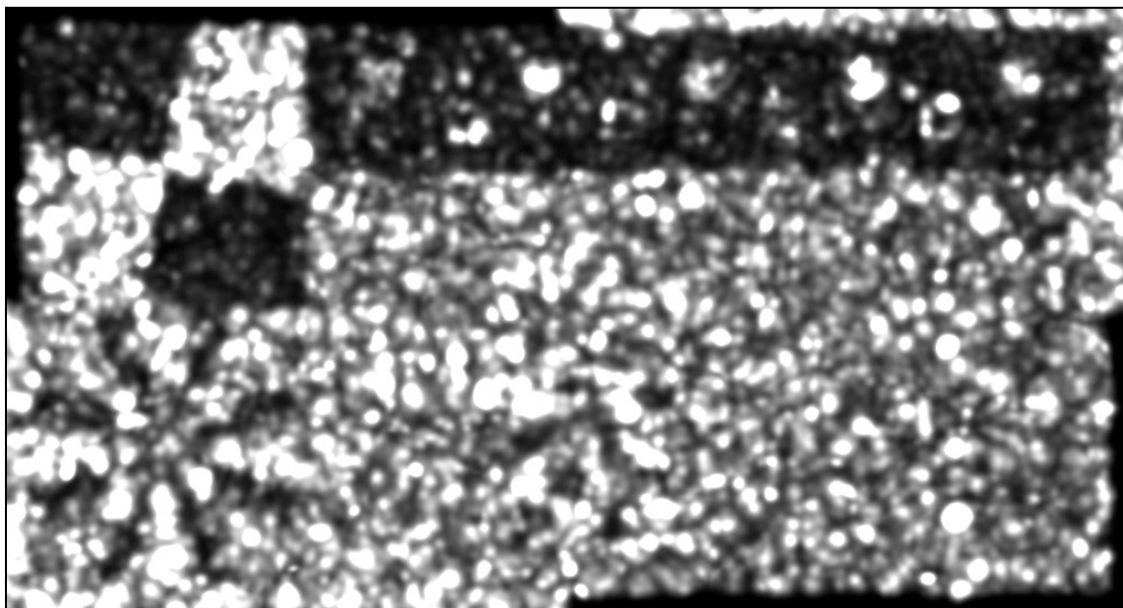
Figure 4-22: Sample Active Images from the OTISS-A Model with C_n^2 = 1e-13 at 2 km Range.

We close this analysis by mentioning that active imaging degrades more rapidly with turbulence than passive imaging, owing to the fact that turbulence affects propagation in both directions. This causes greater scintillation, image displacement and distortion than in the passive imaging case. Such effects, along with the fact that turbulence causes a greater variability in the angle of arrival of the incoming rays, make specular zones appear more Lambertian. It should be noted that some of the cases studied (C_n^2 = 1e-14 at 6 km and C_n^2 = 1e-13 at 2 km) are beyond the weak optical turbulence regime and are therefore outside the domain of validity of OTISS-A.

This section illustrates how the IOSB model for active imaging simulation works for flat scenery, where gated viewing does not give added value. The parameters of the simulation are similar to those listed in Table 4-2. For the DRDC target, only the moderate turbulence scenario ($C_n^2 = 10^{-14}$ m$^{-2/3}$) was used. In order to illustrate how an image in the detector plane is simulated in the framework of the IOSB model, the image formation process will be explained in case of the DRDC target in details.

The first step in simulating the image formation in the detector plane is the forward propagation by the FFT split step method of a divergent beam. The laser beam divergence was increased compared to the initially planned value of half the receiver horizontal divergence (mainly in order to have a broader illumination of the OKTAL scene). A sample propagation of such a beam at a range of 4 km for the moderate turbulence scenario is given in Figure 4-23.
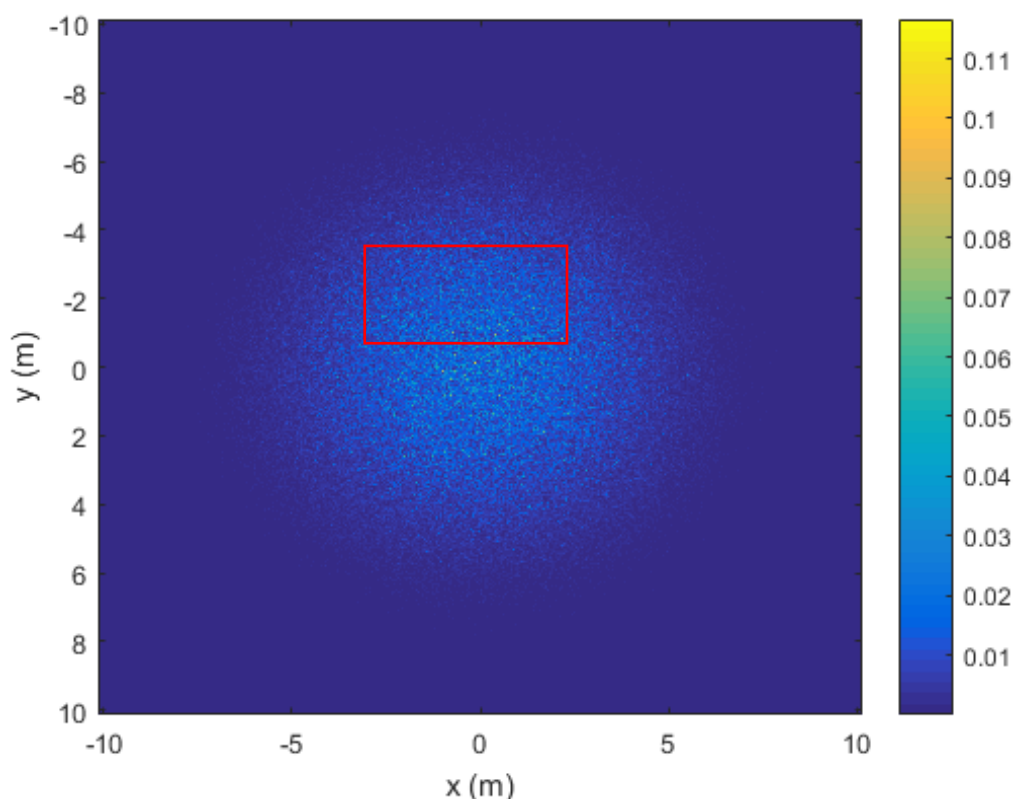
Figure 4-23: Sample Intensity Distribution in Target Plane at 4 km. The color bar is referring to intensity for a beam with unit power. The red rectangle represents the DRDC target extent in the target plane.

As a next step, the intensity distribution in the target plane just after reflection by the target is calculated. A sample reflected intensity distribution is presented in Figure 4-24. The part of the beam power that does not hit the DRDC target is supposed to be lost (or entirely absorbed by the background).
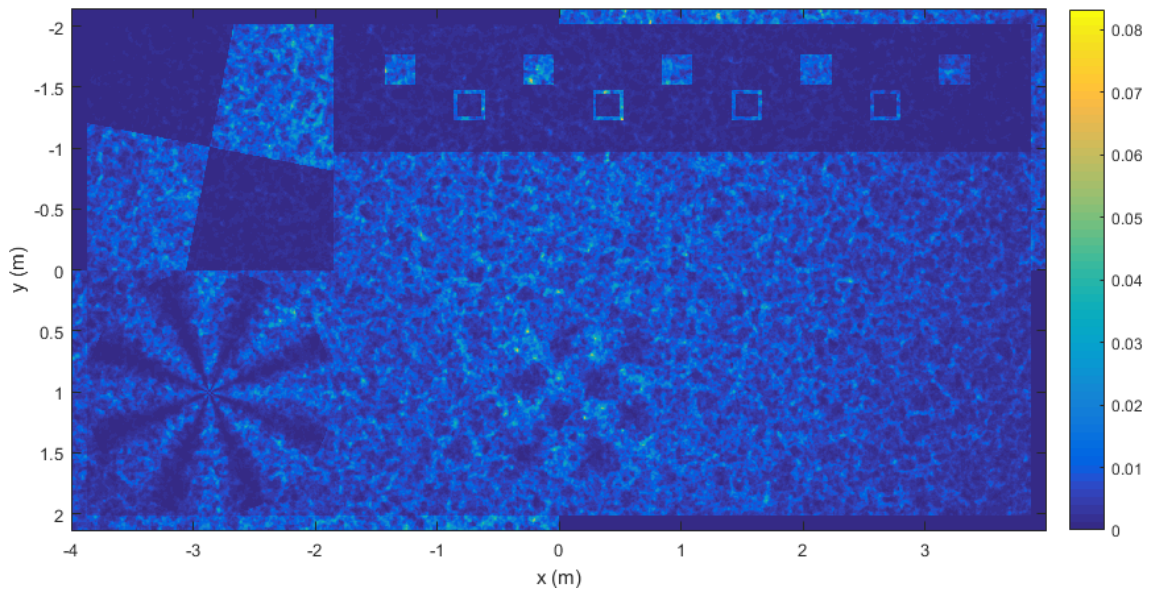
Figure 4-24: Sample Intensity Distribution in Target Plane Directly After Reflection at the DRDC Target. The color bar is referring to intensity for a beam with unit power.

Since the empirical turbulence simulator works with pristine images, that is, images that are formed in the detector plane without any turbulence degradations nor diffraction effects, the next step consists in perfectly imaging the target plane field of view in the detector plane. This is essentially a downsampling process. A sample resulting pristine image in the detector plane of the reflected intensity at the target is shown in Figure 4-25. Since intensity values were not calculated explicitly in the detector plane, this figure does not contain colour bar information of the absolute intensity values as was the case for the target plane related intensity distributions.
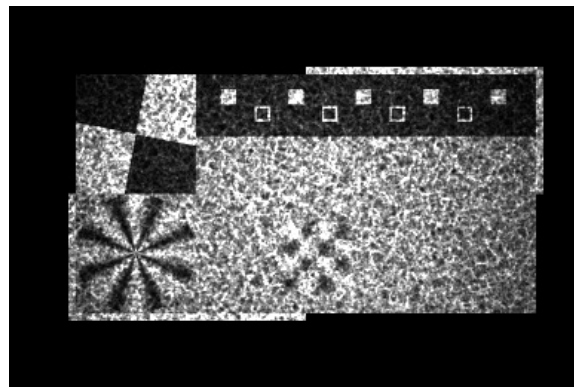
Figure 4-25: Pristine Sample Image in the Detector Plane of the Reflected Intensity at the DRDC Target Located at 4 km from the Sensor.

Eventually, for the whole set of frames to be simulated, the empirical turbulence simulator computes a spatially and temporally correlated noise (three dimensional correlated noise) and applies it on each frame. For each pixel, three random values are taken into consideration. Two of them relate to image dancing (one for each direction) while the other one refers to image blurring (assumed circularly symmetric). With this triplet of values for each pixel, a Gaussian kernel is applied on the image to simulate turbulence degradation and diffraction effect. Figure 4-26 shows a sample result of such a calculation. This is also the primary output of the present imaging simulation.
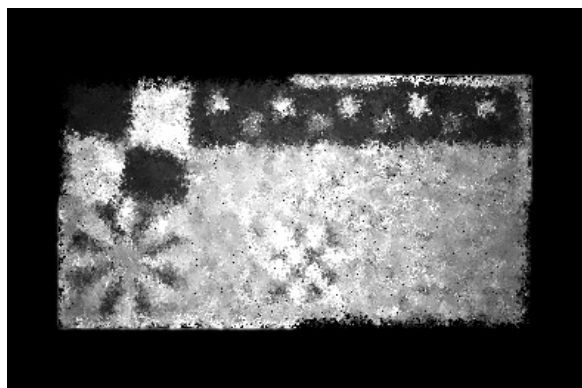
Figure 4-26: Detector Plane Sample Image of the Reflected Intensity at the DRDC Target After Distortions Due to Turbulence and Diffraction and for a Distance Target-Sensor of 4 km.

In case of the longer range of 6 km, the pristine image and the distorted one formed in the detector plane are given in Figure 4-27 and Figure 4-28, respectively.
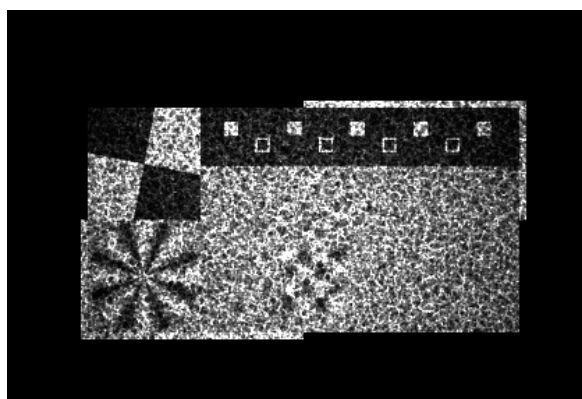
Figure 4-27: Pristine Sample Image in the Detector Plane of the Reflected Intensity at the DRDC Target Located at 6 km from the Sensor.
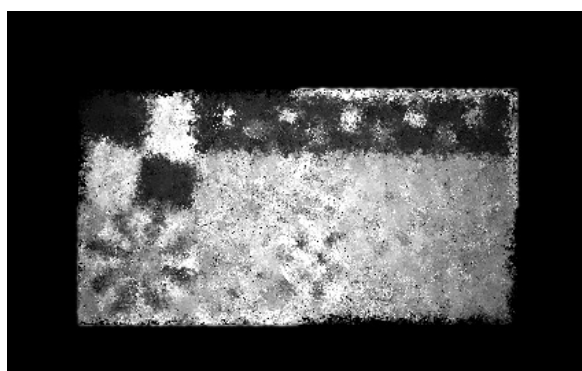
Figure 4-28: Detector Plane Sample Image of the Reflected Intensity at the DRDC Target After Distortions Due to Turbulence and Diffraction and for a Distance Target-Sensor of 6 km.

The DRDC target was used in the 2D and 3D active imaging system simulations. 2D simulations refers to range data per pixel (single-frame or averaged-frame Geiger-mode data), while 3D simulations refers

to both range and intensity per pixel (single frame and cumulative linear-mode data). In these simulations, the scene was set up so that the target was 1 m by 1.8 m, positioned 150 m away from the sensor, which had a FOV of 31.2 arcmin. In this setup, the target occupies one half of the horizontal FOV. Table 4-3 shows the active system specifications for the 2D and 3D simulations.

Table 4-3: System Specifications for 2D and 3D Simulations.

Sensor (128 x 128)	
Pixel Size	20 μm
FOV (iFOV)	0.52° or 31.2 arcmin (0.004° or 14.4 arcsec)
Receiver Bandpass	0.5 nm centered at 1064 nm
Gate Resolution	10 GHz
Laser Source (1064 nm)	
Line Width	0.3 nm
Energy Per Pulse	10 mJ
Pulse Width	0.1 ns
Divergence	0.018 rad (half angle)
Beam Profile	Super Gaussian (radial, 10th order)

Figure 4-29 shows the 2D simulation results for the zero Dark Count Rate (DCR) case and the 100 Hz DCR case. Although the images shown are only range information, there is a slight range bias present due to the relative widths of the laser pulse (0.1 ns) and the timing gate (1 ns), allowing the photons at the front of the laser pulse to reflect back to the sensor with higher probability in brighter areas than in darker areas. This effect disappears when the gate width is much longer than the laser pulse width. The images shown are cropped to show only the target and not the entire FOV.
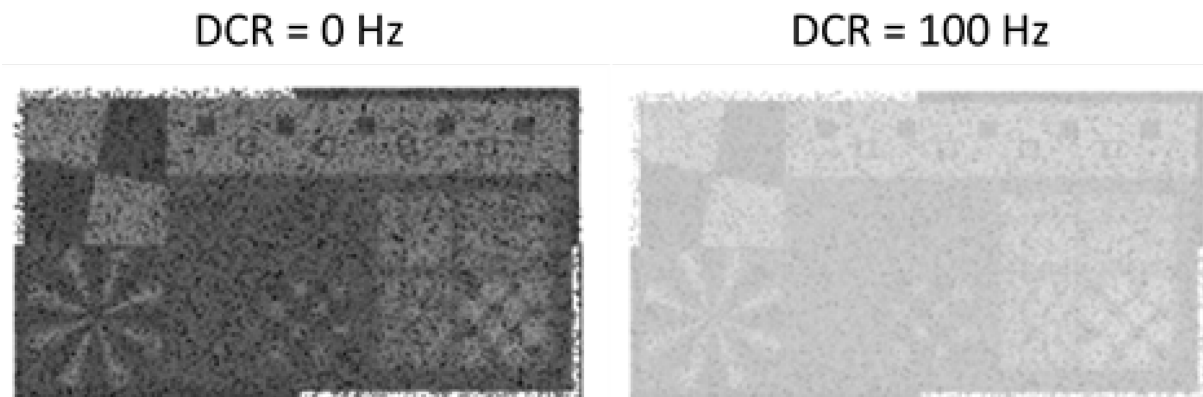
Figure 4-29: Range Value Results (Geiger Mode Simulated System) with Dark Count Rates (DCR) of 0 Hz (Left) and 100 Hz (Right). Noise shown in the 0 Hz case is Poisson noise of the illuminating laser light. Differences in range for varying reflectance on the target are due to range bias and the sampling rate as compared to the pulse duration.

Figure 4-30 shows the 3D simulation results, included a case with no timing error (jitter) and a case with 0.1 ns of timing error (jitter) rms. The intensity image shown is a total of all photons received in each pixel,

while the range images show the average arrival time recorded in each pixel. These images are cropped to show only the target and not the entire FOV.
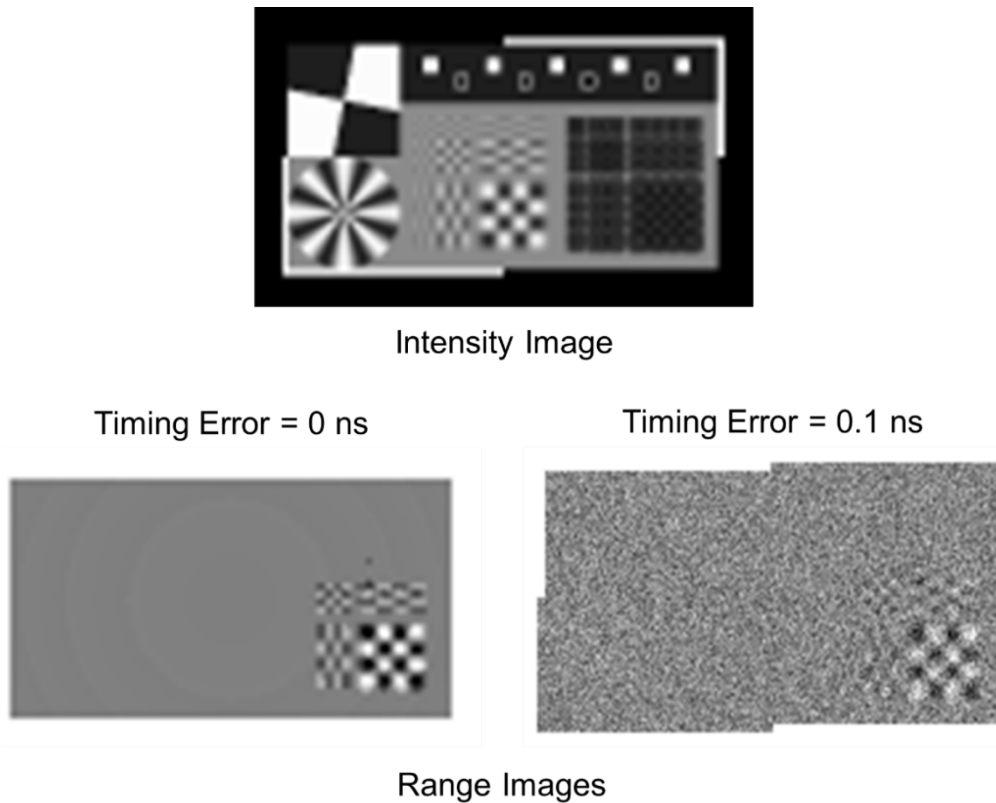
Figure 4-30: Intensity (Top) and Range (Bottom) Results for a Linear-Mode System; Range Images Show Results for No Jitter (Left) and a Jitter or Timing Error of 0.1 ns (Right).

4.4 FULL SYNTHETIC SCENE SIMULATION

One of the aims of the synthetic scene simulation is to illustrate gating imaging capability. Recall that the gate shape seen by the sensor is the convolution of the laser temporal profile with the time integration temporal profile. In order to isolate the target from the background, the gate must be short enough, and also have a strong slope edge.

The gate is constructed as follows:

- Laser pulse: width of 15 ns, with a Gaussian temporal shape; and
- Sensor time integration: width of 100 ns, with a uniform response temporal shape.

Three different gate's lengths have been used:

- Short gate on the target;
- Short gate on the background; and
- Long gate on the target and the background.

The active sensor configuration is based on the parameters defined in Table 4-1, but with the following modifications:

- No sensor noise;

- No sensor MTF; and

- No optical aberration.

Figure 4-31 and Figure 4-32 give the sensor image for the three gates, for a single frame and also for an averaged image over 10 frames.

- $Z = 4$ km
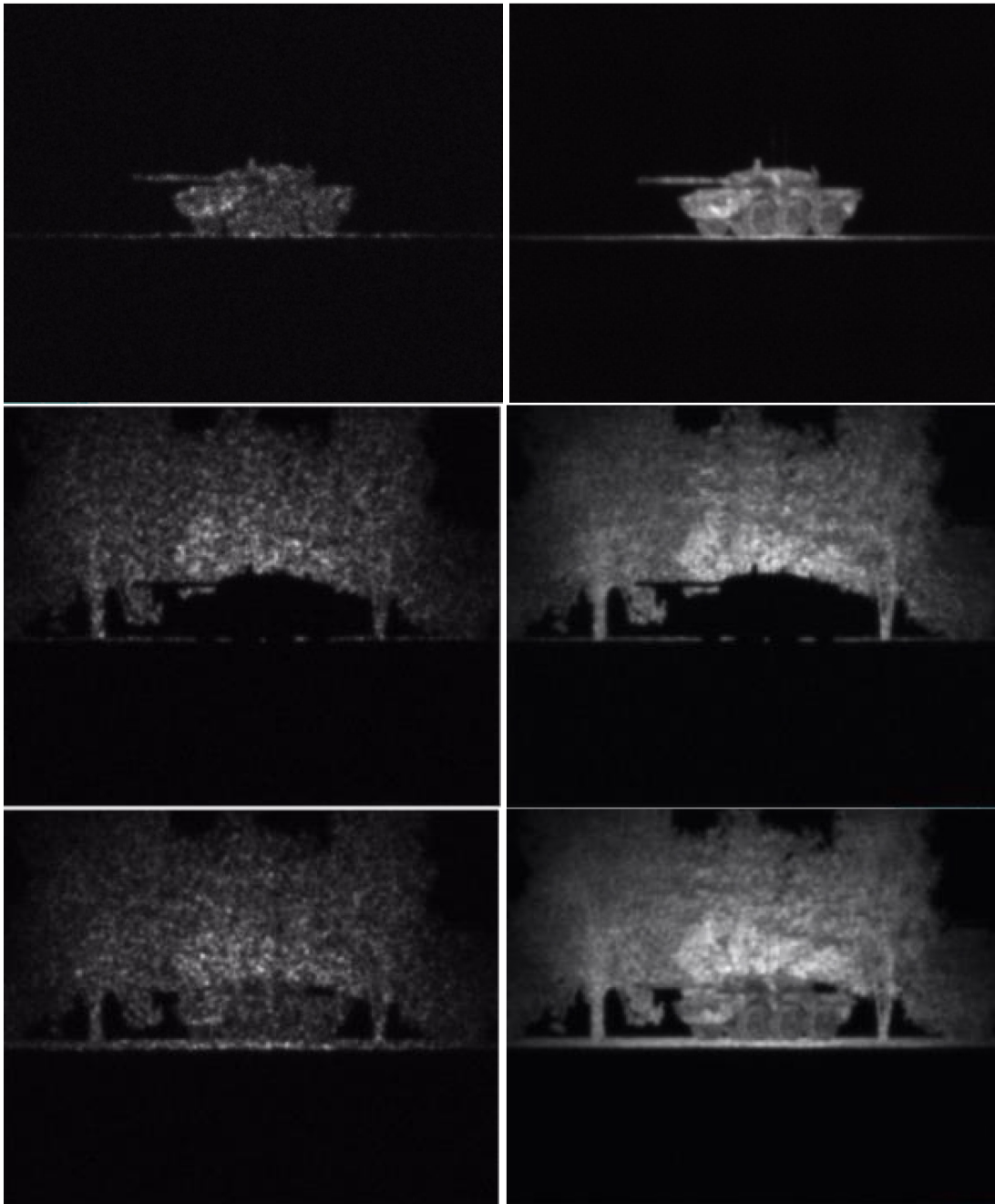
Figure 4-31: DGA Result at 4 km – Single Frame (Left) and 10 Frames Averaged (Right). First line = short gate on the target. Second line = short gate on the background. Third line = long gate).

- $Z = 6$ km
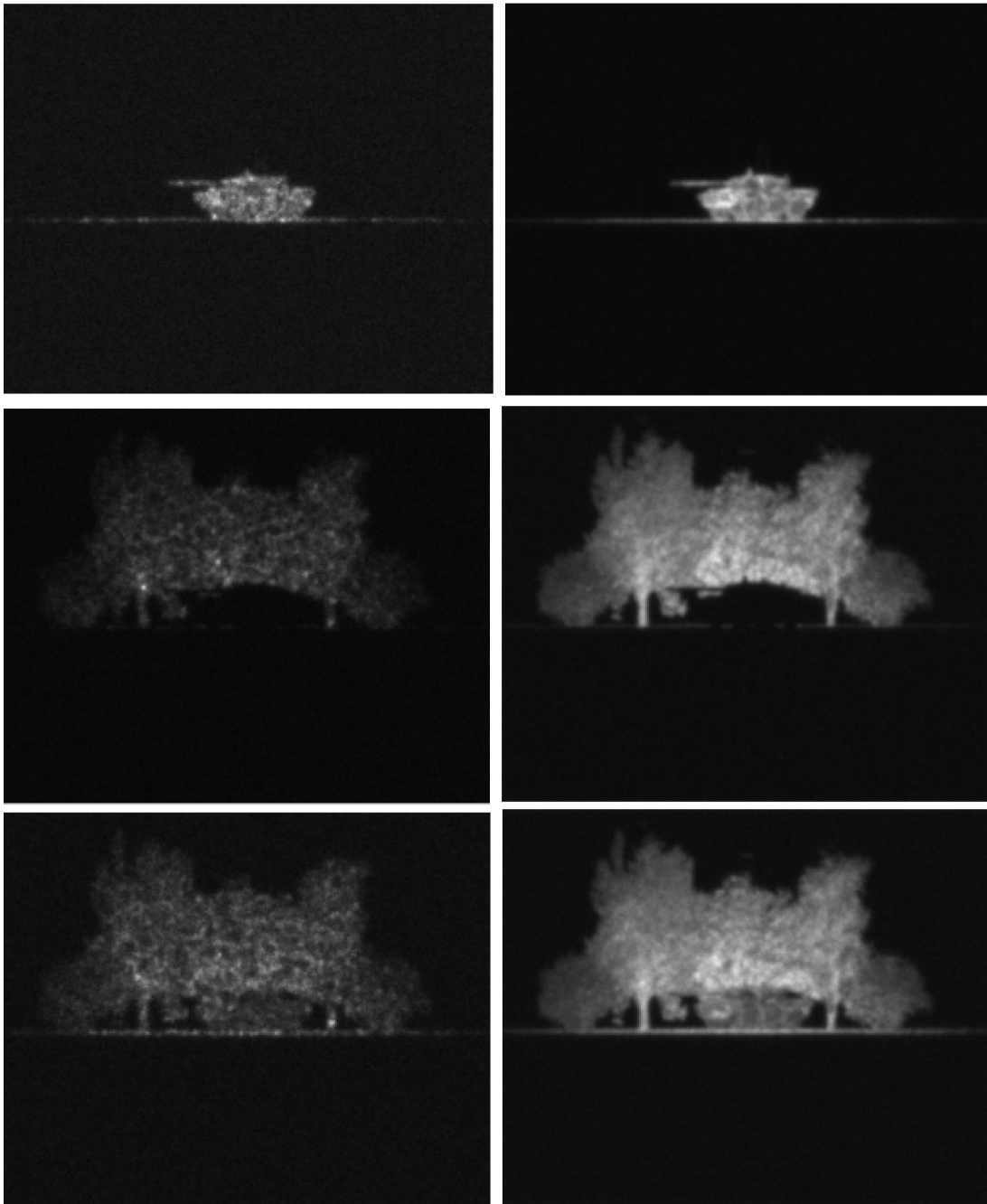
Figure 4-32: DGA Result at 6 km – Single Frame (Left) and 10 Frames Averaged (Right). First line = short gate on the target. Second line = short gate on the background. Third line = long gate).

Although no quantitative evaluation of the image has been performed, we can compare the outputs of the modeling chain to some field results. Figure 4-33 and Figure 4-34 compare the simulation output with some DGA field results using the laser range gating effect. Qualitatively, the simulation compares very well with experimental field data.
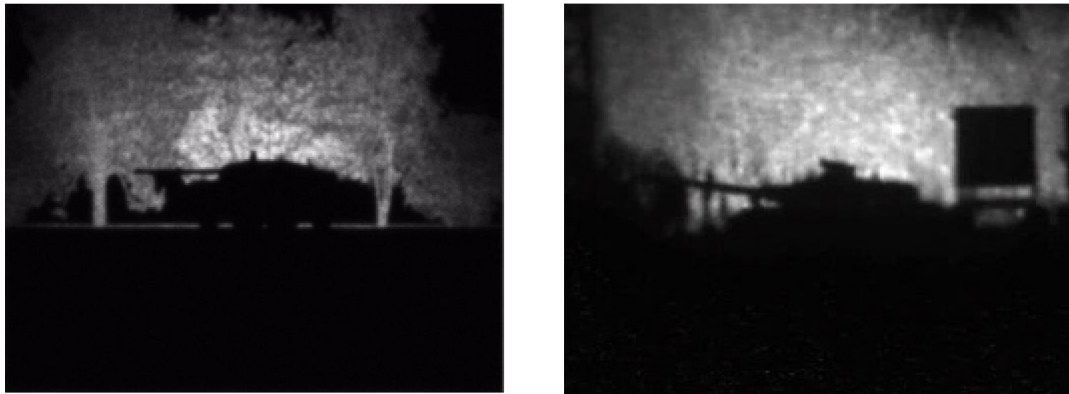
**Figure 4-33: Field and Simulation Comparison for the « Silhouette »
Gate – Simulation (Left) and Field Result (Right).**
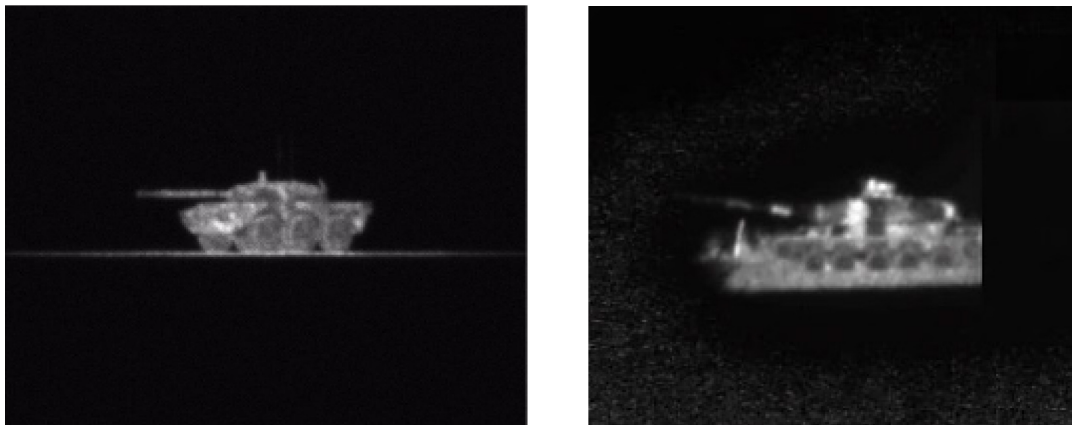
**Figure 4-34: Field and Simulation Comparison for the Short Gate
Around Target – Simulation (Left) and Field Result (Right)**

Active imaging simulations on the synthetic scene provided by the DGA (see previous section) were performed using the DRDC OTISS-A model. The parameters used were the same as those listed in Table 4-2, except that the target was assumed to be entirely Lambertian. Also, the collimation of the illuminating beam was adjusted so that the Gaussian beam width would be half the horizontal Field-Of-View (FOV) at 4 km. The C_n^2 was kept constant at 1e-14, while only the range would alternate between 4 and 6 km. Sample images of these simulations are shown in Figure 4-35.
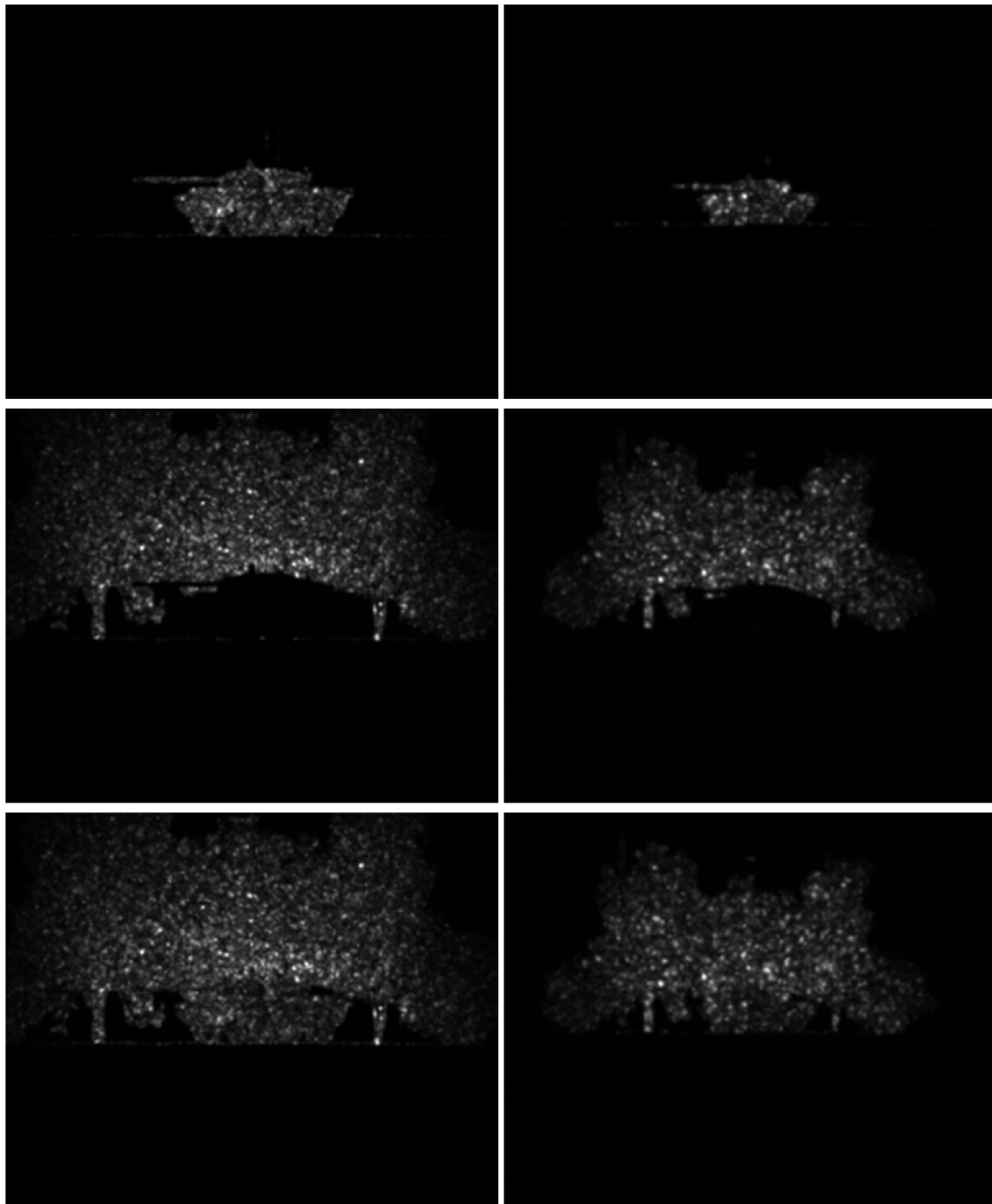
Figure 4-35: Sample Active Images from the OTISS-A Model with C_n^2 = 1e-14. The top row shows the short gate on the target, the middle row shows the short gate on the background and the bottom row shows the long gate on both. The column on the left shows the target and background at a range of 4 km while the one on the right shows a range of 6 km.

A visual comparison of the single frames at 4 km in Figure 4-35 with the single frames from the DGA IMOTEP model (left column in Figure 4-31) shows that the models compare reasonably well at that range. However, a comparison between the single frames at 6 km in Figure 4-35 with the single frames from the left column in Figure 4-32 reveals that OTISS-A produces wider scintillation fluctuations than IMOTEP. While an in depth analysis of the two models is needed, we might suggest that one possible cause for the discrepancy could be that OTISS-A is designed for weak turbulence. At 4 km the Rytov parameter is 0.255,

close to the limit for weak turbulence, whereas at 6 km the Rytov parameter is 0.536. This value exceeds the weak turbulence limit and signals the onset of saturation, something OTISS-A was not designed to model.

The full synthetic scene simulation computed by the OKTAL workbench features reflecting scene elements located at different ranges from the sensor. This is in contrast to the DRDC target that was assumed to be flat. For the OKTAL target, only the moderate turbulence scenario ($C_n^2 = 10^{-14}$ m$^{-2/3}$) was worked out.

In order to show the added value of using gated viewing, simulation was carried out to selectively illuminate part of the scene. The OKTAL target simulation departs from the DRDC one in that scene elements reflectance is weighted using the temporal shape of the laser pulse and the time at which the laser pulse reaches these scene elements according to their sensor range. The reflectance of scene elements that are far away from the gate centre are taken to be zero, which is effectively the same as assuming that the radiation hitting these elements is completely absorbed.

Additionally, the empirical turbulence simulator expects every pixel to be mapped with the distance from which the impinging radiation is stemming. Consequently a range map must be computed from the finely resolved distance map of the original scene. This is a simple downsampling process of the scene size to the detector size. In this way each pixel is mapped with the effective scene range over its instantaneous field of view. Notice that in order to comply with constraints on the empirical turbulence simulator, range values that correspond to a reflectance below a certain threshold is set to 0.

In order to illustrate the gating process, the scene reflectance is shown together with its corresponding range map for a gate "behind the target" in Figure 4-36. This gate registers only backward reflected radiation from scene elements behind the target. Scene elements that are not inside the gate are attributed a zero range.
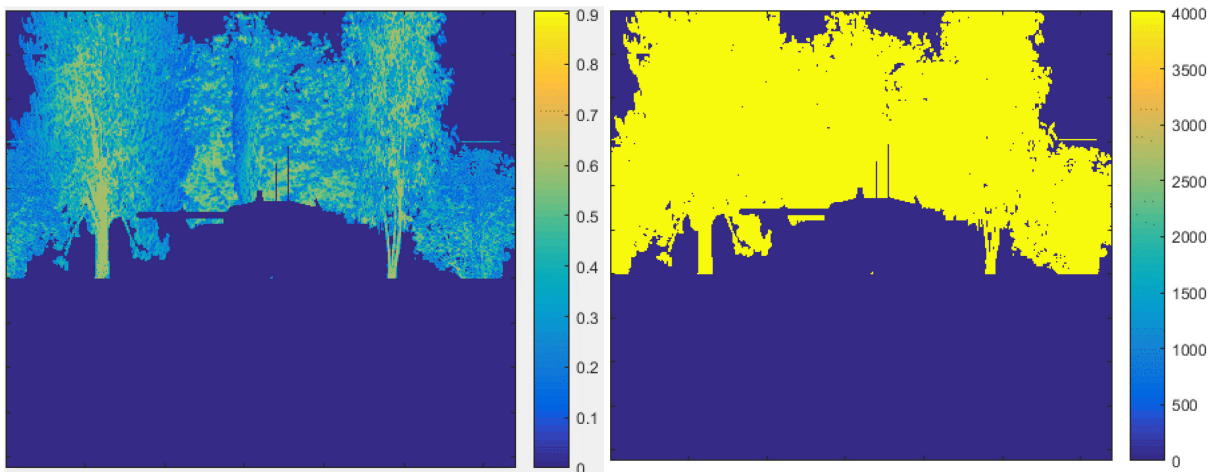
**Figure 4-36: Reflectance (Left) and Range (Right) Map for the
Scene Illuminated with a Short Gate Behind the Target.**

Apart from this gating feature for the simulation on the OKTAL target, there is no fundamental differences in the way the imaging simulation is carried out compared to the DRDC target image simulation.

Three different gates with different pulse width and gate centre pairs were simulated in the moderate turbulence scenario. These are:

- A long gate centred 10 meters behind the target with a laser pulse width of 50 nanoseconds, including target and background elements behind the target (hereafter called "long gate").

- A short gate centred on the target with a laser pulse width of 15 nanoseconds (hereafter called "short gate on the target").

- A short gate centred 20 meters behind the target with a laser pulse width of 15 nanoseconds. This prevents detecting reflection from the target and aims at imaging its silhouette (hereafter called "short gate behind the target").

For a target distance of 4 kilometres, sample pairs of images in the detector plane showing both pristine and distorted images are presented in Figure 4-37 – Figure 4-39, respectively. For a target distance of 6 kilometres, sample pairs of images in the detector plane showing both pristine and distorted images are presented in Figure 4-40 – Figure 4-42, respectively.
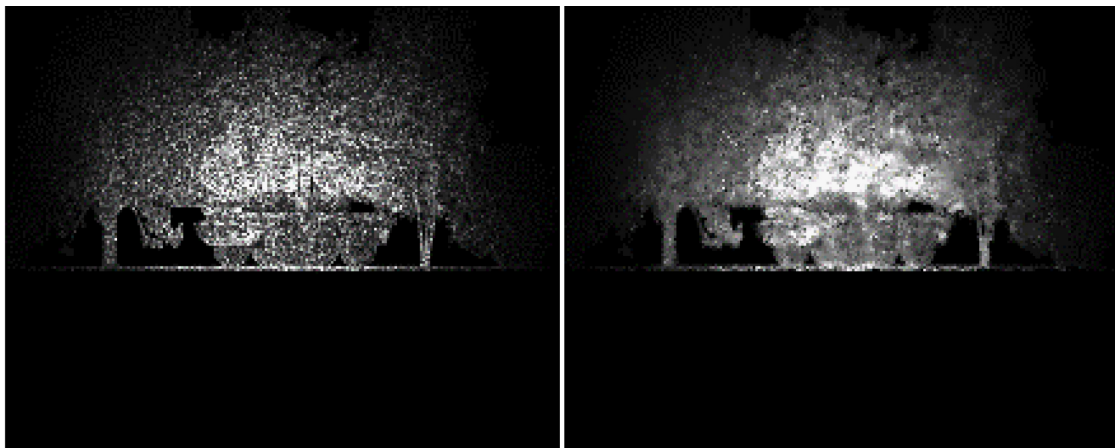
Figure 4-37: Sample Pristine (Left) and Distorted (Right) Images in the Detector Plane of the Reflected Intensity Distribution at the Target for a Target Distance of 4 km and a Long Gate.
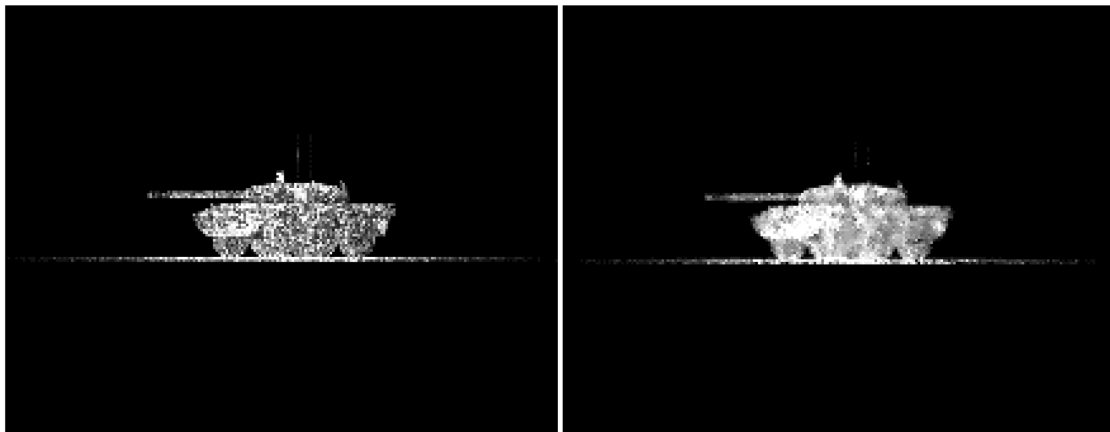
Figure 4-38: Sample Pristine (Left) and Distorted (Right) Images in the Detector Plane of the Reflected Intensity Distribution at the Target for a Target Distance of 4 km and a Short Gate on the Target.
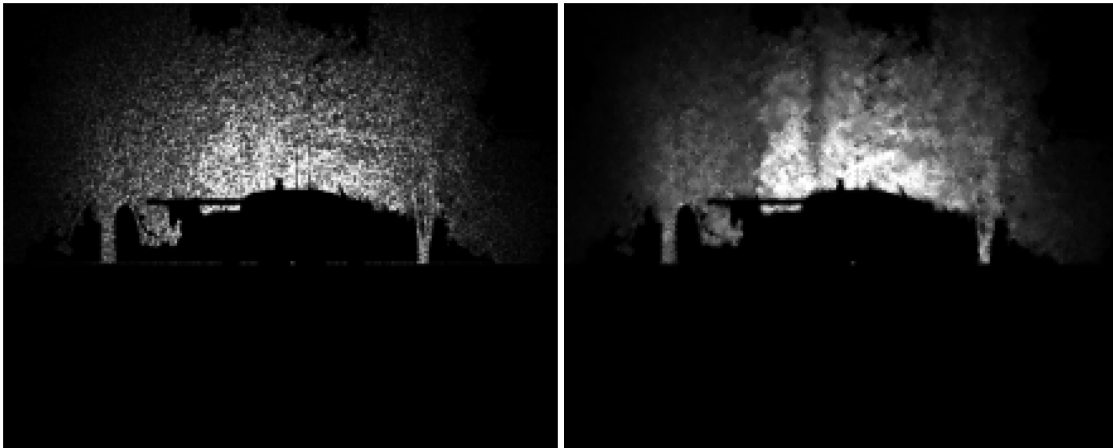
Figure 4-39: Sample Pristine (Left) and Distorted (Right) Images in the Detector Plane of the Reflected Intensity Distribution at the Target for a Target Distance of 4 km and a Short Gate Behind the Target.
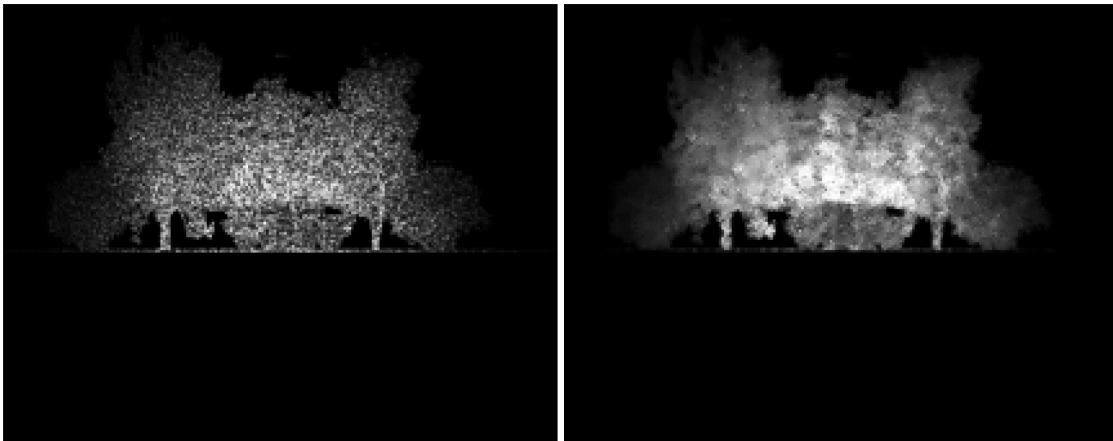
Figure 4-40: Sample Pristine (Left) and Distorted (Right) Images in the Detector Plane of the Reflected Intensity Distribution at the Target for a Target Distance of 6 km and a Long Gate.
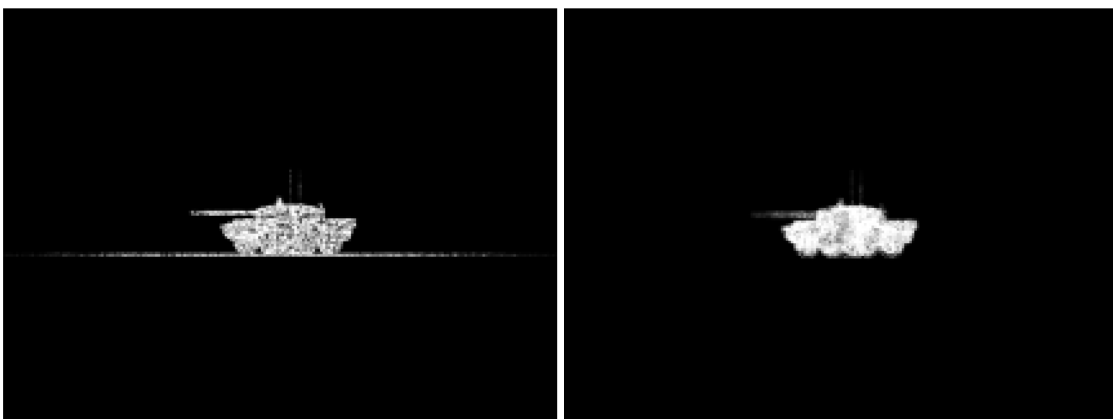
Figure 4-41: Sample Pristine (Left) and Distorted (Right) Images in the Detector Plane of the Reflected Intensity Distribution at the Target for a Target Distance of 6 km and a Short Gate on the Target.
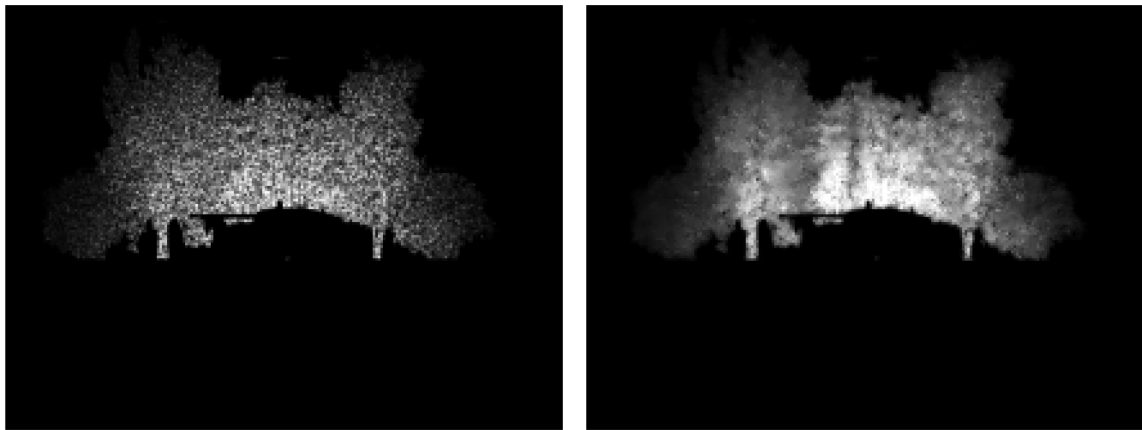
**Figure 4-42: Sample Pristine (Left) and Distorted (Right) Images in the
Detector Plane of the Reflected Intensity Distribution at the Target
for a Target Distance of 6 km and a Short Gate Behind the Target.**

4.5 UNDERWATER IMAGING RECONSTRUCTION

4.5.1 Beam Propagation Model Results

Snapshots of a Gaussian laser beam propagated physically and numerically through SiTTE are shown in Figure 4-43.
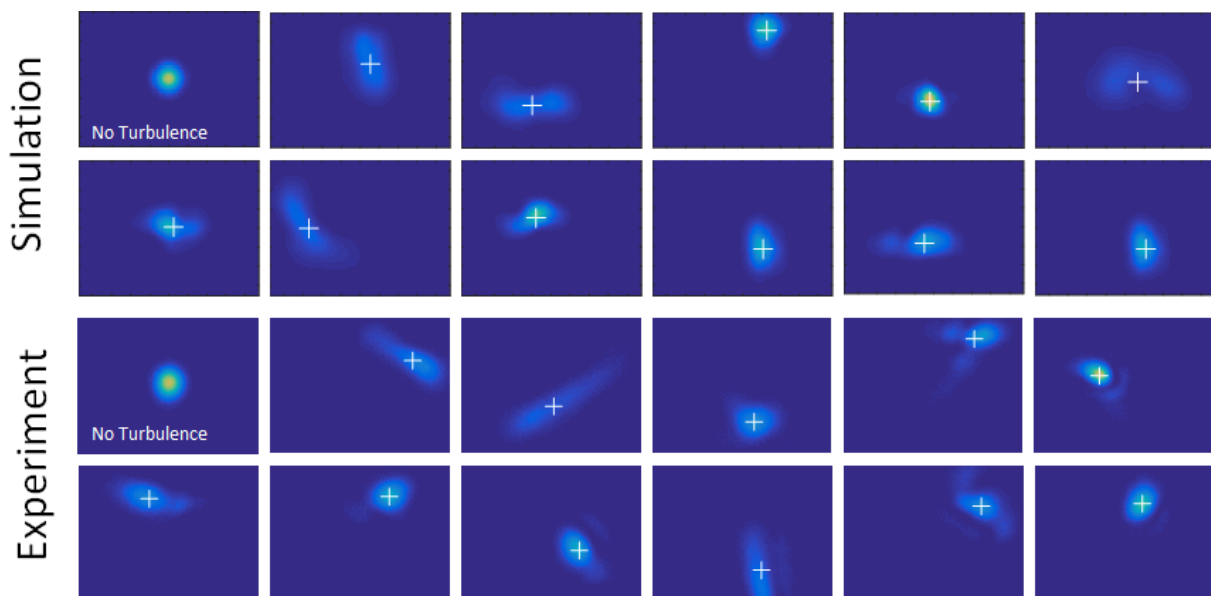
**Figure 4-43: Series of Experimental and Simulated Intensity Profiles of a Focused Gaussian
Beam After Propagating Through the Rayleigh–Bénard Convection Tank with Temperature
Difference ΔT = 16°C for the Simulated Data and ΔT = 17.1°C During the Experiment. The first
frame in each series is the undisturbed beam traversing the tank with no turbulence present.**

From the beam wander, i.e. the standard deviation of the beam centroid position after traversing SiTTE, C_n^2 is extracted. A turbulence outer scale of 50 cm is assumed for the calculation. The results are compared to C_n^2 calculated directly from the structure function from the simulated temperature field in Figure 4-44.
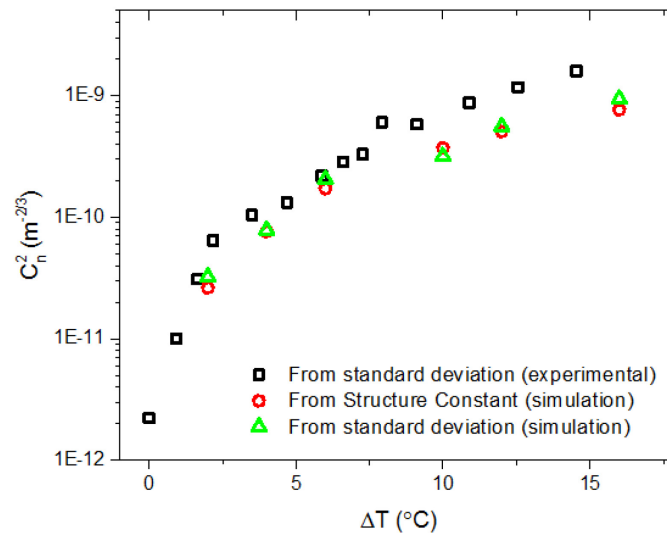
Figure 4-44: Comparison of the Index of Refraction Structure Function (C_n^2) as Extracted from the Physical and Simulated Rayleigh–Bénard Tank for Different Temperature Differences Between Top and Bottom Plate. The index of refraction structure function is extracted directly from the simulated temperature field via the structure function and from the simulated and experimental beam wander standard deviation.

Good qualitative and quantitative agreement between experimental and simulation is found, demonstrating the usefulness of SiTTE for the development and evaluation of electro-optical systems.

4.5.2   Application to Underwater Compressive Line Sensing (CLS)

A CLS system has been implemented [34] to test in a controlled optical turbulence environment. We will briefly outline the theoretical foundations here, followed by the optical and electronic design of a DMD-based CLS system, before the experimental results.

Imaging through turbulence imposes a different challenge than in a scattering environment [31], [35]. The point spread function in the turbulence environment, in general, is a spatial and temporal variant function. The CLS framework offers some unique features that are worth exploring. First of all, in CLS system, the measurement is obtained via spatial encoding of the target and the medium interferences mainly are along the path from the illuminator to the target. By adopting the multi-scaled sensing pattern design, the energy is condensed into a small number of beamlets, which therefore enables improve energy concentration than area flash system. Finally, the CLS imaging system adopts a First-In-First-Out (FIFO) scheme to store L solutions of each line, (L: the number of lines that are solved jointly), therefore, choosing the optimum from the L solutions is essentially a type of "lucky imaging". We conducted a series of experiments as an initial evaluation of the CLS system in the turbulence environment.

4.5.2.1   DMD-Based CLS Prototype System

Digital Micromirror Device (DMD) is a Micro-Electro-Mechanical (MEMS) device. A DMD consists of millions of electrostatically actuated micromirrors (or pixels) that can be individually controlled to reflect external light source. Figure 4-45(a) shows the light reflection path when the pixels are at ON and OFF states. When a pixel is at ON state, it tilts toward the light source and light is reflected to the projection lens. A bright pixel will show up in the projected image. When a pixel is at OFF state, it tilts away from the light source, and the light is directed to the light absorber. A dark pixel will appear on the projected image. During normal operation, the entire DMD surface is under constant illumination. When a binary pattern is loaded to a DMD, only those pixels that are at ON state direct light to the target.

(a)   (b)
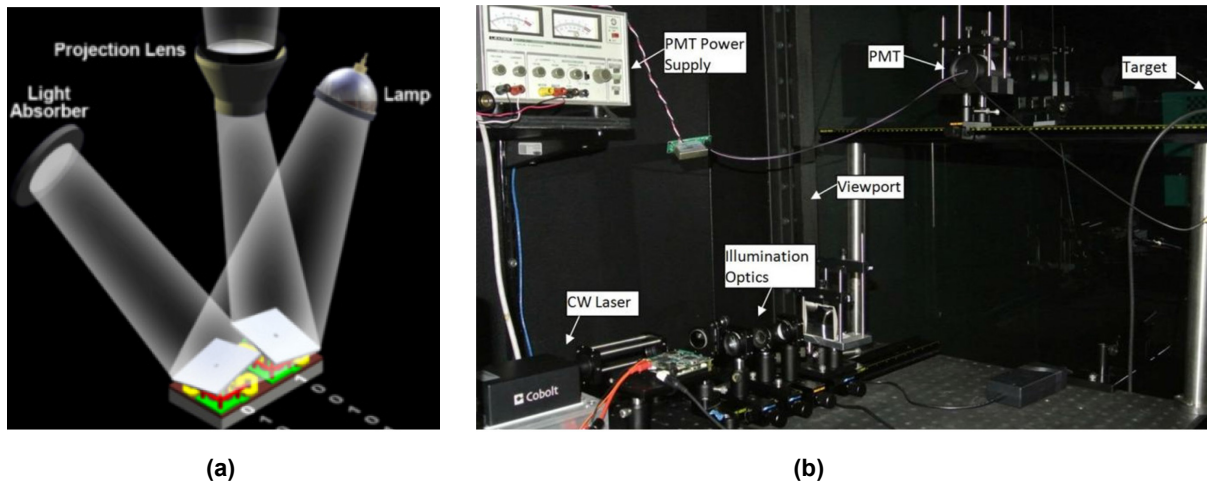
**Figure 4-45: (a) Illustration of a DMD in Binary SLM Operation with Micromirrors
in ON and OFF States; (b) Initial CLS Optical Bench Prototype [34].**

CLS optical bench prototype is shown in Figure 4-45(b). While the system was adequate in the original concept validation effort, the system configuration is cumbersome to be truly considered a "system"; the optical design is not robust and induces undesirable artifacts. In the current effort, a compact and robust system was developed. Figure 4-46 illustrates the new system implemented at NRL.

(a)   (b)
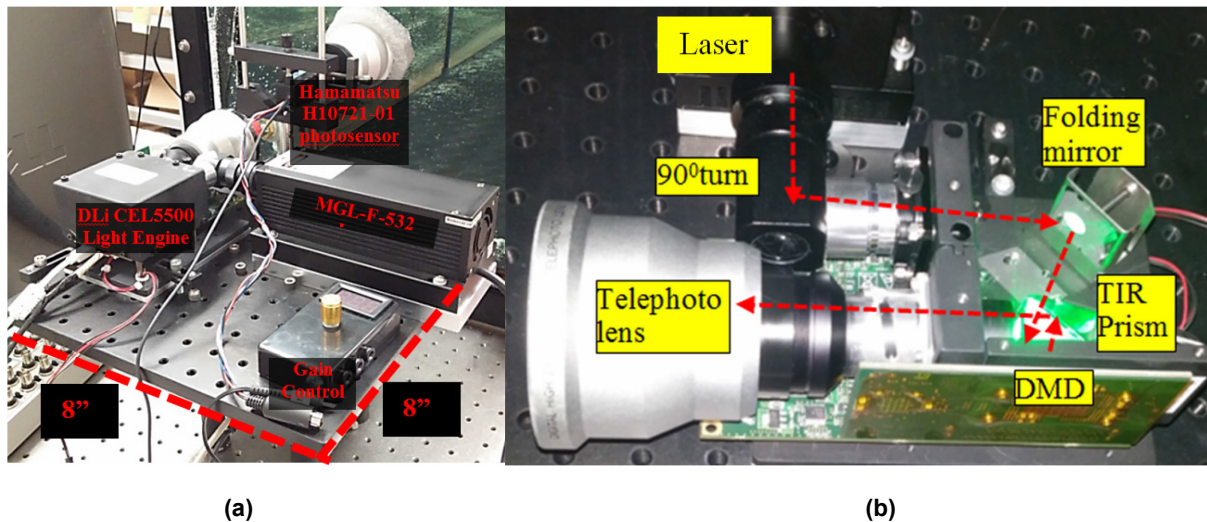
**Figure 4-46: Illustration of the New CLS System – The Overall System Architecture (a);
and the Optical Design of the Illumination Subsystem (b).**

By adopting the Hamamatsu H10721-01 photosensor, the bulky power supplies are replaced by a single wall charger and a gain control unit. The illumination source was a CNI MGL-F-532 CW laser with the actual optical power of 2.88 W and four-hour stability of 0.284%. The DLi CEL5500 DMD light engine was adopted as the Spatial Light Modulation (SLM) device. The whole system now fits on an 8" by 8" board (Figure 4-46(a)). The laser beam is piped into the light engine through a 90-degree angle turn and a custom-made connector to ensure the whole system is light tight (Figure 4-46(b)). A folding mirror directs the beam to the DMD surface. The DMD reflection is re-directed via a Total Internal Reflection (TIR) prism toward to the projection path. A 3X telephoto lens is used to generate a Field Of View (FOV) of 0.5 M at 5 M distance (required for the NRL-SSC test tank). Compared to Figure 4-45(b), the optical path was shortened

significantly. This new design resulted in a more compact system, more importantly, it improved the system robustness. The PMT adopted the same lens to generate an overlapping FOV.

The effectiveness of the predicted codebook under different turbulence streights are shown in Figure 4-47. The six curves represented the combination of the two types of codebook and the three types of input treatments [34]. Images with 2:1 compression ratio was used.
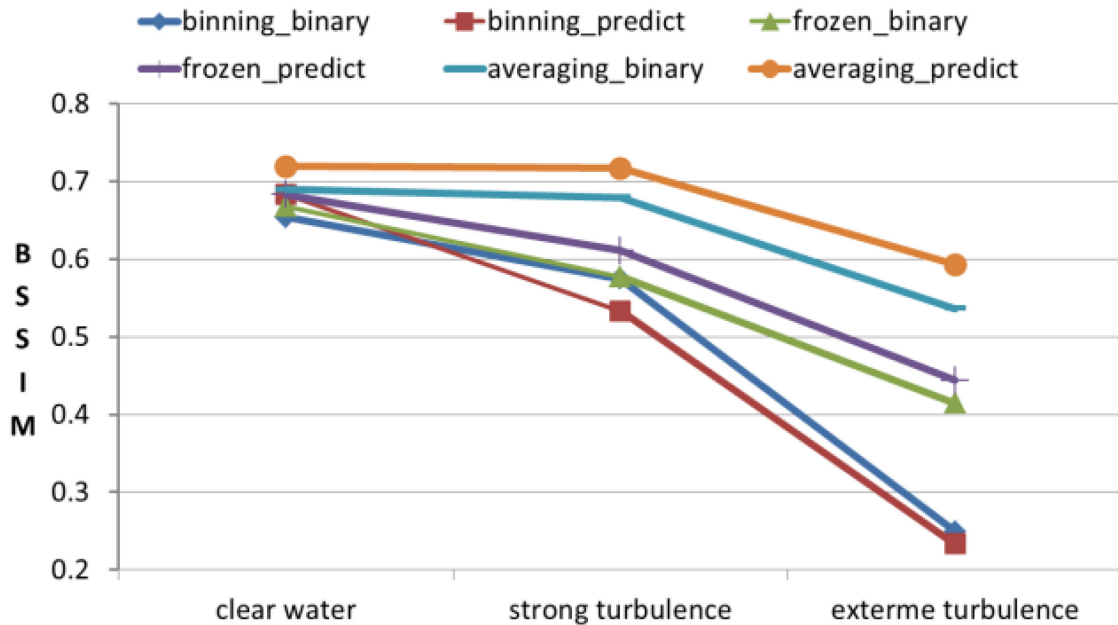
Figure 4-47: Comparison of Binary and Predicted Codebook Using Different Input Treatments (Binning, Frozen, Averaging) at the Different Turbulence Strengths. Images with 2:1 compression ratio were used.

From Figure 4-47, the Averaging treatment resulted in the most significant improvements. The Frozen treatment produced some improvements as well. On the other hand, with the Binning treatment, using the predicted codebook produced the least improvements over the binary codebook. Since using the predicted codebook essentially amounts to incorporating the deconvolution in the reconstruction process. The Averaging treatment improved the SNR of the measuremnts, and in turn, enhanced the image quality.

As an example, Figure 4-48 presented the reconstructed images at 2:1 compression ratio for the "Averaging" input treatment at the Extreme Turbulence strengths. Visual inspection of these images collaborated the BSSIM metric in Figure 4-47.

(a) *Averaging* treatment and binary codebook

(b) *Averaging* treatment and predicted codebook
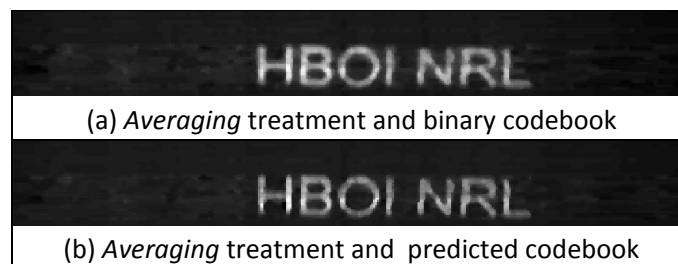
Figure 4-48: Comparison of Reconstructed Images at 2:1 Compression Ratio for the "Averaging" Input Treatments at the Extreme Turbulence Setting Using Binary and Predicted Codebook.

Chapter 5 – BENEFITS OF NUMERICAL SIMULATION

5.1   DEPTH MEASUREMENT ESTIMATION FOR 2D ACTIVE SYSTEM

Under the SET-219 group, DGA provides an illustration of the benefit of 2D numerical modeling of active sensor. The goal is to evaluate, for a specific scenario, the accuracy of the distance measurement of some image processing technics used to retrieve the 3D of the observed scene by 2D active system. Indeed, for such image processing technic, theoretical estimation of the range accuracy is hard to evaluate if you take all the noise contributors (MTF, scintillation, sensor noise, sampling and MTF). Numerical simulation is well adapted in that case.

Several methods for 3D scene reconstruction have been investigated in the past few years (ISL, IOSB, Selex/Leonardo). We focus on two main methods:

- The "double images" method for the 3D reconstruction of the scene developed by ISL [37]: an analysis of the gray level in the depth-intensity profile shows that, for a given sensor delay, i.e. for a given depth-positioning of the profile, the rising and falling edges of the profile contain the 3D information modulated by the object reflectance and the plateau will only contain the reflectance information. Based on this intrinsic property of the depth-intensity profile, one can extract the 3D information of a scene by using only two images. The 3D information is estimated by the ratio between the two images and the depth-intensity profile in the area A and B (see Figure 5-1).
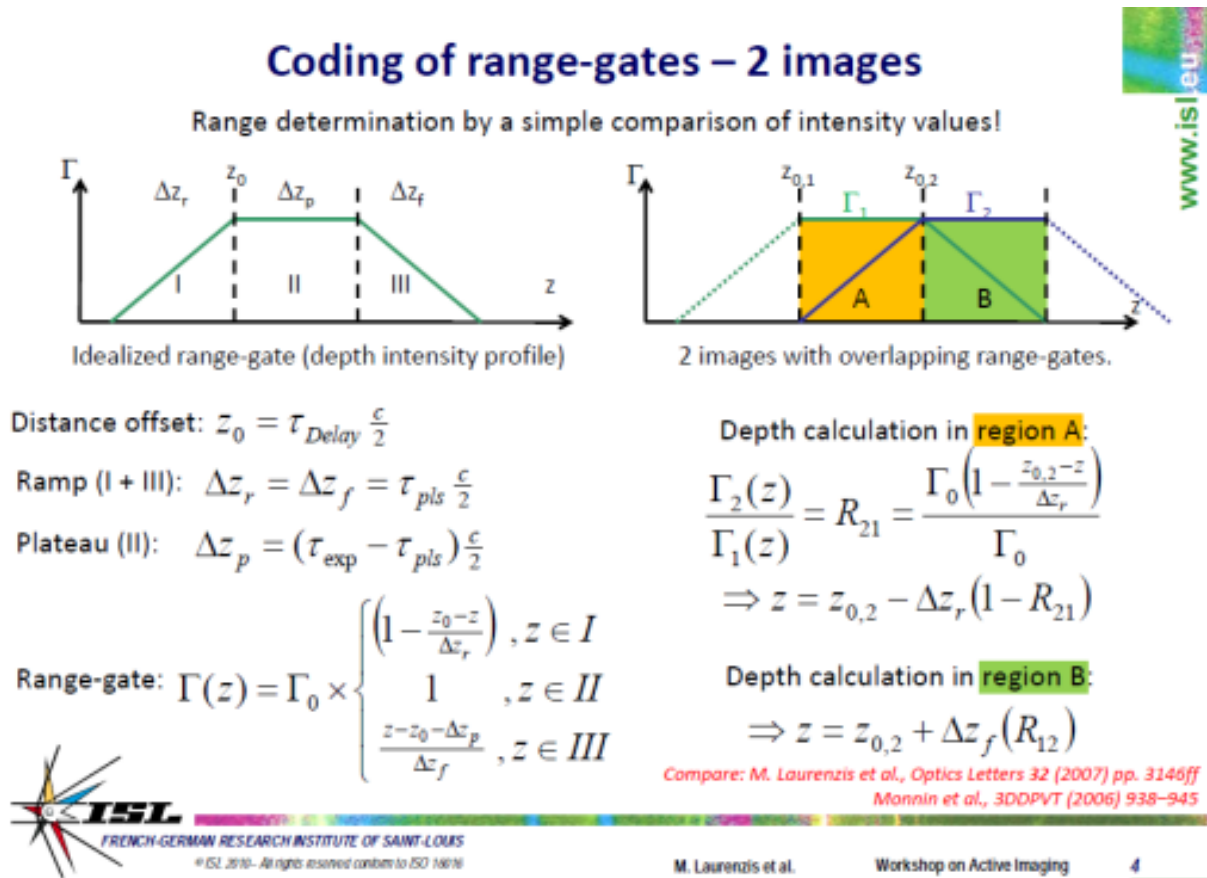
Figure 5-1: "Double Images" Method (Described in Ref. [37]).

- "Sliding gate" method (tomography): the tomography method [38] uses a narrow gate (short pulse width and gate duration) which is translated through the depth of the scene by systematic variation of the sensor gate delay (see Figure 5-2). Assuming a triangular depth-intensity profile, we can estimate the depth position by finding the maximum gray value in each pixel of the sensor.
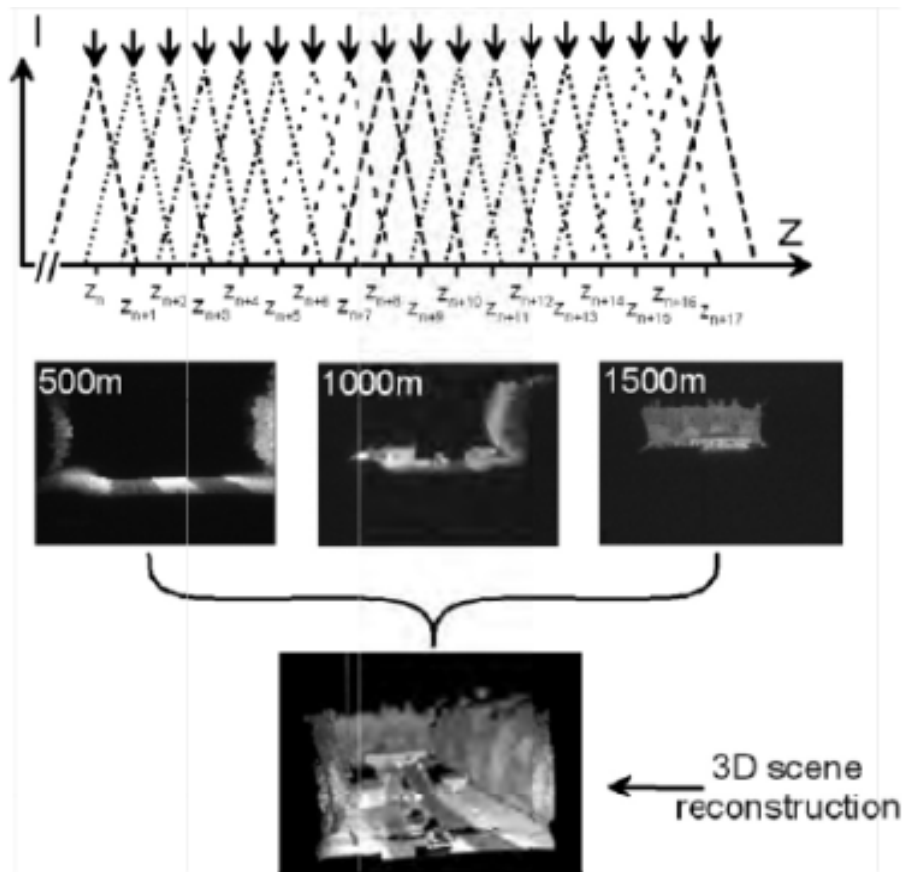
Figure 5-2: Sliding Gate Method (Described in Ref. [38]).

For this study, the synthetic scene at 4 km is used, with $C_n^2 = 1.10^{-14}$ m$^{-2/3}$, with and without frame averaging (over 30). The study assumes a similar setup of the laser and the receiver (optic and sensor) as defined in the previous paragraph, with the following modifications:

- For the "double images" method: in order to get the required gray level in the depth-intensity profile (trapeze shape), we change:

  - Laser pulse width   ➔ 200 ns (square temporal profile);

  - Sensor time integration   ➔ 400 ns (square temporal profile); and

  - 200 ns of delay in the time acquisition between the two images.

- For the "tomography" method: in order to get the required gray level in the depth-intensity profile (triangular shape), we change:

  - Laser pulse width   ➔ 150 ns (square temporal profile);

  - Sensor time integration   ➔ 150 ns (square temporal profile); and

  - 51 steps in the scan over the scene, each steps is separated by 10 ns.

The depth accuracy is estimated by calculating the standard deviation in the image coming from the difference between in the input Z map of the synthetic scene and the reconstructed Z map for the two algorithms. The analyzed area is restricted to the center of the target (see the white box in Figure 5-3 and Figure 5-4).

5.1.1 Perfect Case
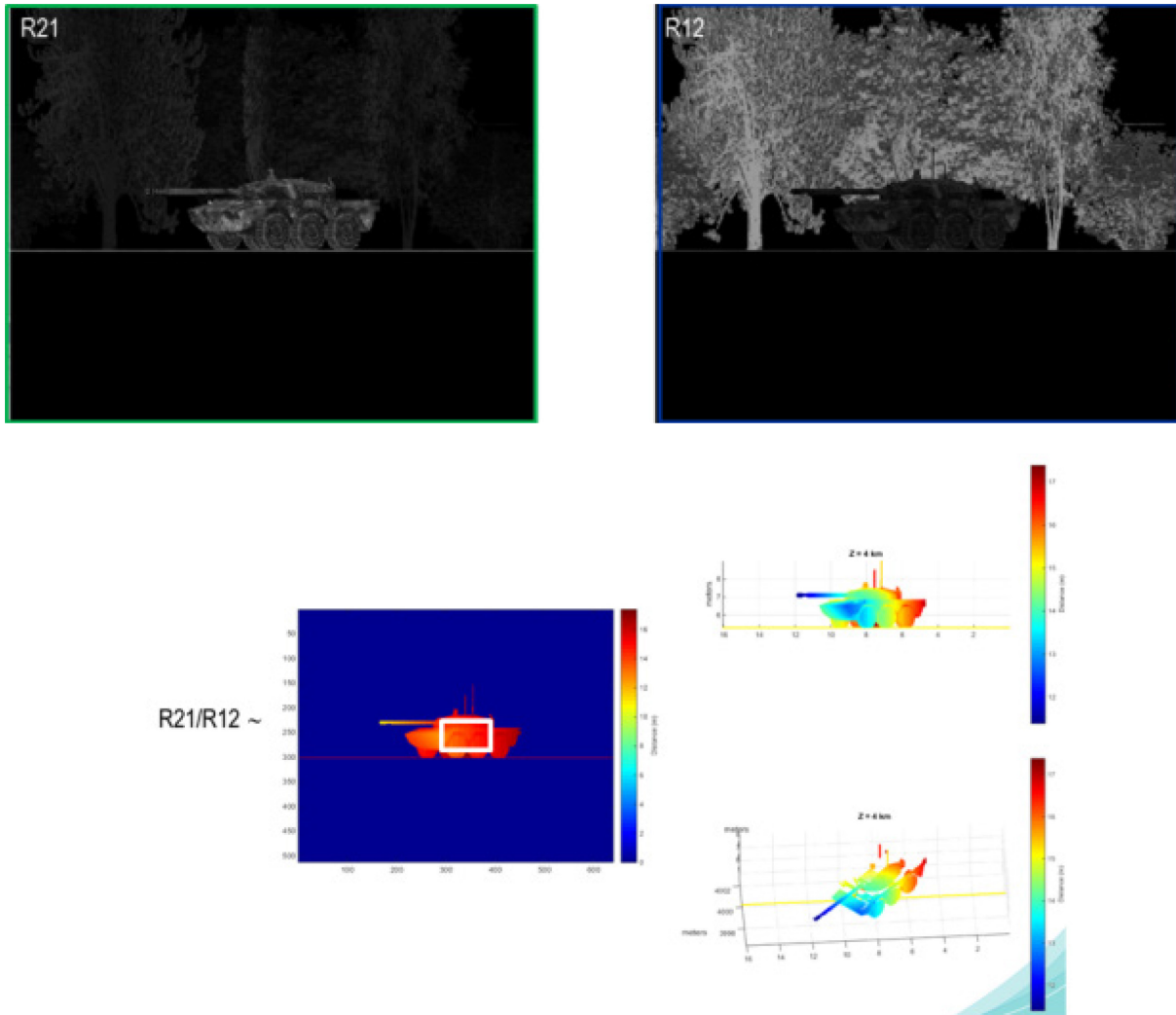
Figure 5-3: Perfect Case – Two "Sensor" Images (Top Left and Right) and the Reconstructed Z Map and 3D View (Bottom). The white box is the area where the accuracy is calculated (standard deviation between the input Z map and the reconstructed Z map).

5.1.2 Receiver MTF + Sensor Noise and Sampling + Scintillation

As we want to evaluate the noise contributors on the accuracy of the distance measurement, we estimate step by step the impact of all sources of noise in the image forming process (no noise, sensor noise including photon noise, MTF and sampling noise, optic MTF and scintillation, image averaging gain), mainly for the "double images" method.

Table 5-1 summarizes the results. Figure 5-3 (above) and Figure 5-4 (on the following page) also provide some illustrations, for two cases for the "double images" method:

- The perfect case, i.e., no MTF and no noise are considered. This steps help to estimate the simulation accuracy (ideally a 0 value should be found); and

- The real case, i.e., with the optical MTF + Sensor resampling + Sensor noise + Scintillation. This case represents the full sensor configuration.

We see that our simulation has a very low level of noise (2 – 3 mm). This allows good estimation of the noise of the different contributors.

Such a specific study, based on numerical simulation, allows ranking the noise contributors of the performance (relative distance accuracy). For the "two images" method, in our scenario, the scintillation and the noise sensor have a similar impact on the performance. To get good range accuracy (1 m RMS), frame averaging is needed. Then, the accuracy of the "double images" is close to the accuracy of the "tomography" method.

Such a conclusion is important to estimate the operational use of an active system. Some applications require that the total number of images be kept as small as possible, i.e.:

- Case of laser discretion; and

- Case of dynamic/moving object, where time integration is limited.

Here, even if the "double images" fitted a the first look the need of low number of pulses emitted (only two), we see that if we need good range accuracy, the averaging process is needed, and then the "double images" method will require 60 pulses, more than the pulses used for the tomography method (only 51 pulses for 1 meter of range accuracy).

Table 5-1: 3D Accuracy Results.

| Type of Noise	"Double Images" Method	"Tomography" Method
Simulation noise (perfect case)	∼ 3 mm	∼ 2 mm
Optical MTF + resampling	∼ 0.4 m	Not computed
Optical MTF + resampling + Sensor noise	∼ 7.2 m	Not computed
Optical MTF + resampling + Sensor noise + turbulence	∼ 7.8 m	Not computed
Optical MTF + resampling + turbulence	∼ 6.0 m	∼ 0.9 m
Optical MTF + resampling + Sensor noise + turbulence + frame averaging (M = 30)	∼ 1.5 m	Not computed
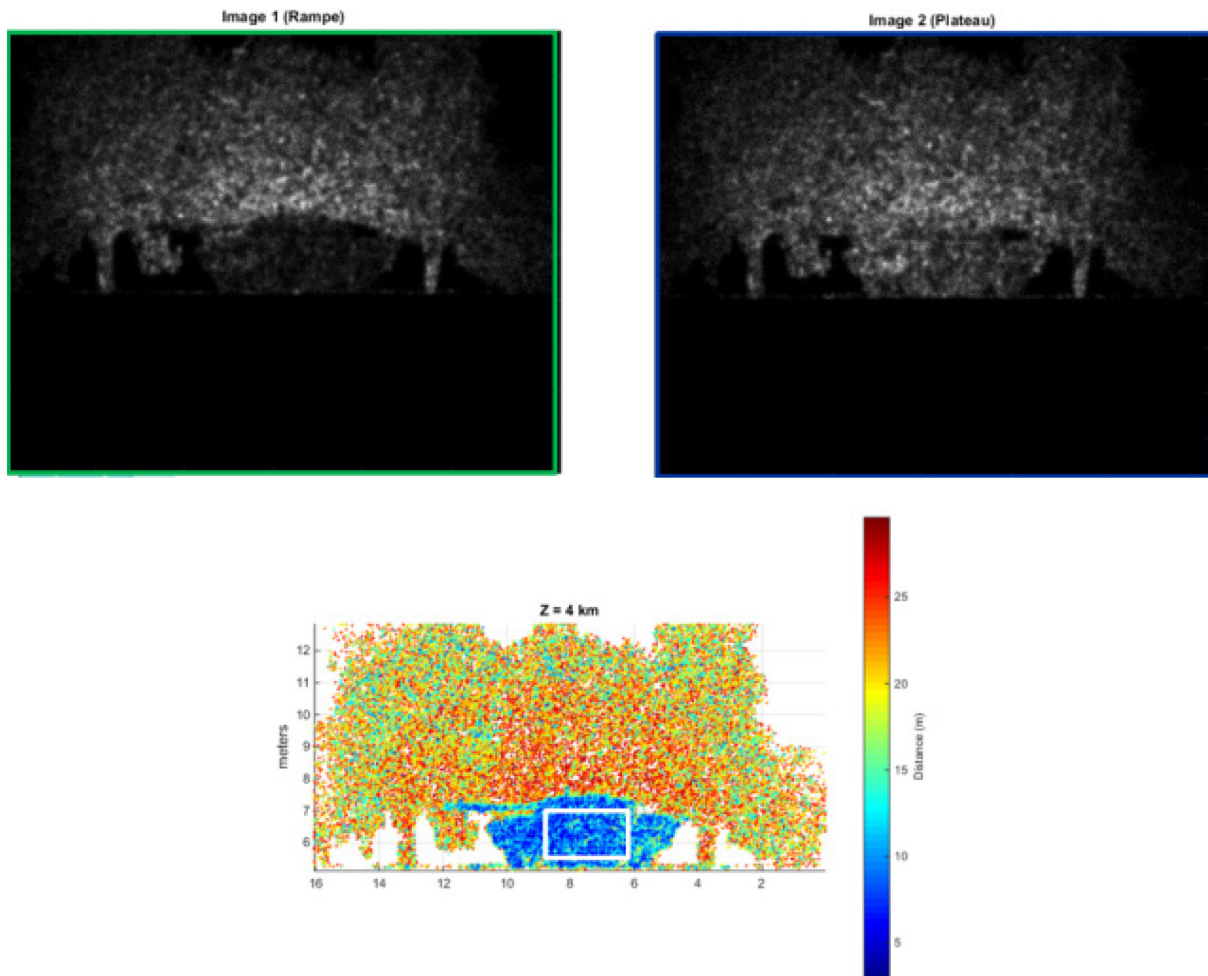
Figure 5-4: Receiver MTF + Sensor Noise + Scintillation – Two Sensor Images (Top Left and Right) and the Reconstructed Z Map (Bottom). The white box is the area where the accuracy is calculated (standard deviation between the input Z map and the reconstructed Z map).

Chapter 6 – CONCLUSION

6.1   CURRENT STATUS

Current active sensor modeling tools at France DGA are focus on 2D sensors. The modeling chain, mainly the simulation of the atmospheric effect on both ways, is available for flash active sensor, and is under development for a cumulative active sensor. Indeed, the noise of the turbulence is not to be considered the same for each type of sensor (for cumulative sensor, the scintillation pattern is reduced over the time exposure, the atmosphere MTF tends to the 'long exposure MTF').

Furthermore, the DGA modeling chain has already been validated through some national field trials for a 2D flash system. Ongoing field trials are being performed for the validation of a 2D cumulative system. Numerical modeling of a 2D active system will be used for future perception evaluations and metric evaluation for specific task (identification of specific set of target). Also, evaluation of the gain of image processing on range performance will be investigated. The active modeling chain will be coupled with a TOD (Triangle Orientation Discrimination) algorithm currently developed at DGA.

The Canada DRDC active imaging model OTISS-A is currently under development. However, in its current state OTISS-A can simulate targets with inclined weakly specular surfaces. Furthermore, the OTISS-A model can simulate specular surfaces with a coherence length matrix which may be anisotropic and position dependant. In addition, OTISS-A simulates the propagation of the illuminating pulse and the return radiance through the same turbulence, thereby creating a correlation between the turbulent illumination and imaging.

The model currently implemented at the Germany Fraunhofer IOSB takes advantage of a widely used technique for forward beam propagation, the FFT split step method. As such its results are easy to validate with other works. On the other hand, the backward propagation model has been empirically established from NATO RTG-40 field trial results. Consequently, simulation based on this model is assumed to reproduce real imagery with high fidelity within the range of validity of this empirical model. Furthermore, simulations based on this backpropagation model are computationally efficient.

The Sweden FOI-LadarSim has simulation modules for several active imaging systems (gated viewing, 1D profiling, and 3D LIDAR), including a recently developed photon counting LIDAR detector module. FOI-LadarSim combines advanced scenario setups with the ability to change the sensor positioning and aiming direction, and the sensor internal parameters. The scene model to be viewed by the sensor can be built by an external editor and imported into FOI-LadarSim, or be built by separate objects such as trees and vehicles that are assembled into a complete scene using script commands. In advanced scenario setups it is possible to have moving scene objects and a moving sensor combined, e.g. with a stochastic model describing the uncertainties for positioning of the sensor.

Additional tools at FOI include simulation models for high level scenario/operator evaluation (MSS-lab) and physical models for underwater active optical sensing (airborne LIDAR system model including air-water interface model, and evaluation of Monte Carlo photon simulations in relation to experiments).

The US Army NVESD is continuing to utilize DIRSIG for both 2D and 3D ladar simulated scene generation. The US Naval Research Lab at SSC is continuing to develop the SiTTE tool to study underwater imaging scene simulation.

6.2   SIMULATION CAPABILITY GAPS

Improving the prediction of the fidelity of SWIR synthetic image remains a challenge. Achieving it requires measurement of optical properties of materials (roughness, absorption, etc.), in order to predict BRDF.

DGA has made some measurements (see Figure 6-1) and research and development of a database of BRDF for a variety of materials is ongoing. Such a database will be used in SE Workbench for future scene generation in the SWIR band.
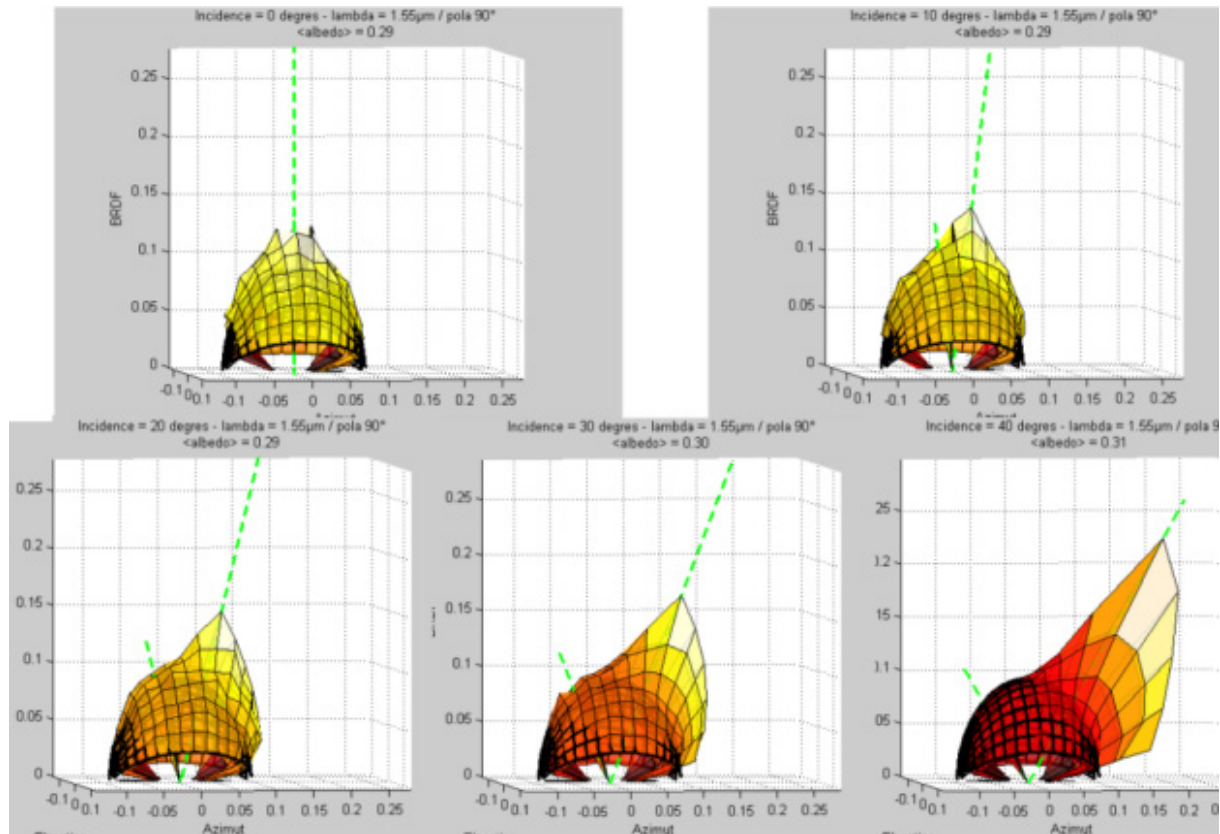
Figure 6-1: BRDF of a Green Canvas @ 1.5 µm for Several Incidence Angles
(0, 10, 20, 30, and 40 Degrees). The incident ray (short dash green line)
and the reflected ray (long dash green line) are depicted.

Investigations will also be performed for others physical effects that affect active imaging, like having the capability to manage polarization and backscattering effects, especially under poor visibility condition. The last point of focus is the capability to estimate the fidelity of the generated sensor image compared to the real environment and sensor. Investigations remain to be done in metrics for image quality estimation (SSIM adapted for noisy sensor as active sensor, others methods, etc.).

The DRDC active imaging model OTISS-A is designed for weak optical turbulence. Further development is required to simulate cases where there is moderate to strong optical turbulent saturation. OTISS-A also cannot model speckle effects created by the illuminating beam. As explained in Annex A, OTISS-A assumes the target surfaces are weakly specular in order to justify the use of first-order Taylor expansions. Such a procedure, while mathematically convenient, can produce inaccuracies in the simulation results for certain conditions. More work is therefore required to give OTISS-A greater range of applicability.

As an empirical model the backscattering model used for active imaging simulation is valid within the range of conditions under which the corresponding field trail was conducted. Specifically, the current model is unable to deal with spatially varying C_n^2 for slanted path. Additionally, field trial imagery was obtained under broadband illumination. Therefore, further work would be needed to extend it for monochromatic illumination and investigate related coherence effect on resulting images.

The FOI-LadarSim has the capability to simulate many types of sensors and scenarios obtained through different modules. Simulations of target BRDF is implemented but requires testing and comparison with experimental data. Also, the turbulence module is of interest for comparison with experimental data and with other models. Development and evaluation is required to improve the computation performance for some scenarios such as FOPEN and photon counting. Realistic and physically correct simulations of foliage penetration can be done with high lateral sub-resolution (many simulated rays per physical detector pixel). Such simulations require high computation (CPU/GPU) performance and are today made for scenarios limited in space (small area, few trees, bushes and targets) and time (few seconds). Simulation of photon counting is valuable for different topics including system design, optimization, and signal processing studies.

6.3 RECOMMENDATIONS FOR FUTURE ACTIVITIES

What follows is a series of nation-based recommendations. First of all, France DGA recommends:

- Complete work on image quality assessment: for that, specific trials could be done or one can reuse specific database image like RTG-40. The goal is to compare ground true images and modeled images with specific set of metrics to be determined; and

- Complete the modeling capability of active SWIR scene, by gathering optical properties of different kinds of materiel. Natural (wood, grass, etc.) and artificial (concrete, paint, etc.) backgrounds have to be considered.

Future activities for the follow-on group to NATO SET-219 could include active imaging trials for the validation of the models. If possible, such a trial should include targets with a variety of known BRDFs, both with and without turbulence. This could entail a trial in controlled conditions, such as an indoor facility. But even with such trial data, metrics will have to be found that could meaningfully compare the data with the simulation outputs. These metrics would probably consist of statistical parameters, such as the average image or the image variance, with a comparison measure such as the *Structural Similarity Index Measure* (SSIM) [39]. Care would have to be used to remove or attenuate the effects of noise or imperfections in the measured images.

Optical imaging in the underwater environment is a challenging problem. The water body introduces many image degrading interferences. One of such interferences is the underwater turbulence due to the pockets of water of varying temperature, density, and index of refraction (i.e. temperature gradients in the deep sea, air-water boundary, etc.). Such turbulence layers cause beam spreading and wandering. As a result, the acquired image will be distorted and loss of detail. Compared with the image degradation caused by the turbid water, the time and spatial varying nature of the turbulence poses a different and maybe more difficult challenge. Optical turbulence can be described by a time and spatial varying Modulation Transfer Function (MTF) [31], [35]. To maximize the investment return in experimental setup and rate of success replicating environmental conditions, NRL has implemented a controlled environment where turbulence and turbidity intensity can be simulated. In turn, this validated system has been used to investigate degradation effects on beam propagation and imaging systems. Through collaboration within SET framework, we have achieved better understanding of the environmental parameters and system response function.

The simulation of active gated viewing systems by Fraunhofer IOSB is almost completed and needs to be validated. We'd suggest to plan and run a new joint field trial by a follow-up group in order to collect validation data. Such a trial should also include data collection by different profiling systems. The scenarios for the data collections must be carefully planned. This includes not only the specification of test objects and cameras, but also taking into account local range (test area) circumstances – e.g. usable distances between test objects and cameras; availability of environmental data, etc. In this study we defined simple scenes at quite long distances. In this way, it has been easier to compare the different simulations – but in the field, unobscured views of test targets at such long ranges (distances) can hardly be found. For a new trial, new set-ups (at shorter distances) must be defined.

The validation effort requires – besides the data collection itself – the comparison of collected data with the simulated data. Currently, there are no single accepted metrics (or published methods) known for numerical comparison of turbulent images. Instead, a few figure-of-merit (like SSIM, MTF, etc.) are calculated and used in combination to support image quality evaluation. There is a need for an appropriate metric/method, which supports the calculation of a single numerical value that might be used for automatic image ranking. The search for such a metrics/method/algorithm as well as the development and testing (accompanied by observer trials) should be continued within the follow-up group. The method should be robust enough to be applicable to images from different application fields (e.g. in-air and underwater recordings).

Simulation models are important for understanding physical limits, and for maximizing the capabilities of existing and future operational systems. Environmental conditions (e.g. turbulence, occluding vegetation, and water) and target properties (size, shape, BRDF) affect active sensors and are therefore of common interest for all such sensor types and technologies. Future activities of interest for a follow-on group to NATO SET-219 could include comparison of simulated data with experimental data. Experimental data could be either existing or new data collected in indoor or outdoor experiments with thorough documentation of environmental (turbulence, vegetation) and target parameters (BRDF). Experimental data could be used both for validation of individual models and comparison of models to gain insight where model assumptions are valid or not. Further work could include extension of existing models for improved accuracy and performance, and development of new models to handle emerging active imaging technologies such as photon counting and compressive sensing both in air and underwater.

Chapter 7 – REFERENCES

[1] O.K. Steinvall, H. Olsson, G. Bolander, C.A. Groenwall and D. Letalick, "Gated viewing for target detection and target recognition," in *Proc. SPIE 3707*, 1999.

[2] A.F. Milton, G. Klager and T. Bowman, "Low cost sensors for UGVs," in *Proc. SPIE 4024*, 2000.

[3] J. Busck, "Underwater 3-D optical imaging with gated viewing laser radar," *Optical Engineering*, vol. 44, 2005.

[4] R.L. Espinola, E.L. Jacobs, C.E. Halford, R. Vollmerhausen and D.H. Tofsted, "Modeling the target acquisition performance of active imaging systems," *Optics Express*, vol. 15, no. 7, pp. 3816-3832, 2007.

[5] L.C. Andrews and R.L. Phillips, Laser beam propagation through random media, Bellingham, WA: SPIE Press, 2005.

[6] M.C. Roggemann and B. Welsh, Imaging through turbulence, Boca Raton, FL: CRC Press, 1996.

[7] Final report of SET-072, "Modeling of Active Imaging Systems," NATO RTO, Neuilly-sur-Seine Cedex, 2009.

[8] Final Report of SET-156, "Modeling of Active EO-Imaging Systems," NATO STO, Neuilly-sur-Seine Cedex, 2015.

[9] O. Steinvall and M. Tulldahl, "Laser range profiling for small target recognition," *Optical Engineering*, vol. 56, pp. 031206-1-16, 2016.

[10] O. Steinvall, T. Chevalier and C.A. Groenwall, "Simulation and modeling of laser range profiling and imaging of small surface vessels," *Optical Engineering*, vol. 53, pp. 013109-1-16, 2014.

[11] Final Report of SET-056, "Integration of Radar and Infrared," NATO RTO, 2009.

[12] P.C. Grosse, "Analyse des effets de la turbulence sur l'imagerie optronique," Ecoles de Saint-Cyr, Coetquidan, 2004.

[13] G. Potvin, J.L. Forand and D. Dion, "Some space-time statistics of the turbulence point-spread function," *J. Opt. Soc. Am. A*, vol. 24, no. 3, pp. 753-763, 2007.

[14] H.D. Brosset, "Analyse des effets de l'etalement turbulent sur l'imagerie," Ecoles de Saint-Cyr, Coetquidan, 2008.

[15] G. Potvin, J.L. Forand and D. Dion, "A parametric model for simulating turbulence effects on imaging systems," TR 2006-787, DRDC Valcartier, Quebec City, 2007.

[16] G. Potvin, J.L. Forand and D. Dion, "A simple physical model for simulating turbulent imaging," in *Proc. SPIE*, 2011.

[17] B.M. Welsh, "A Fourier Series Based Atmospheric Phase Screen Generator for Simulating Non Isoplanatic Geometries and Temporal Evolution," AFIT, 1999.

[18] E. Repasi and R. Weiss, "Analysis of image distortions by atmospheric turbulence and computer simulation of turbulence effects," in *Proc. SPIE 6941*, 2008.

[19] B.A. Ragozzine, "Modeling the Point Spread Function Using Principal Component Analysis," Ohio University, 2008.

[20] G. Monnier, F.-R. Duval and S. Amram, "GPU-based simulation of optical propagation through turbulence for active and passive imaging," in *Proc. SPIE 9242*, 2014.

[21] J.A. Fleck, J.R. Morris and M.D. Feit, "Time-dependent propagation of high energy laser beams through the atmosphere," *Applied Physics*, vol. 10, no. 2, pp. 129-160, 1976.

[22] T.W. Du Bosq and E. Repasi, "Detector integration time dependent atmospheric turbulence imaging simulation," in *Proc. SPIE 9452*, 2015.

[23] T.R. Chevalier and K.O. Steinvall, "Laser radar modeling for simulation and performance evaluation," in *Proc. SPIE 7482*, 2009.

[24] F. Bennet and S. Fenelius, "SceneServer – a 3D software assisting developers of computer vision algorithms," Swedish Defence Research Agency (FOI), 2003.

[25] P. Jonsson, M. Tulldahl, J. Hedborg, M. Henriksson and L. Sjoqvist, "Experimental evaluation of penetration capabilities of a Geiger-mode APD array laser radar system," in *Proc. SPIE 10434*, 2017.

[26] O. Steinvall, L. Sjoqvist and M. Henriksson, "Photon counting ladar work at FOI, Sweden," in *Proc. SPIE 8375*, 2012.

[27] S. Matt, W. Hou, W. Goode and S. Hellman, "Introducing SiTTE: A controlled laboratory setting to study the impact of turbulent fluctuations on light propagation in the underwater environment," *Optics Express*, vol. 25, pp. 5662-5683, 2017.

[28] S. Matt, W. Hou and A. Kanaev, "Numerical simulations of turbulence impact on optical signal transmission and near-surface turbulence," NRL DOD HPCMP Annual Report FY15, 2015.

[29] S. Matt, W. Hou, W. Goode, G. Liu, M. Han, A. Kanaev and S. Restaino, "A controlled laboratory environment to study EO signal degradation due to underwater turbulence," in *Proc. SPIE 9459*, 2015.

[30] S. Matt, W. Hou and W. Goode, "The impact of turbulent fluctuations on light propagation in a controlled environment," in *Proc. SPIE 9111*, 2014.

[31] W. Hou, "A simple underwater imaging model," *Optics Letters*, vol. 34, pp. 2688-2690, 2009.

[32] J.S. Jaffe, "Underwater optical imaging: The past, the present, and the prospects," *IEEE J. Ocean. Eng.*, vol. 40, pp. 683-700, 2015.

[33] Z.Q. Zeng, S. Fu, H.H. Zhang, Y.H. Dong and J.L. Cheng, "A survey of underwater optical wireless communications," *Communications Surveys Tuts.*, vol. 19, pp. 204-238, 2017.

[34] B. Ouyang, W. Hou, C. Gong, F. Dalgleish, F. Caimi, A. Vuorenkoski, G. Nootz, X. Xiao and D. Voelz, "Experimental study of a compressive line sensing imaging system in a turbulent environment," *Applied Optics*, vol. 55, pp. 8523-8531, 2016.

[35] W. Hou, S. Woods, E. Jarosz, W. Goode and A. Wiedemann, "Optical turbulence on underwater image degradation in natural environments," *Applied Optics*, vol. 51, pp. 2678-2686, 2012.

[36] S.E. Johnson, "Foliage penetration optimization for geiger-mode avalanche photodiode lidar," in *Proc. SPIE 8731*, 2013.

[37] M. Laurenzis and E. Bacher, "3D Imaging from Coded Range-Gated Images," French-German Research Institute of Saint-Louis, Active Imaging Workshop, 2011.

[38] F. Christnacher, "3D laser gated viewing from a moving submarine platform," in *Proc. SPIE 9250*, 2014.

[39] Z. Wang, A. Bovik, H.R. Sheikh and E.P. Simoncelli, "Image quality assessment: From error visibility to structural similarity," *IEEE Trans. Image Proc.*, vol. 13, no. 4, pp. 600-612, 2004.

Annex A – THE BRDF FOR TURBULENT ACTIVE IMAGING

Let us suppose we have a scalar electric field $E(\vec{\rho}, z)$ propagating along the line-of-sight of an active imaging system (z-axis) towards the surface of a target which is roughly along the plane described by the two-dimensional vector $\vec{\rho}$ at $z = 0$, whereas the imager and source are located on the plane at $z = L$. In the paraxial approximation, the electric field is approximated as $E = e^{ikz}u$, where k is the wavenumber of the radiation. The function u propagates as:

$$\frac{\partial u}{\partial z} - \frac{i}{2k}\nabla_\rho^2 u - ikn_1 u = 0, \tag{A.1}$$

where n_1 is the refractive index fluctuation. The incident *Mutual Coherence Function* (MCF) on the target surface is defined as:

$$\Gamma_i(\vec{R}, \vec{\Delta}, 0) = u_i\left(\vec{R} + \tfrac{1}{2}\vec{\Delta}, 0\right) u_i^*\left(\vec{R} - \tfrac{1}{2}\vec{\Delta}, 0\right), \tag{A.2}$$

where u_i is the incident function, $\vec{R} = (\vec{\rho} + \vec{\rho}')/2$ is the centre coordinate and $\vec{\Delta} = \vec{\rho} - \vec{\rho}'$ is the coordinate interval. The MCF is subject to turbulent fluctuations, but contains no information about rays and their orientation (as in Figure 3-2). We remedy this by introducing the Wigner function:

$$W_i(\vec{R}, \vec{P}, 0) = \int d^2\Delta \, \Gamma_i(\vec{R}, \vec{\Delta}, 0) \exp\left[-ik\vec{P}\cdot\vec{\Delta}\right], \tag{A.3}$$

where $\vec{P}$ is the slope of the ray. We assume that the outgoing Wigner function is related to the incident Wigner function by an integral transform:

$$W_o(\vec{R}, \vec{P}, 0) = \int d^2R' \int d^2P' W_i(\vec{R}', \vec{P}', 0) T(\vec{R}, \vec{P}, \vec{R}', \vec{P}'). \tag{A.4}$$

We assume that the transfer function T is a Gaussian scattering function:

$$T(\vec{R}, \vec{P}, \vec{R}', \vec{P}') = I(\vec{R}) \frac{\delta(\vec{R} - \vec{R}')}{2\pi\sqrt{|\Sigma|}} \times \exp\left[-\tfrac{1}{2}(P_i + P_i' - 2Q_i)\Sigma_{ij}^{-1}(P_j + P_j' - 2Q_j)\right], \tag{A.5}$$

where the symmetric matrix Σ_{ij} represents the spreads of the scattering function, $\vec{Q}$ is the slope of the normal of the target surface, $I(\vec{R})$ is the surface reflectance and we used the Einstein summation convention. This transfer function is our way of modelling the *Bi-directional Reflectance Distribution Function* (BRDF). In terms of the MCFs, we get the straightforward relation:

$$\Gamma_o(\vec{R}, \vec{\Delta}, 0) = \Gamma_i(\vec{R}, -\vec{\Delta}, 0)I(\vec{R})\exp\left[-\tfrac{k^2}{2}\Delta_i\Sigma_{ij}\Delta_j + 2ik\vec{Q}\cdot\vec{\Delta}\right]. \tag{A.6}$$

The momentum spread matrix Σ_{ij} is in general a function of position on the target surface and is dimensionless. Instead, it is the matrix $k^2\Sigma_{ij}$ that represents the surface's inverse coherence length squared. Note that for a Lambertian surface, we have $\Sigma_{ij} = \sigma^2\delta_{ij}$ where $\sigma^2 \gg 1$ because the surface scatters over a wide range of angles. In that case, the exponential approximates a Dirac delta function $\delta(\Delta)$ and the surface slope no longer matters.

The spherical wave propagator of the function u from a point on the target surface to a point source at $(\vec{\rho}_s, L)$ is given as:

$$G_0(\vec{\rho}, \vec{\rho}_s) = \frac{k}{2\pi i L} \exp\left[\frac{ik}{2L}(\vec{\rho}_s - \vec{\rho})^2\right]. \tag{A.7}$$

If weak turbulence is present, we modify this expression by adding a log-amplitude fluctuation function $\chi(\vec{\rho}, \vec{\rho}_s)$ and a phase fluctuation function $S(\vec{\rho}, \vec{\rho}_s)$ in keeping with the Rytov approximation:

$$G(\vec{\rho}, \vec{\rho}_s) = G_0(\vec{\rho}, \vec{\rho}_s) \exp[\chi(\vec{\rho}, \vec{\rho}_s) + iS(\vec{\rho}, \vec{\rho}_s)]. \tag{A.8}$$

Readers may consult Ref. [15] for more information on the weak turbulence Rytov approximation for optical propagation. From Eq. (A.8) we obtain the incident MCF:

$$\Gamma_i(\vec{R}, \vec{\Delta}, 0) \approx \left(\frac{k}{2\pi L}\right)^2 \exp\left[\frac{ik}{L}(\vec{R}_s - \vec{R}) \cdot \vec{\Delta} + 2\chi(\vec{R}, \vec{R}_s) - i\vec{\Delta} \cdot \vec{\nabla}S(\vec{R}, \vec{R}_s)\right], \tag{A.9}$$

where we expanded χ and S in a Taylor's expansion to first order in Δ. From Eq. (A.6) the outgoing MCF is:

$$\Gamma_o(\vec{R}, \vec{\Delta}, 0) \approx I(\vec{R})\left(\frac{k}{2\pi L}\right)^2 \exp\left[2\chi(\vec{R}, \vec{R}_s) - \frac{k^2}{2}\Delta_i \Sigma_{ij} \Delta_j + ik\vec{\xi} \cdot \vec{\Delta}\right], \tag{A.10}$$

where:

$$\vec{\xi} = \frac{\vec{R} - \vec{R}_s}{L} + 2\vec{Q} + \frac{1}{k}\vec{\nabla}S(\vec{R}, \vec{R}_s). \tag{A.11}$$

We now have to propagate in outgoing MCF on the target surface to the surface of the imaging system's lens, which we denote with the subscript l:

$$\Gamma_l(\vec{R}_l, \vec{\Delta}_l, L) = \left(\frac{k}{2\pi L}\right)^2 \int d^2 R \int d^2 \Delta\, \Gamma_o(\vec{R}, \vec{\Delta}, 0) \exp\left[\frac{ik}{L}(\vec{R}_l - \vec{R}) \cdot (\vec{\Delta}_l - \vec{\Delta})\right]$$
$$\times \exp[2\chi(\vec{R}, \vec{R}_l) + \vec{\Delta} \cdot \vec{\nabla}S(\vec{R}, \vec{R}_l) + \vec{\Delta}_l \cdot \vec{\nabla}_l S(\vec{R}, \vec{R}_l)], \tag{A.12}$$

where we again expanded the log-amplitude and phase fluctuation fields to first order in Δ. We integrate with respect to Δ and obtain:

$$\Gamma_l(\vec{R}_l, \vec{\Delta}_l, L) = \left(\frac{k}{2\pi L^2}\right)^2 \int d^2 R\, I(\vec{R})\mathcal{A}(\vec{R}) \exp\left[\frac{ik}{L}(\vec{R}_l - \vec{R}) \cdot \vec{\Delta}_l\right]$$
$$\times \exp[2\chi(\vec{R}, \vec{R}_s) + 2\chi(\vec{R}, \vec{R}_l) + \vec{\Delta}_l \cdot \vec{\nabla}_l S(\vec{R}, \vec{R}_l)], \tag{A.13}$$

where:

$$\mathcal{A}(\vec{R}) = \frac{1}{2\pi\sqrt{|\Sigma|}} \exp\left[-\frac{1}{2}\gamma_i \Sigma_{ij}^{-1} \gamma_j\right], \tag{A.14}$$

and where:

$$\vec{\gamma} = 2\frac{\vec{R}}{L} + 2\vec{Q} - \frac{\vec{R}_s}{L} - \frac{\vec{R}_l}{L} + \frac{1}{k}\vec{\nabla}S(\vec{R}, \vec{R}_s) + \frac{1}{k}\vec{\nabla}S(\vec{R}, \vec{R}_l). \tag{A.15}$$

The vector $\vec{\gamma}$ contains information on the incoming and outgoing slopes of the unperturbed rays, along with the slope of the surface and the perturbations caused by the turbulence. Therefore, if we have $\vec{\gamma} = 0$, then the incoming ray hits the target surface at the right place and at the right angle so that it enters the imager (as illustrated in Figure 3-1). The factor $\mathcal{A}$ represents the effects of the specular surface. In other words, for a large coherence length we have $\Sigma_{ij}^{-1} \gg 1$ and $\mathcal{A}$ becomes very sensitive to the magnitude of $\vec{\gamma}$, whereas for small coherence lengths we have $\Sigma_{ij}^{-1} \to 0$ and $\mathcal{A}$ becomes insensitive to any value of $\vec{\gamma}$.

Note that we only consider surfaces that are weakly specular in that the coherence length is longer than the wavelength but significantly smaller than Fried's parameter, $r_0 = (0.55k^2LC_n^2)^{-3/5}$. Note also that the DRDC OTISS-A model does not use the χ and S fields directly, but a modified version of them that takes into account the aperture averaging of the imager.

REPORT DOCUMENTATION PAGE

1. Recipient's Reference	2. Originator's References	3. Further Reference	4. Security Classification of Document
	STO-TR-SET-219 AC/323(SET-219)TP/864	ISBN 978-92-837-2188-8	PUBLIC RELEASE

5. Originator	Science and Technology Organization North Atlantic Treaty Organization BP 25, F-92201 Neuilly-sur-Seine Cedex, France

6. Title	Simulation of Active Imaging Systems

7. Presented at/Sponsored by

Final Report of SET-219.

8. Author(s)/Editor(s)	9. Date
Multiple	December 2018

10. Author's/Editor's Address	11. Pages
Multiple	100

12. Distribution Statement	There are no restrictions on the distribution of this document. Information about the availability of this and other STO unclassified publications is given on the back cover.

13. Keywords/Descriptors

1D / 2D / 3D	Image processing
Active imaging	LIDAR
EOIR sensor system	Numerical simulation

14. Abstract

Active imaging systems offer the promise of significantly improved tactical performance compared to passive military systems operating on ground, in air, and underwater. These improvements would include, but not be limited to: i) Extending the ability to operate when passive sensors will not perform satisfactorily; ii) Improving target recognition and identification performance; and iii) Improving capability to determine the exact nature of the activity being pursued by individuals or vehicles at increased ranges.

CENTRES DE DIFFUSION NATIONAUX

ALLEMAGNE
Streitkräfteamt / Abteilung III
Fachinformationszentrum der Bundeswehr (FIZBw)
Gorch-Fock-Straße 7, D-53229 Bonn

BELGIQUE
Royal High Institute for Defence – KHID/IRSD/RHID
Management of Scientific & Technological Research
for Defence, National STO Coordinator
Royal Military Academy – Campus Renaissance
Renaissancelaan 30, 1000 Bruxelles

BULGARIE
Ministry of Defence
Defence Institute "Prof. Tsvetan Lazarov"
"Tsvetan Lazarov" bul no.2
1592 Sofia

CANADA
DGSlST 2
Recherche et développement pour la défense Canada
60 Moodie Drive (7N-1-F20)
Ottawa, Ontario K1A 0K2

DANEMARK
Danish Acquisition and Logistics Organization
(DALO)
Lautrupbjerg 1-5
2750 Ballerup

ESPAGNE
Área de Cooperación Internacional en I+D
SDGPLATIN (DGAM)
C/ Arturo Soria 289
28033 Madrid

ESTONIE
Estonian National Defence College
Centre for Applied Research
Riia str 12
Tartu 51013

ETATS-UNIS
Defense Technical Information Center
8725 John J. Kingman Road
Fort Belvoir, VA 22060-6218

FRANCE
O.N.E.R.A. (ISP)
29, Avenue de la Division Leclerc
BP 72
92322 Châtillon Cedex

GRECE (Correspondant)
Defence Industry & Research General
Directorate, Research Directorate
Fakinos Base Camp, S.T.G. 1020
Holargos, Athens

HONGRIE
Hungarian Ministry of Defence
Development and Logistics Agency
P.O.B. 25
H-1885 Budapest

ITALIE
Ten Col Renato NARO
Capo servizio Gestione della Conoscenza
F. Baracca Military Airport "Comparto A"
Via di Centocelle, 301
00175, Rome

LUXEMBOURG
Voir Belgique

NORVEGE
Norwegian Defence Research
Establishment
Attn: Biblioteket
P.O. Box 25
NO-2007 Kjeller

PAYS-BAS
Royal Netherlands Military
Academy Library
P.O. Box 90.002
4800 PA Breda

POLOGNE
Centralna Biblioteka Wojskowa
ul. Ostrobramska 109
04-041 Warszawa

PORTUGAL
Estado Maior da Força Aérea
SDFA – Centro de Documentação
Alfragide
P-2720 Amadora

REPUBLIQUE TCHEQUE
Vojenský technický ústav s.p.
CZ Distribution Information Centre
Mladoboleslavská 944
PO Box 18
197 06 Praha 9

ROUMANIE
Romanian National Distribution
Centre
Armaments Department
9-11, Drumul Taberei Street
Sector 6
061353 Bucharest

ROYAUME-UNI
Dstl Records Centre
Rm G02, ISAT F, Building 5
Dstl Porton Down
Salisbury SP4 0JQ

SLOVAQUIE
Akadémia ozbrojených síl gen.
M.R. Štefánika, Distribučné a
informačné stredisko STO
Demänová 393
031 06 Liptovský Mikuláš 6

SLOVENIE
Ministry of Defence
Central Registry for EU & NATO
Vojkova 55
1000 Ljubljana

TURQUIE
Milli Savunma Bakanlığı (MSB)
ARGE ve Teknoloji Dairesi
Başkanlığı
06650 Bakanliklar – Ankara

AGENCES DE VENTE

The British Library Document
Supply Centre
Boston Spa, Wetherby
West Yorkshire LS23 7BQ
ROYAUME-UNI

Canada Institute for Scientific and
Technical Information (CISTI)
National Research Council Acquisitions
Montreal Road, Building M-55
Ottawa, Ontario K1A 0S2
CANADA

NATIONAL DISTRIBUTION CENTRES

BELGIUM
Royal High Institute for Defence –
  KHID/IRSD/RHID
Management of Scientific & Technological
  Research for Defence, National STO
  Coordinator
Royal Military Academy – Campus
  Renaissance
Renaissancelaan 30
1000 Brussels

BULGARIA
Ministry of Defence
Defence Institute "Prof. Tsvetan Lazarov"
"Tsvetan Lazarov" bul no.2
1592 Sofia

CANADA
DSTKIM 2
Defence Research and Development Canada
60 Moodie Drive (7N-1-F20)
Ottawa, Ontario K1A 0K2

CZECH REPUBLIC
Vojenský technický ústav s.p.
CZ Distribution Information Centre
Mladoboleslavská 944
PO Box 18
197 06 Praha 9

DENMARK
Danish Acquisition and Logistics Organization
  (DALO)
Lautrupbjerg 1-5
2750 Ballerup

ESTONIA
Estonian National Defence College
Centre for Applied Research
Riia str 12
Tartu 51013

FRANCE
O.N.E.R.A. (ISP)
29, Avenue de la Division Leclerc – BP 72
92322 Châtillon Cedex

GERMANY
Streitkräfteamt / Abteilung III
Fachinformationszentrum der
  Bundeswehr (FIZBw)
Gorch-Fock-Straße 7
D-53229 Bonn

GREECE (Point of Contact)
Defence Industry & Research General
  Directorate, Research Directorate
Fakinos Base Camp, S.T.G. 1020
Holargos, Athens

HUNGARY
Hungarian Ministry of Defence
Development and Logistics Agency
P.O.B. 25
H-1885 Budapest

ITALY
Ten Col Renato NARO
Capo servizio Gestione della Conoscenza
F. Baracca Military Airport "Comparto A"
Via di Centocelle, 301
00175, Rome

LUXEMBOURG
See Belgium

NETHERLANDS
Royal Netherlands Military
  Academy Library
P.O. Box 90.002
4800 PA Breda

NORWAY
Norwegian Defence Research
  Establishment, Attn: Biblioteket
P.O. Box 25
NO-2007 Kjeller

POLAND
Centralna Biblioteka Wojskowa
ul. Ostrobramska 109
04-041 Warszawa

PORTUGAL
Estado Maior da Força Aérea
SDFA – Centro de Documentação
Alfragide
P-2720 Amadora

ROMANIA
Romanian National Distribution Centre
Armaments Department
9-11, Drumul Taberei Street
Sector 6
061353 Bucharest

SLOVAKIA
Akadémia ozbrojených síl gen
  M.R. Štefánika, Distribučné a
  informačné stredisko STO
Demänová 393
031 06 Liptovský Mikuláš 6

SLOVENIA
Ministry of Defence
Central Registry for EU & NATO
Vojkova 55
1000 Ljubljana

SPAIN
Área de Cooperación Internacional en I+D
SDGPLATIN (DGAM)
C/ Arturo Soria 289
28033 Madrid

TURKEY
Milli Savunma Bakanlığı (MSB)
ARGE ve Teknoloji Dairesi Başkanlığı
06650 Bakanliklar – Ankara

UNITED KINGDOM
Dstl Records Centre
Rm G02, ISAT F, Building 5
Dstl Porton Down, Salisbury SP4 0JQ

UNITED STATES
Defense Technical Information Center
8725 John J. Kingman Road
Fort Belvoir, VA 22060-6218

SALES AGENCIES

The British Library Document
Supply Centre
Boston Spa, Wetherby
West Yorkshire LS23 7BQ
UNITED KINGDOM

Canada Institute for Scientific and
Technical Information (CISTI)
National Research Council Acquisitions
Montreal Road, Building M-55
Ottawa, Ontario K1A 0S2
CANADA

ISBN 978-92-837-2188-8